**From the Institute of Neuro- and Bioinformatics**
**Of the University of Lübeck**
**Director: Prof. Dr. rer. nat. Thomas Martinetz**

# Computational Modelling of Memory-Associated Neural Slow Oscillations, Sleep Spindles, and Sharp Wave Ripples

Dissertation
For Fulfillment of
Requirements
For the Doctoral Degree
of the University of Lübeck

from the Department of Computer Science

Submitted by

Muhammad Mushtaq
from Pakistan

Lübeck 2023

First referee: Prof. Dr. rer. nat. Thomas Martinetz

Second referee: Prof. Dr.-Ing. habil. Marcin Grzegorzek

Chairman: Prof. Dr. Stefan Fischer

Date of oral examination: 13 February 2024

Approved for printing: 17 April 2024

# Acknowledgments

First and foremost, I would like to express my gratitude to my advisor, Prof. Thomas Martinetz for allowing me to complete my PhD at his institute. He always agreed with my choices and defended me when I was in need. I am aware that it wasn't always easy. His tremendous support during my research is unforgettable to me.

I am deeply indebted to Prof. Lisa Marshall. Furthermore, I vividly recall the conversations we had throughout my entire research period. She always guided and taught me what it takes to become a professional scientist.

I am unable to adequately express my gratitude towards my parents and family, even though they have been incredibly loving and supportive to me all this time. Most importantly, I cannot forget their support during COVID 19 when I almost lost social contacts. It was a really hard time for everyone who was away from his family. Here, I would like to dedicate a few words to my late mother, who eagerly awaited the completion of my doctoral thesis. Unfortunately, she left us before we could celebrate this event.

The same appreciation is extended to Mrs. Yvonne Marbach and Mr. Dirk Lagin for their unwavering administrative and technical support. When I came to Germany, I initially faced some difficulties, and the foremost among them was the language barrier. Whenever I face any problem, I find them to be quite helpful and encouraging. They never let me feel like I am away from my home country.

As this effort would not be feasible without the financial assistance provided by the US-German Collaboration in Computational Neuroscience (NSF/BMBF grant 01GQ1706), I am grateful to all those who made this opportunity possible.

It would be unjust if I forget my INBer colleagues and, most importantly, the faculty members: Prof. Erhardt Barth and Dr. Amir Madany. I found them quite helpful and supportive whenever I dealt with them. In scientific staff, I would like to thank my colleagues, Mr. Manuel Laufer and Mr. Dominik Mairhöfer who stood by me when I was down. These are the individuals who all contributed to my success and never made me feel out of place in this wonderful community. This wouldn't have been such a wonderful journey without all these people.

*When every inch of the world is known, sleep may be the only wilderness that we have left.*

Louise Erdrich

# Abstract

Sleep is a complex and multifunctional physiological process that rejuvenates the brain after several hours of work and also accomplishes various necessary tasks. It is divided into two stages: Rapid Eye Movement (REM) sleep and non-Rapid Eye Movement (NREM) sleep. The NREM stage is characterized by three prominent EEG rhythms: cortical slow oscillations (SOs), thalamic sleep spindles, and hippocampal sharp wave ripples (SPW-Rs). The experimental observations suggest that these EEG rhythms potentially play a role in memory consolidation. In this work, a series of computational models for simulating SPW-Rs, SOs, and sleep spindles were developed and investigated.

In first study we present a theoretical model of SPW-Rs. We demonstrate the impact of calcium influx and gap junctions on pyramidal cells for the modulation of SPW-Rs in a computational model of CA1. In this model, SPW-Rs are simulated with gradual reduction of calcium and with decreasing conductance through gap junctions in PCs. Both, with calcium reduction as well as with conductance reduction through gap junctions, SPW-Rs are suppressed. Both effects add up synergistically in combination.

In second study, we present a thalamocortical computational model for NREM sleep that exhibits both fast and slow spindles along with the SOs. In humans, sleep spindles are categorized into slow spindles (8–12 Hz) and fast spindles (12–16 Hz), with different properties. Our modeling results show that fast spindles lead to faster cortical cell firing, and subsequently increase the amplitude of the cortical local field potential (LFP) during the SO down-to-up phase. Neither the SO rhythm nor the duration of the SO down state is affected by slow spindle activity. Together, our model results suggest that slow spindles may facilitate the initiation of the following SO cycle, without however affecting expression of the SO Up and Down-states.

In last study, we present another thalamocortical model with closed loop stimulation (CLS) protocols to investigate the impact of CLS on spindle activity. Our model results show that the power of spindles is significantly increased when stimulation cues are applied at the commencing of an SO Down to Up-state transition, but that activity gradually decreases when cues are applied with an increased time delay from this SO phase. Conversely, stimulation is not effective significantly when cues are

applied during the transition of an SO Up to Down-state. Furthermore, our model suggests that a strong inhibitory input of reticular (RE) layer to a thalamocortical (TC) layer in the thalamic network shifts leads to an emergence of spindle activity at the SO Up to Down-state transition and the spindle frequency is also reduced (8-11 Hz) by thalamic inhibition.

In summary, neuronal network oscillations of various frequencies play a crucial role in different mnemonic functions, such as the acquisition of learning, formation of memory traces, and memory consolidation. These oscillations strengthen synaptic plasticity and enhance neural synchrony. This neural synchronization is believed to be important for facilitating communication and transferring information among different regions of the brain. Computational models of these network oscillations have opened up multifaceted opportunities to gain an understanding of complex neural phenomena and to elucidate underlying mechanisms that are often unattainable through experimental studies alone. In this study, computational models of SOs, sleep spindles, and SPW-Rs have been constructed. The effects of various stimulations on different parameters of these oscillatory patterns have been investigated. This theoretical work on neuronal network oscillations shall contribute to bridging the gap between various physiological functions, experimental observations, and the intricate mechanisms that underlie them.

# Zusammenfassung

Schlaf ist ein komplexer und multifunktionaler physiologischer Prozess, der das Gehirn nach mehreren Stunden Denkarbeit erfrischt und noch weitere wichtige Aufgaben erfüllt. Man unterteilt Schlaf in zwei Phasen: REM-Schlaf (Rapid Eye Movement) und NREM-Schlaf (Non-Rapid Eye Movement). Die NREM-Phase ist durch drei auffällige EEG-Rhythmen gekennzeichnet: kortikale langsame Oszillationen (Slow oscillations; SOs), thalamische Schlafspindeln und sogenannte "hippocampal sharp-wave rippel" (sharp wave ripples; SPW-Rs). Die experimentellen Beobachtungen legen nahe, dass diese EEG-Rhythmen möglicherweise eine Rolle bei der Gedächtniskonsolidierung spielen. Im Rahmen dieser Arbeit wurden eine Reihe von Computermodellen zur Simulation von SPW-Rs, SOs und Schlafspindeln entwickelt und untersucht.

In der ersten Studie stellen wir ein theoretisches Modell der SPW-Rs vor. Wir demonstrieren die Auswirkungen des Kalziumeinstroms und der Gap-Junctions auf Pyramidenzellen für die Modulation von SPW-Rs in einem Computermodell von CA1. In diesem Modell werden SPW-Rs mit einer allmählichen Kalziumreduktion und mit einer abnehmenden Leitfähigkeit durch Gap Junctions in PCs simuliert. Sowohl bei der Kalziumreduktion als auch bei der Leitfähigkeitsreduktion durch Gap Junctions werden SPW-Rs unterdrückt. Beide Effekte kombiniert addieren sich synergistisch.

In der zweiten Studie stellen wir ein thalamokortikales Berechnungsmodell für den NREM-Schlaf vor, das neben den SOs auch schnelle und langsame Spindeln aufweist. Beim Menschen werden Schlafspindeln in langsame Spindeln (8-12 Hz) und schnelle Spindeln (12-16 Hz) mit unterschiedlichen Eigenschaften eingeteilt. Unsere Modellierungsergebnisse zeigen, dass schnelle Spindeln zu einer schnelleren kortikalen Zellfeuerung führen und in der Folge die Amplitude des kortikalen lokalen Feldpotenzials (LFP) während der SO-Abwärts-nach-Aufwärts-Phase erhöhen. Weder der SO-Rhythmus noch die Dauer des SO-Down-Zustands werden durch langsame Spindelaktivität beeinflusst. Zusammengenommen deuten unsere Modellergebnisse darauf hin, dass langsame Spindeln die Einleitung des folgenden SO-Zyklus erleichtern können, ohne jedoch die Ausprägung der SO-Auf- und Ab-Zustände zu beeinflussen.

In der letzten Studie haben wir ein weiteres thalamokortikales Modell mit Closed-Loop-Stimulationsprotokollen (CLS) vorgestellt, um die Auswirkungen von CLS auf die Spindelaktivität zu untersuchen. Die Ergebnisse unseres Modells zeigen, dass die Leistung der Spindeln signifikant erhöht wird, wenn die Stimulationsreize zu Beginn eines SO-Abwärts-zu-Aufwärts-Übergangs appliziert werden, dass aber die Aktivität allmählich abnimmt, wenn die Stimulationsreize mit einer größeren zeitlichen Verzögerung zu dieser SO-Phase appliziert werden. Umgekehrt ist die Stimulation nicht signifikant wirksam, wenn die Stimulationsreize während des Übergangs von einem SO Up zu einem Down-State angewendet werden. Darüber hinaus deutet unser Modell darauf hin, dass ein starker inhibitorischer Input von der retikulären (RE) Schicht zu einer thalamokortikalen (TC) Schicht im thalamischen Netzwerk zu einem Auftreten von Spindelaktivität beim Übergang von SO Up zu Down-State führt und die Spindelfrequenz durch thalamische Inhibition ebenfalls reduziert wird (8-11 Hz).

Zusammenfassend lässt sich sagen, dass Oszillationen verschiedener Frequenzen in neuronalen Netzwerken eine entscheidende Rolle bei verschiedenen mnemotechnischen Funktionen spielen, z. B. beim Lernen, bei der Bildung von Gedächtnisspuren und bei der Gedächtniskonsolidierung. Diese Oszillationen verstärken die synaptische Plastizität und verbessern die neuronale Synchronität. Man geht davon aus, dass diese neuronale Synchronisation wichtig ist, um die Kommunikation und die Übertragung von Informationen zwischen verschiedenen Hirnregionen zu erleichtern. Computergestützte Modelle dieser Netzwerk-oszillationen haben vielfältige Möglichkeiten eröffnet, komplexe neuronale Phänomene zu verstehen und die zugrunde liegenden Mechanismen aufzuklären, die durch experimentelle Studien allein oft nicht erreicht werden können. In dieser Studie wurden Berechnungsmodelle für SOs, Schlafspindeln und SPW-Rs erstellt. Die Auswirkungen verschiedener Stimulationen auf unterschiedliche Parameter dieser oszillatorischen Muster wurden untersucht. Diese theoretische Arbeit über neuronale Netzwerk-Oszillationen soll dazu beitragen, die Wissenslücke zwischen verschiedenen physiologischen Funktionen, experimentellen Beobachtungen und den komplizierten Mechanismen, die ihnen zugrunde liegen, zu schließen.

# Contents

# List of Figures

# List of Tables

# Abbreviations

| | |
|---|---|
| AMPA | α-amino-3-hydroxy-5-methyl-4-isoxazolepropionic acid |
| CLS | Closed loop stimulation |
| DSt | Driving stimulation |
| EEG | Electroencephalogram |
| EPSP | Excitatory postsynaptic potential |
| $GABA_A$ | γ-Aminobutyric acid type A |
| $GABA_B$ | γ-Aminobutyric acid type B |
| IN | Interneuron |
| IPSP | Inhibitory postsynaptic potential |
| LFP | Local field potential |
| NMDA | N-methyl-d-aspartate |
| NREM | Non-rapid eye movement |
| PSP | Postsynaptic potential |
| PY | Pyramidal |
| RE | Reticular |
| REM | rapid eye-movement |
| SO | Slow oscillation |
| SPW-Rs | Sharp wave ripples |
| SWA | Slow-wave activity |
| SWS | Slow-wave sleep |
| TC | Thalamocortical |

Chapter 1

# Introduction

Sleep is an important reversible state that demonstrates distinctive features of loss of consciousness, behavioral control, and reduced response to external stimuli. It has a critical role in multiple physiological functions (1) and among these functions, the establishment of memories seems quite important. Sleep assists in consolidation of newly encoded memory during an awake state (2), (3), (4). Consolidation form and merge these memories with preexisting long-term memories.

In mammals, sleep is classified into two primary stages: rapid eye movement (REM) sleep and NREM sleep. Both stages alternate in a cyclic form during nocturnal sleep. NREM sleep is further classified into three stages: N1, N2, and N3. These stages are characterized by low frequency and high amplitude oscillations in the electroencephalogram (EEG). On the other hand, REM sleep is characterized by wake-like fast and low-amplitude oscillatory brain activity. N2 is characterized by the occurrence of sleep spindles (waxing and waning like a spindle shape) and K complex rhythm. N3 also corresponds to slow wave sleep (SWS), which is dominated by low-frequency, high-amplitude oscillation referred to as slow wave activity (SWA) and hippocampal sharp wave ripples (SPW-Rs). In rodents, the N2 and N3 stages are merged into single N3 stage. In human nocturnal sleep, SWS is the most prominent in the early part of sleep and decreases in duration and intensity as sleep progresses. On the other hand, REM sleep becomes more dominant in the later part of sleep (Figure. 1.1).

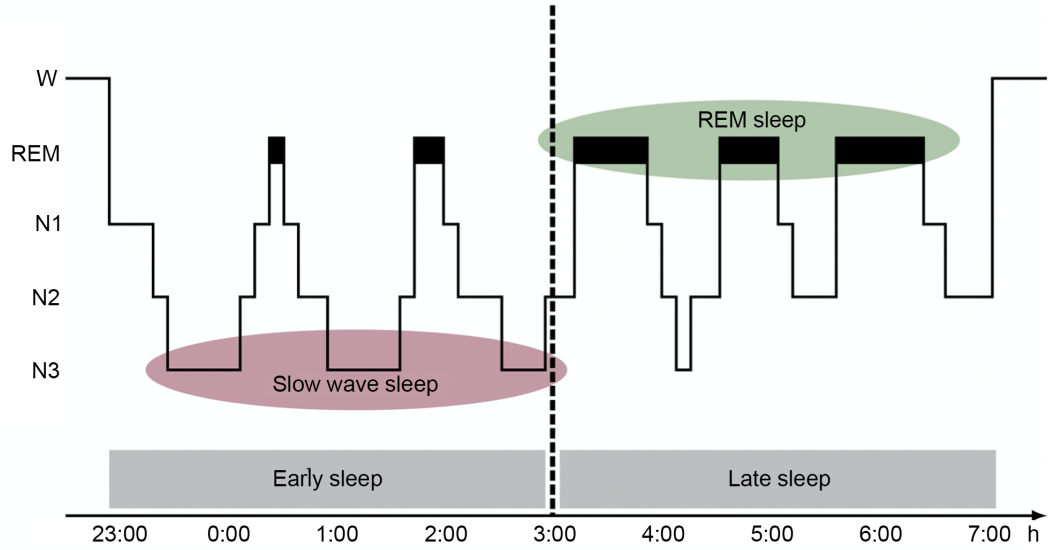


**Figure 1. 1 A single night of human sleep.**

Human sleep alternates between multiple cycles of REM and NREM. The NREM sleep is subdivided into light sleep stages: N1 and N2, and deep sleep/slow wave sleep (SWS), which corresponds to N3. SWS/N3 sleep dominates during the first half of the sleep, while REM sleep dominates during the second half. The figure was adopted from (2).

## 1.1 Sleep and memory

One of the most influential roles of sleep is to facilitate the consolidation of newly encoded memories through specific neuromodulations. (5), (3), (2), (6). Before moving forward, we will briefly discuss memory. Memory can be defined as the information acquired from the surrounding environment and stored for survival in a dynamic environment. Normally, memory is divided into two categories based on storage time period: short-term memory and long-term memory. The short-term memory holds a limited amount of information for a limited time period (for a few seconds) (7). Conversely, long-term memory permanently stores an unlimited amount of information. Moreover, long-term memory comprises various types of contents that are processed and stored in different brain structures, ultimately dividing it into two categories: declarative memory and non-declarative memory (8). Declarative memory deals with the memory of explicit events and facts, whereas non-declarative memory is associated with habits, skills, and emotions (9), (10), (11), (1). Coming back to the relationship between sleep and memory, it has been hypothesized that REM sleep is strongly associated with the processing of non-

declarative memory, while NREM sleep is linked to the processing of declarative memory (12), (13), (3), (2).

## 1.2 Characteristics of NREM sleep

The cortex, thalamus, and hippocampus play highly interactive roles during NREM sleep (14). In SWS, the cortical network generates slow wave activity (SWA) that is dominated by low frequency (1<Hz); slow oscillation (SO) (15), (16). The thalamic network generates burst-like waxing and waning-shaped sequences of 10-16 Hz oscillations that correspond to sleep spindles. In humans, sleep spindles are frequently found in N2 sleep but are also observed in SWS (17), (18). Finally, the hippocampal sharp-wave ripples (SPW-Rs) are another prominent EEG rhythm during NREM sleep. Sharp waves are fast-depolarizing waves that are generated in the CA3 region and are accompanied by fast oscillations (110-200 Hz) called ripples (19).

### 1.2.1 Cortical Structures and slow oscillations (SO)

The neocortex is a highly organized, six-layered, and densely interconnected structure (20), (21), (22). Each layer, from the superficial layer 1 to the deepest layer 6, each consists of different types of neurons and their efferent and afferent pathways (23). These layers contain two types of excitatory neurons: spiny stellate cells and pyramidal cells. The spiny stellate cells are located in the internal granular layer IV. These cells receive thalamocortical input and generate excitatory feedback in association with pyramidal cells (24), (25), (26), (27). The pyramidal cells, which are extensively located in layers III and V (26), (28). These cells have unique properties, consisting of long axons that allow them to connect with other regions of the brain, such as the thalamus and hippocampus (29), (30). Besides excitatory cells, each cortical layer also contains inhibitory cells, also called GABAergic interneurons, which form close local connections (22).

Slow oscillations (SOs) are cortical EEG rhythms with a large amplitude and a low frequency (~1 Hz), have been extensively studied during the last two decades. According to experimental and modeling studies, SOs are the result of synchronized depolarization and hyperpolarization activity in a wide range of cortical cells (31), (15), (32), (33). During the large amplitude of SOs, also known as up states, the

majority of cortical neurons fire or become depolarized and maintain in this depolarized state for several hundred milliseconds. Conversely, during the down state, virtually all cortical neurons remain silent or exhibit a hyperpolarized state for a few hundred milliseconds (15), (34), (35), (36).

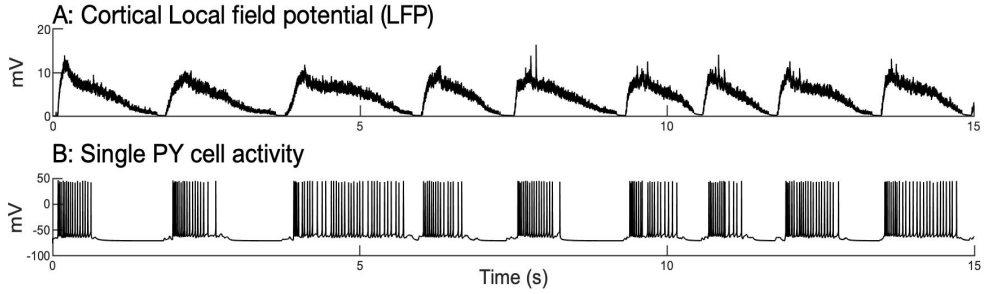


**Figure 1. 2 Cortical LFP and single cell activity.**

Cortical local field potential (LFP) and activity of single pyramidal (PY) cells in slow oscillations (SOs). ***A***, Cortical LFP exhibits slow oscillations with up/depolarized and down/hyperpolarized states. ***B***, A single PY cell synchronously fires during the up state of SO and becomes silent during the down state of SO.

In some experimental observations, mini postsynaptic currents were found in cortical cells during the down state of SO (32). It has been suggested that the summation of these mini currents may depolarize the membrane potential of any single PY cell sufficiently to trigger a persistent sodium current Na(p). This further depolarizes the PY cell, leading to the generation of an action potential. The action potential of one or a few cortical neurons may trigger activity in the entire cortical network and initiate the SO (32). Conversely, the calcium-dependent potassium current and progressive synaptic depression terminate the depolarized/up state and bring the cortical network back to the down state (37).

### 1.2.2 Thalamic structures and sleep spindles

The thalamus serves as the primary gateway to the cortex. Nearly all sensory inputs from the outside the world must pass through the thalamus. The thalamus forms a relatively small structure on each side of the midline and can be divided into multiple nuclei. Each nucleus is responsible for transmitting specific types of afferent sensory signals (38). Among these nuclei, the thalamic reticular nucleus (TRN) enfolds rest of the nuclei and provides them with inhibitory feedback through GABAergic reticular (RE) cells (39). TRN receives excitatory input from both the VI layer of the neocortex and dorsal thalamic nuclei, but it only sends feedback to thalamic nuclei

(40), (38). As we discussed earlier, the thalamic relay cells target the spiny stellate cells in layer IV. Layer IV sends input to the PY cells in layer V, which in turn project back to thalamus, completing the thalamocortical loop.

The thalamic network initiates sleep spindles (17), (41), (42), which are one of the hallmark EEG rhythms of NREM sleep. They are extensively found in the N2 stage (18). Sleep spindles are bursts of waxing and waning-shaped sequences of 10-16 Hz oscillations that last between 0.5 to 3 seconds and reappear after 5-15 seconds (**Fig 1.3A**) (18). In the thalamic network, the interactions between thalamocortical (TC) and reticular (RE) cells produces sleep spindle oscillations. These oscillations are primarily influenced by the TC hyperpolarization current ($I_h$) and the transient calcium current ($I_T$), also known as low threshold calcium (43), (44), (45). Moreover, TRN alone can also generate a sustained spindle rhythm with the assistance of $I_T$ current (46), (47).

In humans, sleep spindles are classified into two categories: fast spindles (12-16 Hz) and slow spindles (8-12 Hz), each with differential characteristics. The fast spindles are mostly found in the central and parietal cortical regions, and they are nested with SOs during the first-half of the up state. Slow spindles are observed in the frontal cortical area, and these are nested with SO during the second-half of the up state, (**Fig 1.3B**) (18), (48). Fast spindles have been extensively studied in terms of their origin, generation mechanism, functional role, temporal, and spatial appearance in various cortical regions (49), (50), (51), (18). Slow spindles, mainly found in the human deep sleep EEG, have been less extensively studied and their source, generation, and functional roles remain unclear.

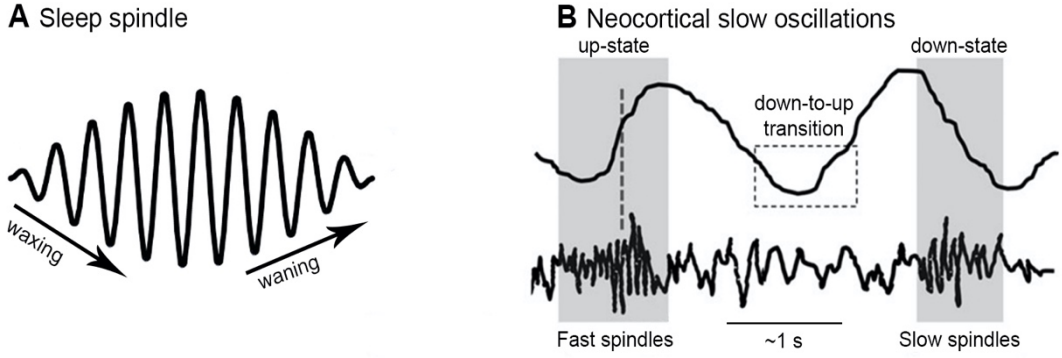

**Figure 1. 3 Sleep spindles.**

Morphology of sleep spindles and their coordination with the slow oscillations. ***A,*** Sleep spindles are distinct events with waxing and waning morphology. ***B,*** During sleep, fast spindles often emerge during the first-half of the up state of SO. The slow spindles often emerge during the second-half of up state of the SO. The figure was modified from (52).

### 1.2.3 Hippocampal structures and sharp-wave ripples SPW-Rs

The hippocampal formation is one of the most extensively researched brain structures in the field of neuroscience. In the human brain, it is located deep within the medial temporal lobe (53), (54), (55). The hippocampal formation is fundamentally classified into four cortical regions: the dentate gyrus, the hippocampus proper, the subiculum, and the entorhinal cortex (53), (54). The hippocampus is further divided into three subfields: CA3, CA2, and CA1. The sub-regions of the hippocampal formation mostly make connections in a unidirectional way. The prefrontal pathways of the entorhinal cortex project to the dentate gyrus, providing it with significant input. Similarly, the dentate gyrus targets to CA3 via the mossy fibers of granule cells, and CA3 targets the CA1 via the Schaffer collaterals of CA3 pyramidal cells (53). Along with the slow oscillations and sleep spindles, sharp-wave ripples (SPW-Rs) are another prominent EEG rhythm of NREM sleep that are initiated in the hippocampus.

In the rat hippocampus, SPW-Rs are the most consistent oscillatory rhythms, exhibiting high local field potential amplitude (~1 mV) and high spatial coherence over 1 mm (56), (57), (58), (19). In the stratum radiatum of CA1, SPW-Rs are generated due to synchronous excitatory input from the CA3 pyramidal cells through Schaffer collaterals (59). These Schaffer collaterals initiate high-frequency oscillations (ripples; 140–250 Hz) in the CA1 region (Fig 1.4). The cellular mechanism of SPW-Rs in vivo and in vitro is highly debated. In SPW-Rs, the high-frequency component (ripples) appears to arise through the collaboration of both chemical synaptic and non-chemical (electrical synapses/gap junctions) mechanism, particularly at the in vitro level (60), (61), (62).


**Figure 1. 4 Frequency Components of sharp wave ripple In Vitro.**

***A,*** Raw data recorded from the hippocampal PY cells of mice. ***B,*** The raw data after the band-pass filter (150-300Hz) shows ripples. ***C,*** The raw data after the low-pass filter (1-50Hz) shows the presence of a sharp wave. The figure was modified from (60).

## 1.3 NREM sleep rhythms and active system consolidation

As discussed in the previous sections, NREM sleep plays a crucial role in the consolidation of declarative memories. In the standard two-stage memory model, declarative memories are initially encoded into a temporary store, known as the hippocampus, before being transferred and stored in the neocortex as long-term memories during sleep (63), (64), (65). Based on this two-stage model, sleep is proposed to serve as an active system consolidation. Moreover, active system consolidation is a process in which newly encoded memories are redistributed and stored in other neuronal circuits as long-term memories (14). According to the active system consolidation model, newly acquired information, particularly episodic memory, is initially encoded simultaneously in both the neocortical networks and the hippocampus along with the adjacent medial temporal lobe. In subsequent sleep, particularly during SWS, these newly acquired memory traces are repeatedly reactivated and eventually, redistributed, strengthening the neocortical synaptic connections and forming persistent memories.

Several experimental studies reveal that the higher rate of information encoding during the active state increases the density and amplitude of SOs in subsequent SWS (66), (16), (67). Moreover, at the local field potentials (LFPs) level, along with SOs, the activities of sleep spindles and hippocampal ripples also increase during sleep after learning experiences (68), (69), (2), (18). Likewise, these increased activities also improve the retention rate of the learned experiences (70), (71), (72), (2).

During SWS, synchronized cortical neuronal activity also activates the thalamic and hippocampal networks through efferent pathways, initiating thalamocortical spindles and hippocampal SPW-Rs (Fig. 1.5). Eventually, the depolarized/up state of SO

provides a broad temporal framework in which hippocampal circuits of memories are repeatedly reactivated in the form of SPW-Rs, in parallel with the thalamocortical spindles. In a meanwhile, both thalamic and hippocampal structures send feedback to the neocortex, which arrives at the same time and is still in the up/depolarized state of SO. The hippocampal ripples and accompanying memory traces become nested within the single troughs of spindle (73), (74). Moreover, the spindles reach the neocortex, likely to assist in $Ca^{2+}$ influx for subsequent processes of synaptic plasticity (2), (75), (76). In summary, the transfer of reactivated memory traces from the hippocampus to the neocortex, which occurs during the up/depolarized state, is parallel to the arrival of spindles. This transfer is a prerequisite for the better formation of persistent memory traces in the neocortical network (14).

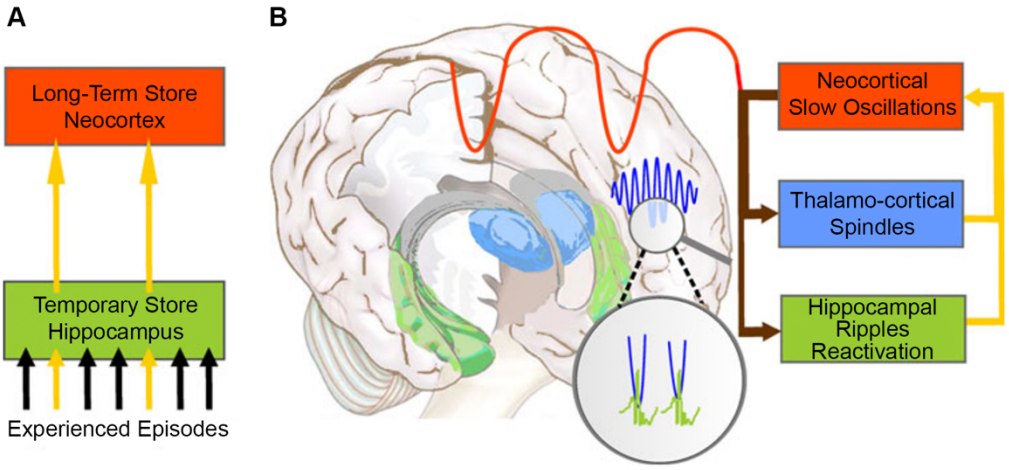


**Figure 1. 5 Active system consolidation during SWS.**

***A,*** Newly acquired memories are initially encoded in a temporary store, namely the hippocampus, and later reactivated to be distributed in the neocortex as long-term storage during SWS. ***B,*** Interaction between neocortical, thalamic, and hippocampal structures during SWS. The depolarized/up state of SOs (red) repeatedly reactivates the hippocampal memory traces along with SPW-Rs (green). These SPW-Rs become nested within single troughs of the thalamic spindle (blue) in the fine temporal window. The figure was taken from (2).

## 1.4 Chemical synapses and electrical synapses

Generally, neurons in different brain structures communicate with one another by releasing chemical messengers called neurotransmitters, which can have either an excitatory or inhibitory effect. The key excitatory neurotransmitter in the brain is the amino acid glutamate, while the main inhibitory neurotransmitter is gamma-aminobutyric acid, also known as GABA. All types of neurotransmitters induce their postsynaptic electrical response by binding to and activating various groups of

proteins called neurotransmitter receptors (77). The main excitatory (ionotropic) receptors discussed are α-amino-3-hydroxy-5-methyl-4-isoxazolepropionic acid receptors (AMPAR) and N-methyl-D-aspartate receptors (NMDAR). AMPARs show a faster response, whereas the NMDARs show a slower response after the release of neurotransmitters in synaptic the cleft (78). In addition, both AMPAR and NMDAR play important roles in the synaptic plasticity (79), (80), (81), (82). Similarly, the γ-Aminobutyric acid type A receptors ($GABA_AR$) are fast inhibitory (ionotropic), while γ-Aminobutyric acid type B receptors ($GABA_BR$, metabotropic) are slow inhibitory receptors (83), (84).

Besides chemical synapses, electrical synapses are found in the nervous systems of rodents, humans, and other species. In electrical synapses, the membranes of both communicating neurons come extremely close to each other and are linked together by an intracellular mechanism called a gap junction (85), (86). The gap junctions consist of aligned channels in both the membranes of adjacent neurons, and these aligned pairs of channels form a pore. These pores of gap junctions are quite large compared to the pores of chemical synapses (48) and as a result, ions and molecules diffuse directly through the pores of gap junctions. The response of electrical synapses is significantly faster compared to chemical synapses, and they are believed to have an important role in the brain development and pattern formation (87). Gap junctions are thought to play a crucial role in sharp wave ripples (SPW-Rs), especially in neuronal synchronization during high-frequency ripples (~200 Hz) activity based on an *in vitro* study (88). Moreover, various theoretical modeling studies suggest that gap junctions are located between the axonal compartments of hippocampal pyramidal cells (89), (90), (91).

## 1.5 Role of calcium and gap junctions in modulation of SPW-Rs

Several investigations reveal that variations in cholinergic input to the hippocampus have been involved in the sudden transitions of SPW-Rs to gamma oscillations and vice versa (92), (93), (94). In addition to acetylcholine (ACh), other neuromodulators, such as norepinephrine (NE), serotonin (5-HT) also suppress ripple activity in rodents (95), (96), (97). These neuromodulators act through various receptors, which engage different signaling cascades and have multiple effects on hippocampal neurons. NE and 5-HT cause mild to moderate hyperpolarizations of CA3 pyramidal

neurons, while ACh depolarizes them. Briefly, they modulate synaptic strength and efficacy, alter excitation and inhibition, interfere with transmitter release, and reduce calcium influx (98), (99), (100), (101). In spite of having multimodal effects, these neuromodulators suppress SPW-Rs possibly by reducing the calcium influx to axon collaterals, (93), (95), (97) and altering conductance through gap junctions (60).

## 1.6 SWS and external stimulations

We have already discussed the role of SWS in the consolidation of declarative memory. The higher rate of information encoding during active state increases the density and amplitude of SOs in subsequent SWS (66), (16), (67). In addition to SOs, the sleep spindles are also directly linked to memory formation during sleep (102), (103). Different experimental studies have revealed that the activity of slow oscillations (SO) and sleep spindles can be increased through sensory and electrical stimulation during NREM sleep. Likewise, this increased SW activity also improves sleep performance in terms of memory consolidation (104). In these studies, applied sensory stimuli were associated with the learning material during the training (also called the target memory reactivation; TMR) before sleep (105), (106), (107), (108). In the result of learning associated sensory stimuli, the memory performance was relatively better compared to the non-simulation case (109).

In some other studies, stimuli unassociated with learning content were also applied in the form of pink noise during NREM sleep (110), (111). The unassociated stimuli were effective only when the auditory ‘clicks’ were synchronously delivered with slow waves and subsequently, the amplitude of the slow waves and retention performance were improved. On the other hand, outside of the phase, stimuli were not effective in relation to memory performance (110), (112). In electrical stimulation, transcranial direct current stimulation (tDCS) utilizes electrodes that are bilaterally positioned at central and/or frontal cortical locations to deliver a slow oscillating current (.75 Hz). This current is applied with a reference electrode that completes the circuit (113), (114). In the result of tDCS, the retention rate of the learned experiences before sleep was improved compared to the non-stimulation paradigm (113).

## 1.7 Outline and main research questions

In the second chapter, various modeling approaches commonly used for neuronal modeling are discussed. The next three chapters (3 to 5) deal with modeling studies. In these three chapters, the introduction and the methods used in the study are included at the beginning of each chapter. The last chapter deals with discussion and summary of all three studies.

**Chapter 2: Methods.** In this chapter, various neuronal modeling methods are discussed. Along with other methods, the conductance-based modeling approach is discussed in detail which is used in current modeling studies. Additionally, the NEURON simulator is discussed which was used to develop these models.

**Chapter 3: Suppression of SPW-Rs by controlling calcium and gap junctions.** In this chapter, a computational model for SPW-Rs is presented. This study demonstrates the impact of calcium influx and gap junctions on pyramidal cells in the modulation and suppression of SPW-Rs in a computational model of CA1.

**Chapter 4: Differential thalamocortical interactions in slow and fast spindle generation.** In this chapter, a thalamocortical computational model for NREM sleep is presented, which demonstrates the presence of both fast and slow spindles, as well as the occurrence of SOs. The purpose of this study is to investigate the potential mechanism of slow sleep spindles initiation and their role.

**Chapter 5: Closed loop stimulations and sleep spindles.** In this study, we present another thalamocortical model for NREM sleep that exhibits fast spindles along with the SO rhythm. In addition, closed loop stimulation (CLS) protocols are also implemented to study the effect of stimulation cues on the activity of sleep spindles. The purpose of this study is to find the optimal SO phase for stimulation cue in order to achieve increased spindle activity.

**Chapter 6: Discussion and summary.** In the last chapter, the thesis concludes with a discussion and summary of these three studies.

Chapter 2

# Methods

In neuroscience, mathematical models, along with experimental approaches, play a very important role in understanding the process of information processing in the nervous system. These modeling studies provide possible explanations of information processing and sometimes provide predictions about the results of new experiments. If the new experimental observations agree with the model predictions, the model is considered reliable and accepted for the time being. Conversely, if the experimental results disagree with the model predictions, the model theory is rejected. Eventually, computational models are used to assist in reasoning, removing ambiguity from theories, and can be helpful for testing hypotheses in some cases. In this chapter, various computational modeling approaches are discussed that are widely utilized in the field of neuroscience. Our main focus is the conductance-based modeling approach that was employed in this work.

## 2.1 Conductance based models

Two English physiologists, Alan Hodgkin and Andrew Huxley, laid the foundation for conductance-based models, also known as Hodgkin-Huxley (HH) based models. They quantitatively characterized the voltage dependence of membrane currents in the giant squid axon and demonstrated how the action potential can be generated and propagated (115), (116), (117), (118), (119). They conducted an experiment on the giant axon of a squid and revealed that the action potential emerges as a result of the interplay between two voltage-dependent currents: sodium ($Na^+$) and potassium ($K^+$) with the cable properties of the axon. They simulated the shape of an action potential using a quantitative model that consisted of a set of differential equations.

The HH model consists of two types of currents: the capacitive current $I_c$ and the ionic currents $I_i$ shown in the equivalent circuit diagram in Fig 2.1.

$$I = I_c + I_i \qquad 2.1.1$$

where $I$ represents the membrane current, which is sum of both $I_i$ and $I_c$.

$$I_c = C_M \frac{dV}{dt} \qquad 2.1.2$$

Here, $C_M$ represents the membrane capacitance. Similarly, in the basic model, the total ionic current is the sum of three ionic currents: sodium ($I_{Na}$), potassium ($I_K$), and leak ($I_L$) currents.

$$I_i = I_{Na} + I_K + I_L \qquad 2.1.3$$

Each ionic current is calculated by multiplying the driving force of the ion with the membrane conductance of that ion (120).

$$I_{Na} = g_{Na}(V - E_{Na})$$

$$I_K = g_K(V - E_K)$$

$$I_L = g_L(V - E_L)$$

Where $V$ is the membrane potential, $g_{Na}$, $g_K$, and $g_L$ are the conductances of *sodium*, *potassium*, and *leak* currents, respectively and $E_{Na}$, $E_K$, and $E_L$ are their corresponding equilibrium potentials. Finally, by adding the derived values of $I_i$ and $I_c$ in equation 2.1, we obtain the general differential equation of HH model.

$$I = C_M \frac{dV}{dt} + g_{Na}(V - E_{Na}) + g_K(V - E_K) + g_L(V - E_L) \qquad 2.1a$$

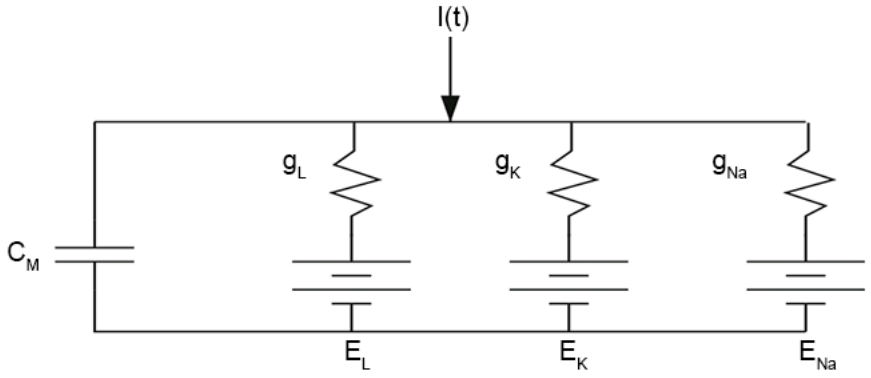


**Figure 2. 1 HH-type circuit diagram.**

The basic circuit diagram of Hodgkin-Huxley-type models. $C_M$ represents membrane capacitance, while $g_{Na}$, $g_K$, and $g_L$ represent the conductances of the ionic currents Na, K, and L, respectively. $E_{Na}$, $E_K$, an d $E_L$ denote their corresponding reversal potentials.

### 2.1.1 Voltage-Gated Channels

In the HH model, each channel is considered a transmembrane protein that forms a pore. This pore allows specific ions to diffuse through the membrane. The pores contain gates that can be opened or closed depending on the membrane voltage.

$$C \xrightarrow{\alpha(V)} O, O \xrightarrow{\beta(V)} C \qquad 2.1.4$$

Where *C* corresponds to the closed state of the gate and *O* corresponds to the open state of the gate. α(V) and β(V) are voltage-dependent rate constants that determine the opening and closing of the gate, respectively, from the closed and open states. If *m* is considered a fraction of open gates, then 1-*m* represents the fraction of closed gates. According to the law of mass action,

$$\frac{dm}{dt} = \propto (V)(1-m) - \beta(V)m = \frac{m_\infty(V)-m}{\tau(V)} \qquad 2.1.5$$

where $m_\infty(V)$ is steady state, $\tau(V)$ time constant,

$$m_\infty = \frac{\propto(V)}{\propto(V)+\beta(V)} \; and \; \tau(V) = \frac{1}{\propto(V)+\beta(V)} \qquad 2.1.6$$

This equation can be simplified if *V* is constant. The solution starts from *m*(0) is $m(t) = m_\infty(V) + (m(0) - m_\infty(V))e^{-t/\tau(V)}$.

Hodgkin and Huxley solved the equations for sodium and potassium conductances by using the voltage-clamp data. They proposed:

$$g_{Na} = \bar{g}_{Na} m^3 h, and \; g_K = \bar{g}_K n^4 \qquad 2.1.7$$

Where $\bar{g}_{Na}$ and $\bar{g}_K$ are the maximum conductances of sodium and potassium, respectively, and *m*, *h*, and *n* are gating variables that range from 0 to 1. The $n^4$ represents the probability that the potassium channel is open. Similarly, $m^3$ represents the probability that the sodium activation gate is open, and *h* represents the probability that the sodium inactivation gate is open.

The final set of equations of the HH model that calculate the total membrane current (as mentioned in equation 2.1) and the gating variables *n*, *m*, and *h* are:

$$I = C_M \frac{dV}{dt} + \bar{g}_{Na} m^3 h(V - E_{Na}) + \bar{g}_K n^4 (V - E_K) + g_L (V - E_L)$$

$$\frac{dm}{dt} = \propto_m (V)(1-m) - \beta_m(V)m$$

$$\frac{dh}{dt} = \propto_h (V)(1-h) - \beta_h(V)h$$

$$\frac{dn}{dt} = \propto_n (V)(1-n) - \beta_n(V)n$$

where

$$\propto_m (V) = 0.1 \frac{25 - V}{\exp\left(\frac{25 - V}{10}\right) - 1},$$

$$\beta_m(V) = 4 \exp\left(\frac{-V}{18}\right),$$

$$\propto_h (V) = 0.07 \exp\left(\frac{-V}{20}\right),$$

$$\beta_h(V) = \frac{1}{\exp\left(\frac{30 - V}{10}\right) + 1},$$

$$\propto_n (V) = 0.01 \frac{10 - V}{\exp\left(\frac{10 - V}{10}\right) - 1},$$

$$\beta_n(V) = 0.125 \exp\left(\frac{-V}{80}\right).$$

The parametric values are: $E_K$ = -12 mV, $E_{Na}$ = 120 mV, $E_L$ = 10.6 mV, $\bar{g}_K = 36$ mS/cm$^2$, $\bar{g}_{Na} = 120$ mS/cm$^2$, and $\bar{g}_L = .3$ mS/cm$^2$, C = 1 μF/cm$^2$.

The basic Hodgkin and Huxley model simulated only three ionic currents to reproduce the action potential. Current models include various types of currents and neurons, such as calcium currents (121), persistent sodium current, low threshold calcium currents, calcium-dependent potassium currents, hyperpolarization current (45), (43), (122), (123), (124) and others. Similarly, some recent models present a morphologically complex structure with multiple interconnected compartments (125), (91), (89).

## 2.2 Simple models

The conductance-based models provide significant details and some level of accuracy for each individual network cell. However, they require extensive computational resources and time. These models can be useful for small neuronal networks that deal with synaptic plasticity and/or specific intrinsic neuronal currents (126), (127), (128). Some neuronal models do not require detailed intrinsic information about individual neurons. Instead, they focus on specific aspects such as action potentials or the collective output of a network, such as local field potentials (LFP) and electroencephalograms (EEG). For this type of neuronal models, the lower-dimensional models or simple models can be more efficient, fast, and computationally less expensive than the conductance-based models. The three-

dimensional model of Hindmarsh-Rose (129), as well as the two-dimensional models of FitzHugh-Nagumo (130) and Morris-Leclar (131), are widely used and they also preserve the basic dynamical properties. The integrate and fire model is one of the most common and simplified reduced models, along with these other models. The integrate-and-fire modeling approach has a long history of over a hundred years and it has been widely used in neuronal modeling (132), (133), (134), (135). Integrate-and-fire models are relatively simple and fast as compared to the conductance-based models. These models describe the neuronal membrane potential in terms of injected currents and excitatory or inhibitory synaptic inputs received from other neurons through their associated synapses. When the membrane potential reaches the threshold, an action potential or spike is produced, regardless of the actual intrinsic neuronal mechanism that generates it (136).

$$C_M \frac{dv(t)}{dt} = I_{leak}(t) + I_S(t) + I_{inj}(t), \qquad 2.2.1$$

where $C_M$ represents the membrane capacitance, $I_{leak}(t)$ represents the passive leak current of the membrane, $I_S(t)$ describes the synaptic input received from connected neurons, and $I_{inj}(t)$ describes the injected current into the neuron. The leak current is calculated by

$$I_{leak}(t) = -\frac{C_M}{\tau_M}[+v(t) + V_0] \qquad 2.2.2$$

where $C_M$ represents the membrane capacitance, $V_0$ denotes the resting potential and $\tau_M$ represents the passive membrane time constant.

## 2.3 Firing-Rate models

In some experimental paradigms, the exact time course of each and every neuron in a network might be irrelevant, and the focus might be on the output of average activity output of multiple neurons rather than the activity of individual neurons (137). In surface electroencephalogram (EEG), field potential, and functional magnetic resonance imaging (fMRI), the average firing rate of the local neuronal population is recorded without considering individual neuronal activity. To simulate this type of activity, the firing-rate modeling approach is considered the best choice for modeling. In the firing-rate modeling approach, the average firing rate of the entire network of neurons is represented instead of individual neurons in the network.

These models are also referred to as population models because they deal with a large population of network neurons. The firing rate models were introduced in the 1930s for neural network research, and a comprehensive history of them was written by Cowan and Sharp (138). Many rate models have been developed and successfully used to simulate various activities in large neuronal network (139), (140), (141), (142), (143).

The neural mass models (NMM) are another subtype of rate models used to describe brain functions at a mesoscopic level (144), (145), (146), (147), (148), (149). The NMMs provide an average dynamic of neural ensembles, which offer both biological plausibility and mathematical simplicity (150), (151). These models are widely used for simulating electroencephalogram (EEG) (152). Usually, in NMM, mean membrane potential and mean firing rate of neural ensembles (referred to neural masses) are quantified using differential equations.

## 2.4 NEURON simulator

The differential equations of a neuronal model require a simulation environment to construct and execute this model. Various simulation environments have been developed for this purpose. These simulators offer the ability to construct models of single neuron (with complex morphological and biophysiological properties) as well as large-scale neural network models. Some of these prominent neuronal simulators are NEURON (153), (154), GENESIS (the GEneral NEural SImulation System) (155), NCS (NeoCortical Simulator) (156), XPPAUT (157) , SNNAP (158), (159) are widely used in the field of neuroscience. In this research, we utilized the NEURON simulation environment to develop hippocampal and thalamocortical network models. Therefore, we will provide a brief overview of this simulation environment.

The NEURON simulation environment was presented nearly four decades ago to construct neural network models, comprising neurons with complex anatomical and biophysiological properties that are nearly similar to real neurons. These properties cover the extracellular potential near the cell membrane, different types of channels, and the inhomogeneous distribution of channels. NEURON can handle diffusion reaction models (160), (161) and integrating diffusion functions into cellular networks and synaptic models. Similarly, in NEURON, morphologically detailed

single neuron models demonstrate the spatial diversity of biophysiological and electrical cellular properties. Morphologically, an individual neuron is treated as a tree of unbranched cables, referred to as *sections* and each *section* can have distinct biophysiological parameters from the others. Moreover, each *section* can be discretized into multiple adjacent segments called *compartments* (153). The main purpose of discretization is to achieve more realistic results in the spatial domain. In compartmental models, each neuron can have distinct morphological features, inhomogeneities, and connectivity pattern from other neurons. In a single neuron, the electrical activity of each *section* of the neuron is modeled by using cable equation (162), (160) and the membrane potential is obtained at a specific point in space and time.

The electrical and chemical signals, distributed in space and time, interact with each other through the involvement of neuronal function. The procedures that produce these signals and modulate their interactions have a wide range of diverse properties, such as differences in neuronal cell class, species, and developmental stage (163). The NEURON provides a flexible and powerful simulation environment for developing biophysiological mechanisms using a high-level language called NMODL (Neuron MOdel Description Language). The NMODL was derived from MODL (MOdel Description Language), which was initially developed at NBSR (National Biomedical Simulation Resource) to provide a platform for simulating models for SCoP (Simulation Control Program) (164). NMODL for NEURON was originally implemented by Michael Hines and later extended to generate code for linking with GENESIS. The high-level language NMODL code is passed to a translator that converts and generates this NMODL code into C language code, which is executable in NEURON (160). Furthermore, C language code can also be added to achieve specific goals.

Some essential information of NEURON simulator is provided below.

**NEURON developers:** Michael Hines (Department of computer science, Yale University, USA), John Wilson Moore Late (Duke University, USA), and Ted Carnevale (Yale school of medicines).

***Programming Languages:*** C, C++, and user programs in HOC (High Order Calculator) and/or Python.

***Package compiled binaries:*** Microsoft Windows, Linux, and Mac OS X.

***License:*** Open source.

***URL:*** www.neuron.yale.edu

Chapter 3

# Suppression of SPW-Rs by controlling calcium and gap junctions

Parts of this chapter have been published in Mushtaq et. al, 2021 (165). The hippocampus exhibits a variety of neuronal network oscillations, which are associated with various mnemonic functions. These oscillations are mainly theta (θ; 4–10 Hz), gamma (γ; 30-90) and sharp wave ripples (SPW-Rs; 140-250 Hz). Theta and gamma oscillations appear during spatial searching, acquisition of learning and rapid eye movement (REM) sleep, while SPW-Rs emerge during slow-wave sleep (SWS), immobile state, during eating and drinking, and are essential for memory consolidation processes (59), (56), (166). In rat hippocampus, SPW-Rs are the most consistent oscillatory rhythms having high local field potential amplitude (~1 mV) and high spatial coherence over 1 mm (56), (58), (57). In CA1's stratum radiatum, SPW-Rs are generated due to the synchronous excitatory input from the CA3 pyramidal cells through Schaffer collaterals (59). These Schaffer collaterals initiate high frequency oscillations (ripples; 140-250 Hz) in the CA1 region. The place cells, which fire during spatial searching or explorative behavior, exhibit reactivation during sleep, and in this reactivation period, cells have the same temporal firing pattern as it was during spatial searching (167), (168), (169). Previously stored information reactivation is strongly observed during SPW-Rs in immobile state, slow-wave sleep (170), (171) and rarely during searching (172), (173). This behavior dependent switching of hippocampal network oscillations is an abrupt process.

## 3.1 Suppression of SPW-Rs

Several investigations reveal that variations in cholinergic input to the hippocampus have been involved in these sudden transitions (92), (94), (93). In addition to acetylcholine (ACh), other neuromodulators such as norepinephrine (NE), serotonin (5-HT) also suppress ripple activity in rodents (95), (97), (96). These neuromodulators act via a variety of different receptors involving different signaling cascades and exert multiple effects on hippocampal neurons. NE and 5-HT cause

mild to moderate hyperpolarization of CA3 pyramidal neurons while ACh depolarizes them. Briefly, they modulate synaptic strength and efficacy, alter excitation and inhibition, interfere with transmitter release and reduce calcium influx (98), (99), (100), (101). In spite of having multimodal effects, these neuromodulators suppress SPW-Rs possibly by reducing calcium influx to axon collaterals (95), (97), (93) and altering conductance through gap junctions (60).

### 3.2 Our study purpose

As mentioned above, modulation of calcium influx and electrical coupling play a pivotal role in the suppression of SPW-Rs in different experimental settings. Scientific literature reveals that there are several computational models for the generation of SPW-Rs, but there is not a single report describing the modulation of SPW-Rs based on calcium influx and electrical coupling in pyramidal cells. We evaluated the role of calcium influx and electric conductance through gap junctions on the generation of SPW-Rs. For these evaluations, after SPW-Rs generation, we gradually reduced calcium influx and decreased conductance through gap junctions in the pyramidal cells of our SPW-Rs model and examined the effects of these alterations on the generation of SPW-Rs.

### 3.3 Different SPW-Rs models

The majority of the SPW-Rs models are based on two elements: chemical synapses and gap junctions. Chemical synapses based SPW-Rs models with replay are based on strong synaptic connectivity in recurrent networks (174). These models explain the encoding achieved by spike timing dependent plasticity with phase precession. According to Memmesheimer's model (175), transient ripples can appear in a network of cells linked by excitatory synapses. Taxidis (176) suggested another SPW-Rs model, in which ripple-frequency rhythm in CA1 is generated only in interneurons, which are connected to each other by $GABA_A$ synapses. Traub & Bibbig suggested a SPW-Rs model based on gap junctions. The axons of the pyramidal cells were stimulated by random spikes at low frequency, which generated high frequency (140 Hz or high) rhythms (177). A later model of Traub (178) produced the axonal plexus driven SPW-Rs, where gap junctions were situated in axonal branches away from the soma. In another computational study for declarative

memory formation (179), the SPW-Rs were studied in basket cells network with different transient and noisy excitatory inputs. In recent studies, (179) focused on disinhibition of the CA3 network and the role of interneurons during SPW-Rs activity.

## 3.4 SPW-Rs model for our study

In this study, we chose Vladimirov's model (with small modifications) (91), which possibly provides a bridge between two presently opposite models of SPW-Rs, the first based on gap junctions and the other based on chemical synapses. In this proposed model of ripples, the occurrence of ripples and antidromic spikes are regulated by the input from dendrites of PCs. Slight alterations in somatic potential gate spike transmission from an axonal collateral to the main axon, so that EPSPs can turn on and IPSPs can turn off ripple-associated somatic spikes. Using the same mechanism, the replay in the ripple-associated PCs is demonstrated.

### 3.4.1 CA1 pyramidal cells

The pyramidal cell model of Roger Traub and colleagues (180) was used for the computational simulation of a CA1 network model. In this cell model, six ionic currents were used: (i) fast sodium current, [Na (Fast)], (ii) potassium after-hyper-polarization, $K_{(AHP)}$ (iii) potassium delayed-rectifier, $K_{(DR)}$ (iv) potassium transient current, $K_{(A)}$, (v) high-threshold calcium current, Ca, and (vi) calcium-dependent and voltage-dependent potassium current $K_{(Ca)}$. For the soma-dendritic compartment k, the ionic current was computed by the equation:

$$\begin{aligned} I_{ionic,k} = {} & g_{L,k}V_k + \bar{g}_{Na,k}m_k^2 h_k (V_k - V_{Na}) + \bar{g}_{Ca,k}s_k^2 (V_k - V_{Ca}) \\ & + \bar{g}_{K(DR),k}n_k^2 (V_k - V_K) + \bar{g}_{K(A),k}a_k b_k (V_k - V_K) \\ & + \bar{g}_{K(AHP),k}q_k (V_k - V_K) \\ & + \bar{g}_{K(Ca),k}c_k \times \min\left(1.0, {}^{\chi_k}/_{250}\right) \times (V_k - V_K) + I_{syn,k} \\ & - I_{inj,k} \qquad (1.1) \end{aligned}$$

For the axon-initial segment compartment k, the ionic current was computed by

$$\begin{aligned} I_{ionic,k} = {} & g_{L,k}V_k + \bar{g}_{Na,k}h_k m_k^3 (V_k - V_{Na}) + \bar{g}_{K(DR),k}n^4 (V_k - V_K) + I_{syn,k} \\ & - I_{inj,k} \qquad (1.2) \end{aligned}$$

In the above equations, k denotes the compartment index and $\bar{g}$ represents the maximum conductance for a particular ion in compartment k (given in Table B 3.1). $V_k$ is the local membrane resting potential and $g_{L,k}$ is the leak conductance. The resting potential of given ions is $V_{Na}$ = 115 mV, $V_K$ = -15 mV, $V_{Ca}$ = 140 mV. For the axonal-initial segment (AIS) compartment we have $V_K$ = -25 mV. $\chi_k$ represents the $Ca^{2+}$ in the submembrane shell in arbitrary units. *m*, *h*, *n*, *s*, *a*, *b*, *q*, and *c* are state variables having values between 0 and 1. The dynamics of these state variables is like follows: Let $x_k$ represent a dimensionless state variable *m*, *h*, *n*, *s*, *a* or *b* and $V_k$ represent the membrane potential in compartment k (if $x_k$ represents q then $V_k$ is $\chi_k$). Then these state variables follow the Hodgkin-Huxley (119) like equation:

$$\frac{dx_k}{dt} = \alpha_x(V_k)(1 - x_k) - \beta_x(V_k)x_k \qquad (1.3)$$

where $\alpha_x$ and $\beta_x$ are forward and backward rate functions, presented in Table A 3.1 and 3.2.

Conductance densities of somato-dendrites were taken from the basic model (180) excluding the fast sodium in lower areas of the soma (0.070 S/cm$^2$) to ensure that only a small number of spikes turn into soma spikes (181). The densities of the ionic conductances were the same in all axonal compartments of the main axon, collaterals, and the axonal initial segment (AIS): Na (Fast) 0.3 S/cm$^2$ and potassium delayed-rectifier 0.4S/cm$^2$ (Table B 3.1). The dimensions of the axonal compartments, i.e. AIS, main axon, collaterals, and the two collaterals branched out of the main axon (Fig. 3.1A) were set according to Vladimirov's model (91).

All compartments had the same membrane capacitance of 0.75 μF/cm$^2$. The membrane resistance ($R_m$) for soma and dendrites was $5 \times 10^4$ Ωcm$^2$ and for axonal compartments $10^3$ Ωcm$^2$. The cytoplasmic resistance of the soma and the dendritic compartments was 200 Ωcm and in axonal compartments 100 Ωcm. Leak current reversal potentials ($E_{rev}$) in all compartments were −65 mV. All compartments had 50 mV Na $E_{rev}$. Similarly, K reversal potential was −80 mV in compartments of soma-dendrites, and axonal compartments had −90 mV reversal potential (180). The Reversal potential of AMPA was 0 mV. To suppress spike propagation into the main axon from proximal collaterals, AISs of all PCs except the first three PCs of the network were hyperpolarized by -0.107 nA during resting mode. According to (182), the place cells have a slide somatic depolarization compared to silent cells. In our

model, the first three pyramidal cells played the place cell role and their AISs membrane potentials were set a bit more depolarized than the rest of the pyramidal cells. The AISs of the first three PCs were less hyperpolarized compared of other network cells (for instance, AIS of PC no. 0 was hyperpolarized by -.099 nA). The passive cable length constant $\lambda = \sqrt{\mathrm{aRm}}/2\mathrm{Ra}$ for the apical dendritic shaft was set to 2500 μm, for proximal basal dendrites to 1768 μm, for the main axonal trunk to 158 μm, and for the AIS to 223 μm.

### 3.4.2 Interneuron

A single compartmental model was used for the interneuron (183), which follows the current equation:

$$C_m \frac{dV}{dt} = -I_{Na} - I_K - I_L - I_{syn} + I_{inj} \qquad (3.1)$$

where $C_m$ = 1 μF/cm$^2$ is membrane capacitance, $I_{syn}$ is the synaptic current, $I_{inj}$ the injected current, $I_L$ the leak current ($I_L = g_L(V\text{-}E_L)$ with leak conductance $g_L$ = 0.1 mS/cm$^2$ and a reversal potential, $E_L$ = -65mV) and $Na^+$ and $K^+$ are spike generating voltage dependent ion currents. $I_{Na}$ and $I_K$ follow a Hodgkin and Huxley (119) kinetics. The sodium current is given by

$$I_{Na} = g_{Na}\, m^3 h(V\text{-}E_{Na}) \qquad (3.2)$$

with $g_{Na}$ = 0.035 S/cm$^2$ and $E_{Na}$ = 55 mV. m and h are again state variables. m is an activation variable substituted by the steady function $m_\infty = \alpha_m/(\alpha_m+\beta_m)$ where $\alpha_m(V)$ = -0.1(V+35)/(exp(-0.1(V+35)) – 1) and $\beta_m(V)$ = 4exp(-(*V* + 60)/18). The inactivation state variable h is calculated by a first order kinetics:

$$\frac{dh}{dt} = \phi(\alpha_h(1-h) - \beta_h h) \qquad (3.3)$$

where $\alpha_h(V)$ = 0.07 exp(-(V+58)/20) and $\beta_h(V)$ = 1/(exp(-0.1(V +28)) +1) and ϕ = 5.

The potassium delayed-rectifier current is described by:

$$I_K = g_K n^4(V\text{-}E_K) \qquad (3.4)$$

where $g_K$ = 0.009 S/cm$^2$ and $E_K$ = -90mV. The activation variable n is also calculated by a first order kinetics:

$$\frac{dn}{dt} = \phi(\alpha_n(1-n) - \beta_n n) \qquad (3.5)$$

where $\alpha_n(V)$ = 0.01(V+34)/(exp(-0.1(V + 34)) – 1) and $\beta_n(V)$ = 0.125 exp(- (V +44)/80).

The cell had the same diameter and length of 20 μm.

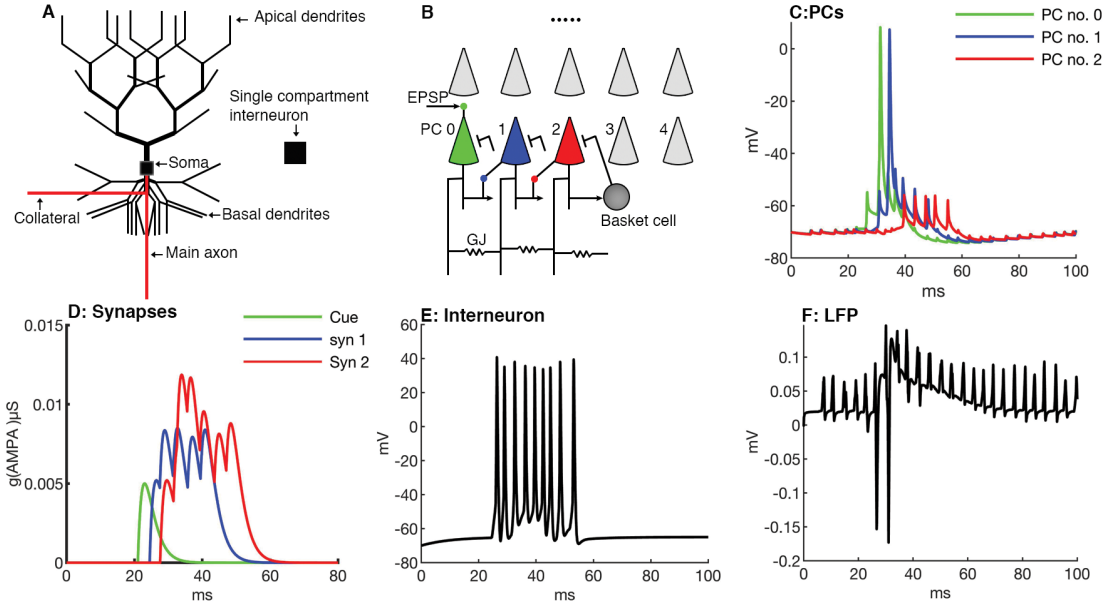


**Figure 3. 1 Network design and simulation of CA1 SPW-Rs.**

***A,*** Schematic model of the pyramidal cell consisting of 64 compartments for soma and dendrites and the interneuron consisting of single compartment. ***B,*** A network of 25 PCs (ten shown) and one interneuron. PC no. 0 receives an excitatory afferent ('cue') in its apical dendrites and starts replay sequentially in PC no. 1 and 2 which are synaptically connected. The distal collateral of PC (i) projects to the basal dendrite of PC (i+1) (i = 0, 1) by an AMPA synapse (Arrows). Proximal collaterals of all PCs are randomly coupled via gap junctions and get random current stimulation. All PCs project to the interneuron by AMPA synapses (Arrows) and the interneuron targets back to the somas of all PCs by inhibitory synapses (blunt arrows). The complete cell connectivity is shown in PC no. 2. ***C,*** PC no. 0 synaptically stimulates PC no. 1 which repeats the previous somatic spike generation cycle of PC no. 0 and generates a spike after ~4 ms following PC no. 0. ***D,*** Excitatory synaptic inputs of the first three pyramidal cells. The first PC receives afferent input (cue) in its apical dendrite and starts to reactivate the synaptically connected cells' sequence (i.e. PC no. 0, 1, 2). ***E,*** Interneuron firing in the network, which receives an input from a PC and generates a spike. ***F,*** Local field potential, which is temporally correlated to synaptic inputs of the first three PCs. The first deep negative spike occurs when PC no. 0 fires, and the ripple cycle occurs when PC no. 1 fires.

### 3.4.3 Synaptic connections in pyramidal cells

The conductance time course in AMPA synapses were chosen according to the alpha-function $g = g_{max}(t/\tau)\exp(-(t-\tau)/\tau)$, which has the maximum conductance $g_{max}$ at the time $\tau$ from start. AMPA targeted pyramidal to pyramidal cells (PC-PC) and pyramidal cells to the interneuron (PC-IN). The parameters of the AMPA synapses from PC-to-PC were $g_{max}$= 52 nS, $\tau$=2 ms, and from PCs-to-IN synapses $g_{max}$= 4 nS, $\tau$= 0.8 ms. The excitatory afferent synaptic input 'cue' to the first PC was set to 5 nS, $\tau$=2 ms, and the Nernst potential was 0 mV. The PCs communicate to the targeted

cells via the distal axonal collateral. The $GABA_A$ synapses, which target to the PCs, are located in the middle of the PCs' soma. The conductance time course for $GABA_A$ synapses from IN to PCs was simulated by a double exponential function $g = g_{max}(\tau_2/\tau_2-\tau_1)(-\exp(-t/\tau_1)+\exp(-t/\tau_2))$, which approaches $g_{max}$ at time $\tau_1\tau_2\log(\tau_1/\tau_2)/(\tau_1-\tau_2)$ after the start. The values of the parameters were $\tau_1 = 2$ ms, $\tau_2 = 5$ ms, $E_{rev} = -75$ mV, and the maximum conductance was $g_{max} = 40$ nS (91).

### 3.4.4 Gap junction connections

In our network model, every PC had three gap junctions (GJ) situated in its proximal axonal collateral. These gap junctions were positioned in a random fashion in the range from 0.25 to 0.75 on the proximal collateral. Different collateral gap junctions were randomly interconnected in the network, with a connection probability independent of the cell distance. Cells were not allowed to make self-connections, but two cells were permitted to have double connections between each other. All pyramidal cells were electrically coupled and no cells were isolated.

### 3.4.5 Network architecture

The network model contained 25 pyramidal cells and one interneuron (Fig. 3.1B). The first PC received an excitatory afferent input into its apical dendrites. We suppose that prior theta oscillations between PCs of CA1 formed some AMPA synapses via LTP (168) Two AMPA synapses made contact between the first three PCs in a feed forward pattern. The first synapse is connected from PC no. 0 to 1, the second one from 1 to 2. Both synapses were set on PCs basal dendrites, 35 μm away from somas and played a gating role for antidromic spikes in targeted PCs and generated antidromic ripples in the CA1 network. All pyramidal cells of the network projected to the interneuron through AMPA synapses (3.5 nS). The interneuron also targeted back to the somas of all PCs through powerful $GABA_A$ synapses (40 nS). The network model was implemented with the NEURON simulation environment (153), (154).

### 3.4.6 Reduction of calcium influx and conductance through GJ

A single pyramidal cell (Fig 3.1A) of model had 11 soma-dendritic branching levels. The calcium conductance densities for the different branching levels was 1 mS $cm^{-2}$

for levels 1-6, 2 mS $cm^{-2}$ for level 7, 3 mS $cm^{-2}$ for level 8-9 and 1 mS $cm^{-2}$ for level 10-11. In the soma, the calcium conductance density was 1 mS $cm^{-2}$ (180). The calcium conductance was gradually decreased in each dendritic level and in the soma with the same proportion to evaluate effects of presynaptic calcium influx on sharp wave ripples. Four simulation results were gathered with different calcium conductances in pyramidal cells: 0% $g_{ca}$, 30% $g_{ca}$, 50% $g_{ca}$, and 100% $g_{ca}$. Similarly, in order to investigate the role of gap junctions on the modulation of SPW-Rs, the conductance through gap junctions was decreased to half (partial reduction) and to complete blockage (full reduction). Calcium conductance was set to 50% and gap junction conductance to 1.6 nS (partial reduction) for obtaining synergistic effects of Ca and gap junctions on SPW-Rs modulation.

## 3.5 Simulation results

In this study, we evaluate the effects of a reduction in calcium influx and electrical coupling on the generation of SPW-Rs in a computational model of these network oscillations. SPW-Rs are generated by a variant of the computational model proposed by Vladimirov and colleagues (91). In a next step, calcium influx and gap junction conductances are gradually decreased during the simulation of SPW-Rs.

### 3.5.1 Simulation of SPW-Rs

In a first step, we simulated a network model with 26 cells, 25 multi compartment pyramidal cells and one interneuron having a single compartment (Fig. 3.1A, 3.1B). In this network, proximal collaterals of pyramidal cells are coupled randomly through gap junctions, and these proximal collaterals are stimulated in a semi random fashion (NetStim.noise = 0.5 in the NEURON simulator) by current insertion via a distal tip (0.042 nA for 3 ms). As a proximal collateral of a single cell is stimulated, all proximal collaterals of the remaining cells participating in the network also generate action potentials synchronously within 0.5 to 1 ms with a frequency of ~250 Hz. All 25 pyramidal cells target to one interneuron and the interneuron targets back to all somas of the pyramidal cells. The first three pyramidal cells of the network are connected by two AMPA synapses. The distal collateral of pyramidal cell (i) targets to the basal dendrite of its next neighboring pyramidal cell (i+1) by an excitatory synapse (Fig. 3.1B). The somatic and axonal both inputs together reach the threshold

and generate an action potential, which propagates in both directions: antidromic and orthodromic. In result of the antidromic propagation, the soma of PC no. 0 generates a spike. By this mechanism, one cell activates another cell by EPSP and, similarly, the other cell develops an EPSP in chain on replay basis (Fig. 3.1C). According to Lee (182) place cells have a more somatic depolarization 'hill' compared to the silent cells. In our model, the somas and AISs of the first three PCs of the network had more depolarization than the other twenty-two pyramidal cells. When the AIS of PC no 0 gets strong input from proximal collaterals in combination with maximum gap junctions input, its reaches the threshold because of less hyperpolarization as compared to other cells, which leads to an action potential. This process produces second and so forth SPW-Rs (Fig. 3.2D).

The first PC of the network receives an excitatory afferent input (cue) into its apical dendritic shaft, and it starts firing and delivers EPSPs to the next cell, which also starts firing after a short delay (~ 4 ms). Similarly, the third cell also fires but produces only spikelets (Fig. 3.1C). Initially, only the first three synaptically connected PCs participate in the SPW-Rs generation (Fig. 3.1F). If any pyramidal cell fires it triggers the interneuron, which also fires following that pyramidal cell (Fig. 3.1E). This is consistent with the experimental results that excitatory postsynaptic currents (EPSCs) and inhibitory postsynaptic currents (IPSCs) in pyramidal cells are phase-locked to the ripples, and IPSCs follow EPSCs (62). The remaining 22 pyramidal cells are axonally linked to the other pyramidal cells via gap junctions. The proximal collaterals are stimulated by a current injection of 0.042 nA for 3 ms.

### 3.5.2 Suppression of calcium influx

Before proceeding with the results, we want to mention that in all simulation results, spikes or spikelets mean somatic spikes or spikelets (shown in Figures' spike raster). Reduction in calcium influx weakens the strength of chemical synapses in pyramidal cells (Fig. 3.2A). Due to these weaker synapses, the targeted cells fire with a time delay or cannot produce complete spikes (Fig. 3.2B) at all. Reduction in calcium influx by 50% causes a 1.8 ms delay in the spike generation of PC no. 1 (Fig. 3.2B). Consequently, the second SPW-R appears ~ 40 ms later than in the normal network (Fig. 3.2D and 3.2E). A further decrease in calcium influx (30% of the normal

calcium influx) results in an even longer delay in firing of PC no. 1, which now fires 3.86 ms later as compared to normal calcium influx. Similarly, there is a marked delay of ~420 ms in the appearance of the second SPW-Rs (Fig. 3.2D and 3.2F). In the next step, calcium is completely suppressed, PC no. 1 does not produce any spike, however, spikelets are generated (Fig. 3.2B & 2G spike raster) and PC no. 2 does not generate even any spikelet (Fig 3.2G spike raster). In addition it decreases the amplitude and the number of ripples. The duration and the incidence of sharp waves are also decreased (Fig. 3.2C). Moreover, in this paradigm, the network does not produce a second SPW-R (Fig. 3.2G). The number of SPW-Rs in the network simulations is 4, 3, 2 and 1 at 100%, 50%, 30% and 0% calcium influx, respectively (Fig. 3.2D-G also Fig. 3.4C) in 650 ms.

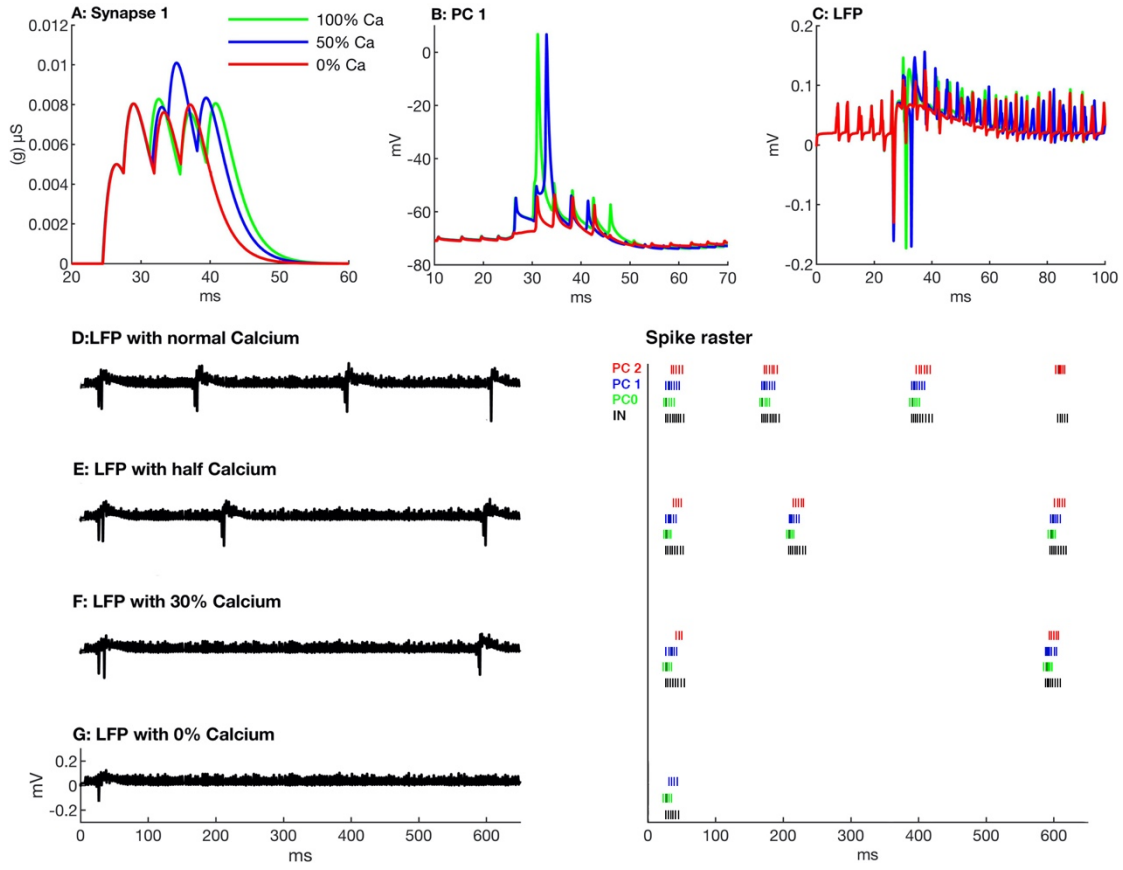


**Figure 3. 2 Effects of suppression of calcium influx on SPW-Rs.**

***A,*** Calcium suppression effects on synapse no. 1, which makes a connection from PC no. 0 to PC. no. 1. Note that when calcium is decreased, the strength of the synapse is also decreased, which causes a delayed activation of the targeted PC or a suppression of spikes. ***B,*** PC no. 1 firing behavior with different calcium quantities. With gradual calcium suppression it takes more time to produce a spike. Complete calcium suppression leads to spikelets (red). ***C,*** Local field potentials for different calcium

influxes showing less ripples in sharp waves. ***D-G,*** Local field potentials (left) and spike raster of the first three PCs (right thick and dark ones are spikes and thin ones are spikelets) during different calcium influxes in pyramidal cells of the network. Note that gradual calcium suppression in PCs decreases the number of SPW-Rs.

### 3.5.3 Reduction in gap junction conductance

In another series of simulations, we studied effects of variations in gap junction conductance on network oscillations. As we mentioned earlier, when a proximal collateral is stimulated it generates an action potential in collateral. All other proximal collaterals of the network fire action potentials synchronously within 0.5 to 1 ms (Fig. 3.3A). We observe that a reduction in electrical conductance through gap junctions reduces the synchronous activity of proximal collaterals of pyramidal cells (Fig. 3.3B, 3.3C). Partial or full reduction in conductance through gap junction in proximal collaterals disturbs the temporal correlation among axonal and AIS inputs. Consequently, it weakens the strength of synapses (Fig. 3.3D) because of inadequate proximal collateral input. This weakened synaptic strength during partial reduction causes 1.62 ms delay in PC no. 1 compared to a normal network with normal gap junction conductance (Fig. 3.3E). PC no. 0 also generates a spike with a time delay of 1.1 ms with partial conductance (half blocked gap junction). Moreover, the number of spikelets also decreases in this scenario (Figure 3.3H, 3.3I spike raster). Consequently, the second SPW-Rs with partial conductance appears ~ 182 ms (Fig. 3.3H) later than the respective SPW-Rs in a normal network (Fig. 3.3G). PC no. 1 produces only one spikelet during complete gap junction blockage (Fig. 3.3C, 3.3E), and PC no. 0 produces a spike with a delay of 2.3 ms and generates even fewer spikelets (one) than the normal GJ network (four spikelets) (Fig. 3.3G and 3.3I raster plot). Proximal collaterals produce temporally unsynchronized action potentials during the complete gap junction blockage (Fig. 3.3C). These sparse proximal collaterals' spikes don't make temporal coordination with somatic synaptic activities and, therefore, PC no. 1 cannot generate an action potential. These sparsely distributed proximal axonal action potentials decrease the amplitude of ripples and produce high frequency jittery pulses (Fig. 3.3F).

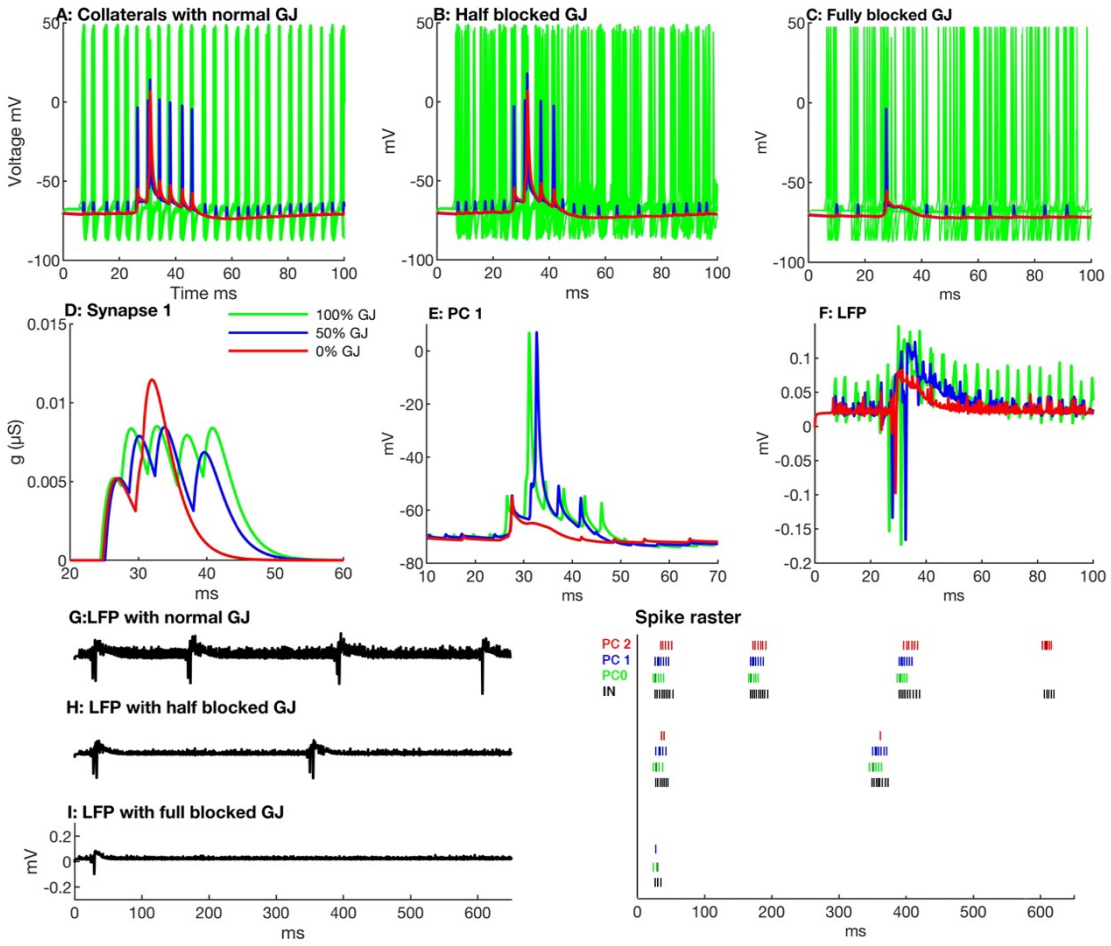


**Figure 3. 3 Effects of reduction in conductance through GJ on SPW-Rs.**

***A,*** Proximal collaterals (green) of the first ten PCs with normal conductance generate synchronous action potentials, which are temporally coherent to AIS (blue) and somatic input (red) of PC no. 1. ***B,*** Partial conductance through gap junctions leads to a decreased synchronous activity of the proximal collaterals, which also decreases the temporal correlation between somatic, AIS, and axonal inputs. Therefore, PC no. 1 produces only two spikelets after a spike (red), in contrast to four spikes with normal conductance. ***C,*** Proximal collaterals exhibit a sparse firing activity with fully blocked gap junctions. AIS and axonal input do not correlate enough to reach the threshold, hence, the soma of PC no. 1 produce only one spikelet. ***D,*** Synapse no. 1 looses its strength with gap junction blockage and causes a delay in the next SPW-Rs generation. ***E,*** The firing behavior of PC no. 1 during normal conductance, partial and complete GJ blockage. The cell produces a spike with delay and only two post-spikelets with partial conductance, and it does not produce any spike but only one spikelet at all with complete GJ blockage. ***F,*** The local field potentials (LFP) with partial and full GJ blockage exhibit ripples with small amplitude because of unsynchronized proximal collateral action potentials. **G-I,** LFPs (left) and spike raster of first three PCs (right thick and dark ones are spikes and thin ones are spikelets) with normal, partial, and complete gap junction blockage in the pyramidal cells. Partial and complete GJ blockages also decrease the number of spikes and spikelets during SPW-Rs.

### 3.5.4 Synergistic effects of reduction in calcium influx and GJ conductance

According to the above results, the suppression of calcium influx or electrical conductance through gap junctions in pyramidal cells suppresses SPW-Rs. Calcium suppression decreases the strength of synapses, whereas the blockage of gap junctions decreases the synchronized activities of proximal collaterals. Weak coordination between proximal collaterals and AIS input also weakens the strength of synapses. In set of simulations, we investigated the combined effects of gradually reduced calcium influx and gap junction conductance on SPW-Rs. The simulation with 75% Ca and 75% GJ conductance shows approximately the same results as with 50% Ca suppression (Fig. 3.2E and 3.4D). Three SPW-Rs occur at time 27 ms, 216 ms, and 539 ms, respectively. In another simulation with simultaneous 65% Ca and GJ conductance, the network generates only two SPW-Rs (Fig. 3.4E), the first at time 27 ms and 2$^{nd}$ at 341 ms after the start of the simulation.

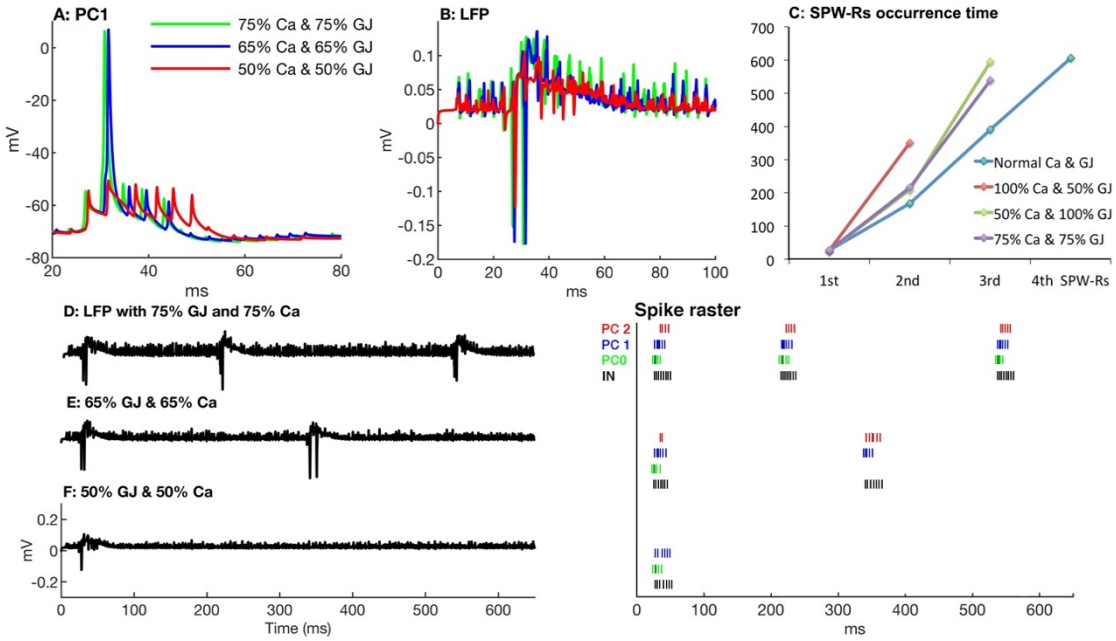


**Figure 3. 4 Synergistic effects of calcium and GJ blockage.**

***A,*** PC no. 1 shows a spike delay with 65% calcium influx and 65% gap junction conductance (blue) as well as with 50% calcium and 50% gap junction blockage (red). ***B,*** Partial blockage of gap junction conductance (50%) and calcium influx (50%) affects the number of ripples and their amplitude (red). ***C,*** First, second, and so forth SPW-Rs occurrence time with different level of calcium and gap junction conductances. ***D-F,*** LFPs (left) and spike raster (right) with 25% suppression of Ca and 25% blocked GJ (***D***) 35% suppression of Ca and 35% blocked GJ (***E***) and 50% blockage of both Ca and GJ (***F***). Note that during 650 ms, the network doesn't generate a second SPW-R and PC no. 2 does not produce any spike or spikelet during a 50% simultaneous reduction of calcium influx and gap junctions' conductance.

With simultaneous 50% suppression of Ca influx and gap junction blockage, PC no. 1 generates only spikelets and not, a spike, conversely it produces a complete spike in individual partial suppression of Ca (Fig. 3.2B) or gap junction blockage (Fig. 3.3E). Disturbance in synchronized proximal collateral activity and weakness in synaptic strength are further increased resulting in a marked delay in spiking and decrease in the number of spikelets of PC no. 0 and 1. PC no. 2 does not produce even any spikelet (Fig 3.4F spike raster plot). However, amplitude and incidence of the ripples are similar to the partially blocked gap junction network because of sparse proximal collateral activities. The network does not generate a second SPW-Rs within 650 ms (Fig. 3.4F). Interestingly, we observed that 50% blockage of gap junctions together with 50% calcium suppression had a stronger effect on SPW-Rs suppression than the individual effects of 50% Ca influx or gap junction blockage.

## 3.6 Results summary

From these observations and findings we conclude that a sudden switching of behavioral dependent oscillatory patterns of the hippocampal neurons partially depends on the combined effects of decreased calcium influx and reduced gap junction coupling along with possible postsynaptic mechanisms like an imbalance of depolarization and hyperpolarization, mainly caused by increased cholinergic input.

Chapter 4

# Differential thalamocortical interactions in slow and fast spindle generation

Parts of this chapter have been published in Mushtaq et. al, 2022 (184). Sleep plays an important role in memory consolidation. Two thalamo-cortical oscillatory rhythms, the sleep slow oscillations (SO) and sleep spindles of non-rapid eye movement (NREM) sleep play a comprehensive role in declarative memory consolidation (185), (113), (186). It is believed that cortical SOs provide a temporal frame where recently-acquired memory can be replayed, and transferred to cortical regions for long-term memory storage (5), (3), (187). During sleep spindles, which occur endogenously in temporal association with both the SO and hippocampal sharp wave ripples (188) processes of long-term potentiation and synaptic plasticity take place (189), (103), (190). During the large amplitude SOs so-called Up states the majority of cortical neurons fire or become depolarized and maintain this depolarized state for several hundred milliseconds. Conversely, during the Down state, virtually all cortical neurons remain silent or exhibit a hyperpolarized state for a few hundred milliseconds (31), (36), (34), (35).

## 4.1 Fast and slow sleep spindles

In humans, sleep spindles are classified into two categories: fast spindles (12-16 Hz) and slow spindles (8-12 Hz), with differential properties. Fast spindles are well studied regarding their origin, generating mechanism, functional role, temporal, and spatial appearance in different cortical regions (49), (50), (51), (18). Slow spindles – mainly found in human deep sleep EEG – have been less extensively studied and their source, generation, and functional roles remain unclear. Some pharmacological and computational studies suggest that slow spindles may rely relatively more on cortical and less on thalamic sources as compared to fast spindles (191), (192). On the other hand, the level of thalamic hyperpolarization has been suggested to affect differences in spindle frequency, and other spindle properties (193). Bastuji et al. (194) using intrathalamic EEG recordings in humans, observed a significantly slower

spindle frequency (11.89 Hz) in the ventral lateral posterior (VLp) thalamic nucleus as compared to other local posterior thalmic nuclei. Most interestingly the VLp was the most anterior of the recorded thalamic nuclei, and projects to the frontal cortical region.

## 4.2 Study purpose

In this study, we present a thalamocortical computational model for NREM sleep that exhibits both fast and slow spindles along with the SO rhythm. Fast and slow spindles are simulated in two independent fast and slow thalamocortical sub-networks, whereby each interacts with its own reticular sub-networks (195). In the model both cell layers (TC and RE neurons) of the thalamic network for slow spindles are set to a more hyperpolarized level than the fast thalamic network. Our model provides a platform to investigate the interactive role of both fast and slow spindles during NREM sleep. Model results suggest that the role of slow spindles may be to facilitate ongoing cortical SO activity.

## 4.3 Thalamocortical model for our study

In this study, a conductance based thalamocortical model for NREM sleep was extended from existing model (33). All network neurons were modeled by Hodgkin-Huxley kinetics. Synaptic current calculations were based on first and higher-order synaptic activation schemes. Standard intrinsic currents and their conductance are described in Table A 4.1 and Table B 4.1. The synaptic currents developed and balanced for SOs and both spindles are given in Table B 4.2. Our thalamocortical network model incorporates three interactive sub-networks (Fig 4.1). The first is a cortical network for SOs comprising pyramidal cells (PY) and interneuron (IN). The second and third sub-thalamic networks are for fast and slow spindles, respectively. Each sub-thalamic network is comprised of a thalamocortical/relay (TC) and reticular (RE) cell layer.

### 4.3.1 Cortical intrinsic currents

The pyramidal and interneuron cells of the cortex are modeled as two separate compartments (dendritic and axosomatic compartment) as initially proposed by Mainen and Sejnowski (196) based on Hodgkin-Huxley kinetics (33).

$$C_m \frac{dV_D}{dt} = -g_L(V_D - E_L) - g_{SD}(V_D - V_S) - I_D^{int} - I^{syn},$$
$$0 = -g_{DS}(V_S - V_D) - I_S^{int} \quad (4.1)$$

In equation 1, $C_m$ and $g_L$ are the membrane capacitance and leakage conductance of the dendritic compartment. $E_L$ is the reversal potential, $V_D$ the dendric and $V_S$ is the axosomatic compartment membrane potential. $g_{SD}$ and $g_{DS}$ are the conductances between the axosomatic and dendritic compartments, respectively and g_SD = 1/(R*$S_{soma}$ *165) and g_DS = 1/(R*$S_{soma}$) where R = 10 MΩ and $S_{soma}$ = 1.0*$10^{-6}$ $cm^2$. $I_D^{int}$ is the sum of active dendritic, $I_S^{int}$ the sum of active axosomatic currents and $I^{syn}$ the sum of synaptic currents. $I_D^{int}$ and $I_S^{int}$ are the sum of the following intrinsic currents:

$$I_D^{int} = I_{Na} + I_{Na(p)} + I_{LK} + I_{HAV} + I_{Kca} + I_{Km},$$
$$I_S^{int} = I_{Na} + I_{Na(p)} + I_K.$$

Thereby, $I_{Na}$ represents the fast sodium current, $I_{Na(p)}$ the persistent sodium current, $I_{LK}$ the potassium leak current, $I_{HAV}$ the high-threshold calcium current, $I_{Kca}$ the slow calcium-dependent potassium current, $I_{KM}$ the slow voltage-dependent non-inactivating potassium current and $I_K$ represents the delayed rectifier potassium current. The IN cell compartments have the same intrinsic currents except for $I_{Na(p)}$ that is only included in PY cells, The ratio of dendritic area to somatic area was set to $\rho$ =165 in PY cells, and to $\rho$ =50 in IN cells. All voltage-dependent currents $I_c$ were simulated in the same fashion:

$I_c = g_c m^M h^N (V - E_c)$

where $g_c$ is the maximum conductance, $m$ is an activation gating variable, $M$ is the number of activation gates, $h$ is an inactivation gating variable, and $N$ is the number of inactivation gates. $V$ is the corresponding compartment voltage and $E_c$ is the reversal potential. The dynamics of all gating variables were solved with the same equations:

$$\frac{dy}{dt} = -\frac{x - x_\infty}{\tau_x}$$
$$\tau_x = (1/(\alpha_x + \beta_x))/Q_T$$
$$x_\infty = \alpha_x/(\alpha_x + \beta_x)$$

where x is a gating variable, $x = m$ or $h$, the temperature-related term, $Q_T = Q^{((T-32)/10)}$ = 2.9529 where Q = 2.3, T = 36° C. $\alpha_x$ and $\beta_x$ are voltage-dependent transition rates. All individual intrinsic currents are described in Table A 4.1 and their units and parametric values are described in Table B 4.1.

### 4.3.2 Thalamic intrinsic currents

Two separate sub-thalamic networks for fast and slow spindles, respectively, were developed, each with a thalamocortical/relay (TC) and reticular (RE) cell layer. Cells of each layer were modeled based on a single compartment (somatic compartment) using the same voltage-dependent and calcium-dependent currents dynamics as expressed by Hodgkin-Huxley kinetics schemes (33):

$$C_m \frac{dV}{dt} = -g_L(V - E_L) - I^{int} - I^{syn}, \qquad (4.2)$$

where $C_m$ is the membrane capacitance, $g_L$ the leakage conductance, $E_L$ the reversal potential, and $V$ the voltage of the compartment. $I^{syn}$ denotes the sum of the synaptic currents and similarly $I^{int}$ the sum of the active intrinsic currents. The sum of these active currents for TC, $I_{TC}^{int}$ and RE, $I_{RE}^{int}$ are described as

$$I_{TC}^{int} = I_{Na} + I_k + I_{KL} + I_h + I_T,$$

$$I_{RE}^{int} = I_{Na} + I_K + I_{KL} + I_T.$$

here $I_{Na}$ represents the fast sodium current, $I_K$ the fast potassium current (197), $I_{KL}$ the potassium leak current, $I_h$ the hyperpolarization-activated cation current (198), $I_T$ the low-threshold calcium current in TC (124) and $I_T$ in RE neuron (123). The potassium leak current is $I_{KL} = g_{KL}(V\text{-}E_{KL})$ in both TC and RE cells where $g_{KL}$ is potassium leak conductance and $E_{KL}$ is the potassium reversal potential ($E_{KL}$ = -95 mV). Calcium dynamics for thalamic cells is described by;

$d[Ca]_i/dt = -AI_T + ([Ca]_\infty - [Ca]i)/\tau$,

where $[Ca]_\infty = 2.4 * 10^{-4}$ mM, $A = 5.1819 * 10^{-5}$ mM cm$^2$/(ms μA) and τ = 5ms.

All individual voltage-dependent currents were simulated in the same fashion as the cortical intrinsic currents given in Table A 4.1. Table B 4.1 gives the parametric values developed in our model.

### 4.3.3 Synaptic currents

For synaptic signaling four types of synaptic currents, $I_{syn}$ were used, three (AMPARs, $GABA_A$Rs, and NMDARs) were modeled by the first-ordered activation scheme (199), (37). Accordingly, these synaptic currents are given by

$$I_{syn} = g_{syn}[O]f(V)\big(V - E_{syn}\big) \qquad (4.3)$$

where $g_{syn}$ is the maximal synaptic conductance, $[O]$ is the fraction of open channels and $E_{syn}$ is the synaptic reversal potential. For AMPARs and NMDARs, $E_{syn}$ = 0 mV, whereas for $GABA_A$Rs, $E_{syn}$ = -70 mV. For AMPARs and $GABA_A$Rs $f(V)$ =1, for the NMDARs, the voltage-dependent sigmoidal function $f(V) = 1/(1 + \exp(-(V - V_{th})/\sigma))$ was used (197), (199), where $\sigma$ =12.5 mV, $V_{th}$ = -25 mV. The fraction of open channel $[O]$ was computed by the following equation:

$$d[O]/dt = \alpha(1 - [O])[T] - \beta[O],$$

$$[T] = A\theta(t_0 + t_{max} - t)\theta(t - t_0)$$

where $t_0$ is the time for receptor activation and $\theta(x)$ is the Heaviside function (200). The duration and amplitude parameters for the neurotransmitter pulse are $t_{max}$ = 0.03 ms and A = 0.5. The synaptic current rate constants for AMPARs were $\alpha$ = 1.1 ms and $\beta$ = 0.19 ms, for $GABA_A$Rs $\alpha$ = 10.5 ms and $\beta$ = 0.166 ms, and for NMDARs $\alpha$ = 1 ms and $\beta$ = 0.0067 ms. Intracortical currents were modified by multiplying the short-term depression term "*D"* (201), (127) with the maximal synaptic conductance in equation 3 for AMPARs and $GABA_A$Rs receptors:

$$I_{syn} = Dg_{syn}[O]f(V)\big(V - E_{syn}\big),$$

where D is the amount of available synaptic resources, calculated by the following scheme:

$$D_{n+1} = 1 - \big(1 - D_n(1 - U)\big)\exp\left(-\frac{\Delta t}{\tau}\right),$$

where the synaptic resources time recovery is $\tau$ = 700 ms, the interval between *nth* and $(n+1)\,\Delta t$, and the fraction of resources used for each action potential is $U$ (for AMPARs $U$ = .07, for $GABA_A$Rs $U$ = .073).

The fourth synaptic current, $GABA_B$Rs is computed by a higher-ordered activation scheme that involves potassium channel activation by a G-protein, (199), (202):

$$I_{GABAB} = g_{GABAB}([G]^4/([G]^4 + K))/(V - E_K)$$

$$d[R]/dt = K_1(1 - [R])[T] - K_2$$

$$d[G]/dt = K_3[R] - K_4[G],$$

where [G] reflects the G-protein concentration, [R] the fraction of activated receptors, and the potassium reversal potential $E_K$ = -95 mV. K1 = 0.052 $m_M^{-1}ms^{-1}$, K2 = 0.0013 $ms^{-1}$, K3 = 0.098 $ms^{-1}$, and k4 = 100 $\mu_M^4$ were the rate constants. The maximal synaptic conductance used here for each synapse is described in Table B 4.2.

### 4.3.4 Network geometry

The network model is comprised of six one-dimensional layers of neurons (Fig 4.1). Each layer of cells has N neurons, (N = 40) except the PY neurons layer, which has 5N neurons (200 neurons) (203). The first and second cortical layer of PY and IN neurons initiate SOs. The third and fourth are thalamic layers for fast spindle initiation, and similarly the fifth and sixth are also thalamic layers that initiate slow spindles. The radii of synaptic connections between different layers are described in Table B 4.2. For each SO cycle initiation, EPSPs and IPSPs miniature currents were implemented to PY-PY, PY-IN and IN-PY cells via AMPARs and $GABA_A$Rs receptors (204). These mini currents emerge ~ 100 ms after the start of the SO downstate. For Poisson input implementation, NetStim.noise was set to 1 in the NEURON simulator.

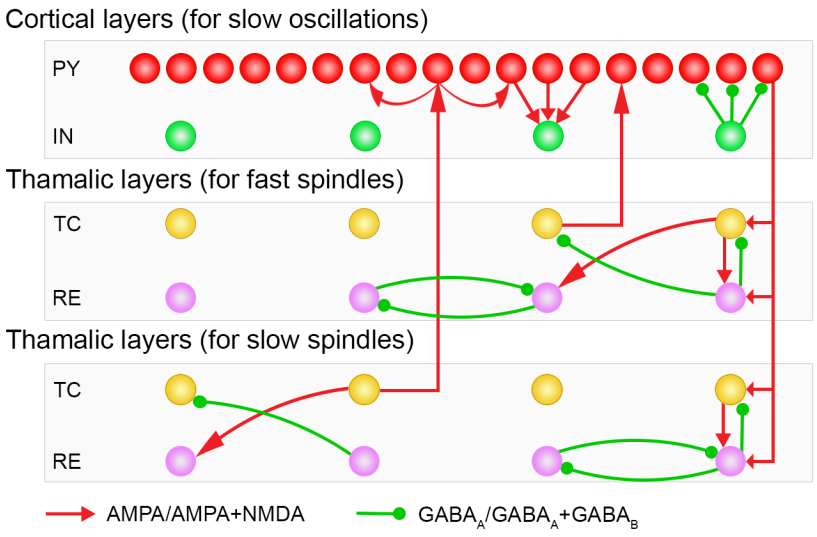

**Figure 4. 1 The thalamocortical network geometry and connection scheme.**

The network is comprised of six cell layers. The top two consist of cortical PY and IN neurons. The middle two layers are thalamic TC and RE neurons for fast spindle generation, and the bottom two thalamic TC and RE neuron layers generate slow spindles. The cortical PY cells layer contains 200 neurons, all other layers contain 40 neurons. Small green-filled circles symbolize $GABA_ARs$ or $GABA_ARs$+ $GABA_BRs$, and corresponding connections. Red arrowheads represent correspondingly AMPARs or AMPARs+ NMDARs receptors.

## 4.4 Simulation results

Our model exhibits both fast and slow spindles along with SOs. Both fast and slow spindles were initiated in two separate thalamic subnetworks. The main network comprises six layers of cells (Fig 4.1), the top two of which are cortical layers of PY and IN cells for SOs, while the middle two are thalamic layers of TC and RE cells that initiate the fast spindles ('fast thalamic network') and the lower two layers are for slow spindles ('slow thalamic network'). The thalamic subnetwork for slow spindles has the same type of intrinsic and synaptic current dynamics and network architecture as the fast thalamic subnetwork, however, it has a larger hyperpolarization than the fast thalamic subnetwork. Hyperpolarization of the slow thalamic subnetwork was increased by setting the reversal potential of $GABA_ARs$ to $E_{GABAA}$ = -88 mV in TC cells. The reversal potential of passive currents was set to $E_L$ = -77 mV in TC cells and $E_L$ = -82 mV in RE cells.

### 4.4.1 Initiation of slow oscillations

The main thalamocortical network is initiated by mini synaptic current to both cortical layers during the hyperpolarized Down state. Once the SO cycle is initiated, the mini synaptic current is terminated. During the Down state, the mini synaptic current activates the persistent sodium current of PY neurons and consequently these PY neurons depolarize and reach firing threshold. Initially only one or few PY neurons generate an action potential, yet they target their neighboring PYs by strong PY-PY excitatory connections. Due to the strong PY-PY excitatory connections and persistent sodium current they sustain this depolarized Up state for 500-1000 ms. The calcium dependent potassium current and progressive synaptic depression terminate the depolarized Up state and bring cortical network back to the Down state. After ~100 ms of terminating the SO cycle, the mini synaptic current is again

activated for the next SO cycle initiation and similarly this process is repeated for each SO cycle.

### 4.4.2 Initiation of spindles generation

As the cortical network is activated, both layers of the fast thalamic subnetwork (TC and RE cells layers) also receive cortical inputs and become active. In the fast thalamic network, the interaction of TC and RE cells produces fast spindle oscillations with a major contribution of the TC hyperpolarization current ($I_h$) and transient calcium current ($I_T$) (45). The fast thalamic output is sent back to the cortical network by TC cells. The cortical network receives this fast thalamic feedback ~200 ms after the initiation of the SO cycle (Fig. 4.2). The thalamic network for slow spindles receives cortical inputs with a 600 ms time delay (600 ms after the initiation of SO). Hyperpolarization of the slow thalamic network was increased by setting the reversal potential of $GABA_AR$s to $E_{GABAA}$ = -88 mV in TC cells. The reversal potential of passive currents was set to $E_L$ = -77 mV in TC cells and $E_L$ = -82 mV in RE cells. This more hyperpolarized thalamic network produced slow spindle oscillations that send excitation back to the cortical network via TC cells. The cortical network receives this slow thalamic input ~800 ms after the initiation of the SO cycle (Fig. 4.2 bottom two raster plots of entire slow thalamic network activity, left, and unit activity, right). Cortical LFP was calculated as the sum of the presynaptic currents (AMPARs, NMDARs, $GABA_AR$s) of PY cells. The resultant cortical local field potential (LFP) is depicted in Figure 4.3.

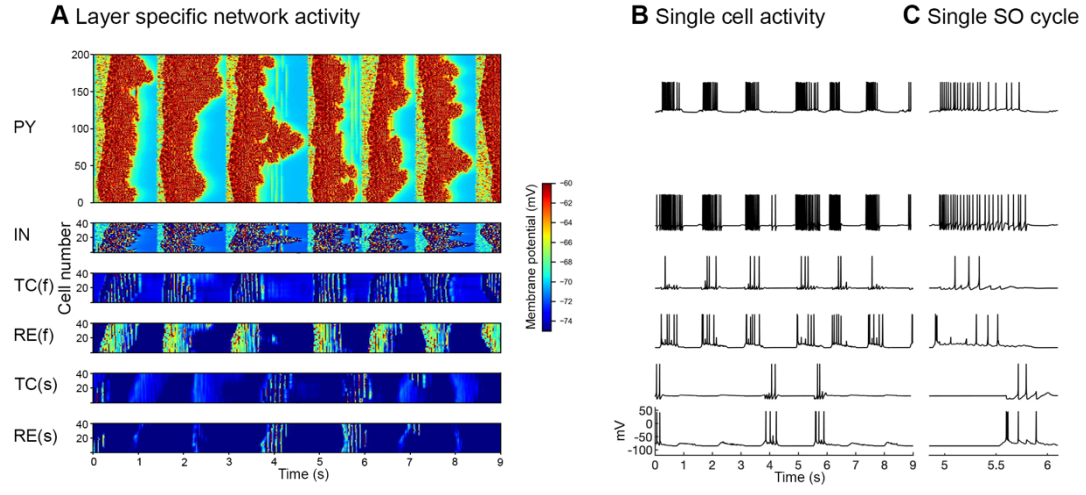


**Figure 4. 2 Layer specific network activity**

***A***, Space-time raster plots show the simultaneous activity of each neuron layer (200 PY, 40 IN, and 40 cells in each thalamic layer). The membrane potential of each cell is color coded. TC(f) and RE(f) represent thalamocortical and reticular cells of the fast thalamic network and similarly TC(s) and RE(s) represent thalamocortical and reticular cells of the slow thalamic network. ***B***, Corresponding single-cell activity of each neuron layer. Slow thalamic cells respond relatively seldom (bottom two) compared to the cells of the fast thalamic network. ***C***, Zoomed LFP and single cell activity of one SO cycle.

The LFP was smoothed using the function; filter() (MATLAB) with a window size of 200 for better visualization of spindles, nested with the cortical LFP (Fig. 4.3B). The fast thalamic input (Fig. 4.3C and D, red) projected to the cortical network ~200 ms after the initiation of the SO cycle, whereas the slow thalamic input (Fig. 4.3C and D, green) projected to the cortical network ~800 ms after the initiation of the SO cycle, nearly a few hundred ms before the termination of the SO cycle. Similarly, the fast thalamic inputs were found in every SO cycle but the weaker inputs did not have an impact on the cortical LFP (Fig. 4.3D 2$^{nd}$ to 4$^{th}$ SO cycle).

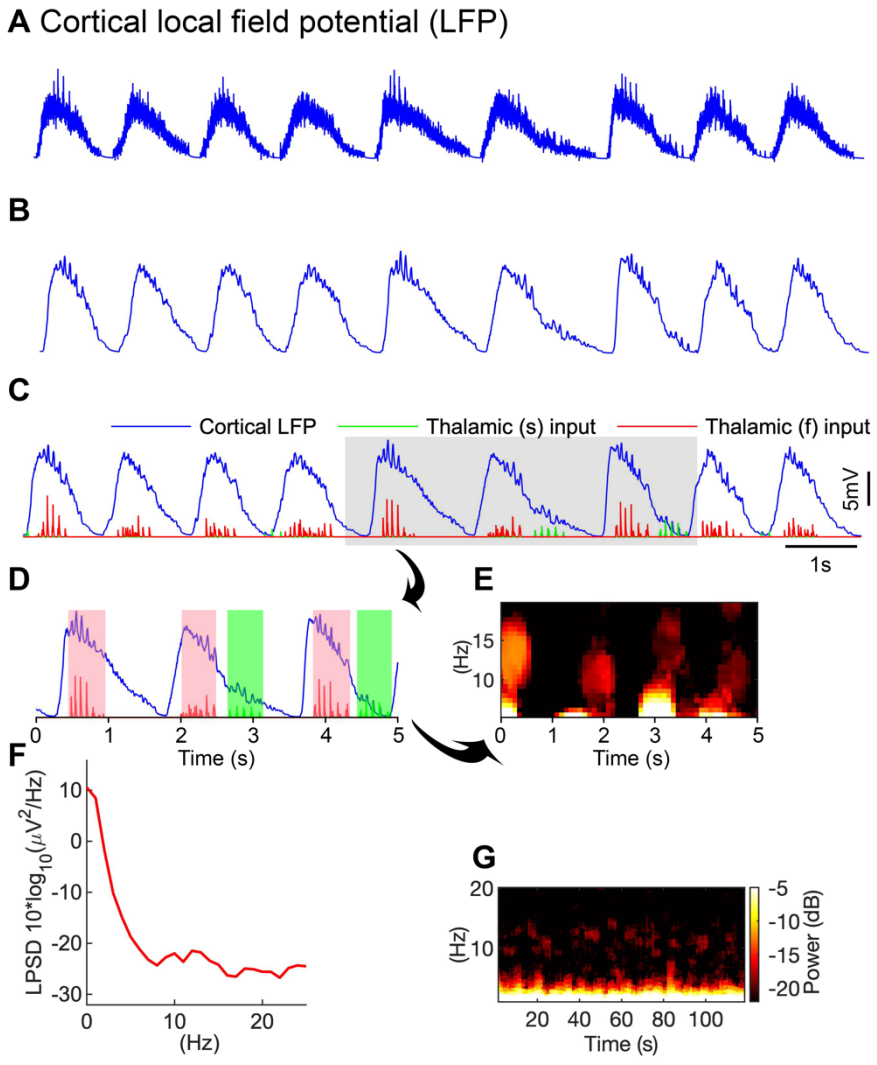

**Figure 4. 3 Resultant cortical local field potential (LFP).**

***A***, Cortical LFP calculated as the sum of presynaptic currents (AMPARs, NMDARs, $GABA_ARs$) of PY cells. ***B***, Smoothed LFP revealing up and down SO states more clearly. ***C***, Spontaneously occurring Cortical LFP indicating times of both thalamic synaptic inputs. The occurrence of slow and fast spindles varies during long time simulations. The 'fast thalamic' input (red) responsible for fast spindle generation occurs at the SO down-to-up state transition SO. The slow thalamic input (green) is responsible for slow spindle generation and occurs at the SO up-to-down state transition. ***D***, zoomed figure of C indicating fast thalamic spindle (red) input nested within the first SO-half (pink filled box, time period of ~500 ms). The green input and green filled box describe slow thalamic input and its time period. ***E***, time-frequency spectrogram (calculated by short-time moving window Fourier transform) (range, 5-20 Hz) of LFP, for shaded area (panel E) indicates the bands of fast and slow spindles. ***F***, Log power spectrum of the LFP across the time period of 120 s, exhibiting power in the SO (~1 Hz), slow spindle (8-12 Hz), and fast spindle (12-16 Hz) frequency bands. ***G***, time-frequency spectrogram (range 0-25 Hz) of the LFP of 120 seconds duration indicates SO, fast and slow spindle activity.

Moreover, in the temporal window the thalamic inputs with a lifetime of less than 0.5 seconds were not considered proper spindles. In normal simulations, the number of fast spindles was high compared to that of slow spindles (see Fig 4.3C above). In our slow spindles results, generally the waning phase of the slow spindle was completed before the completion of the SO cycle, although sometimes a few spikes of the waning phase were also observed after the completion of the SO cycle, i.e. in the down state of the SO. Sometimes slow spindles initiated the second SO cycle before the completion of the preceding SO cycle (Fig 4.4B $6^{th}$ and $8^{th}$ SO cycle). Slow spindles initiated approximately 10% of SO cycles during normal or control simulation (See Fig 4.5I below).

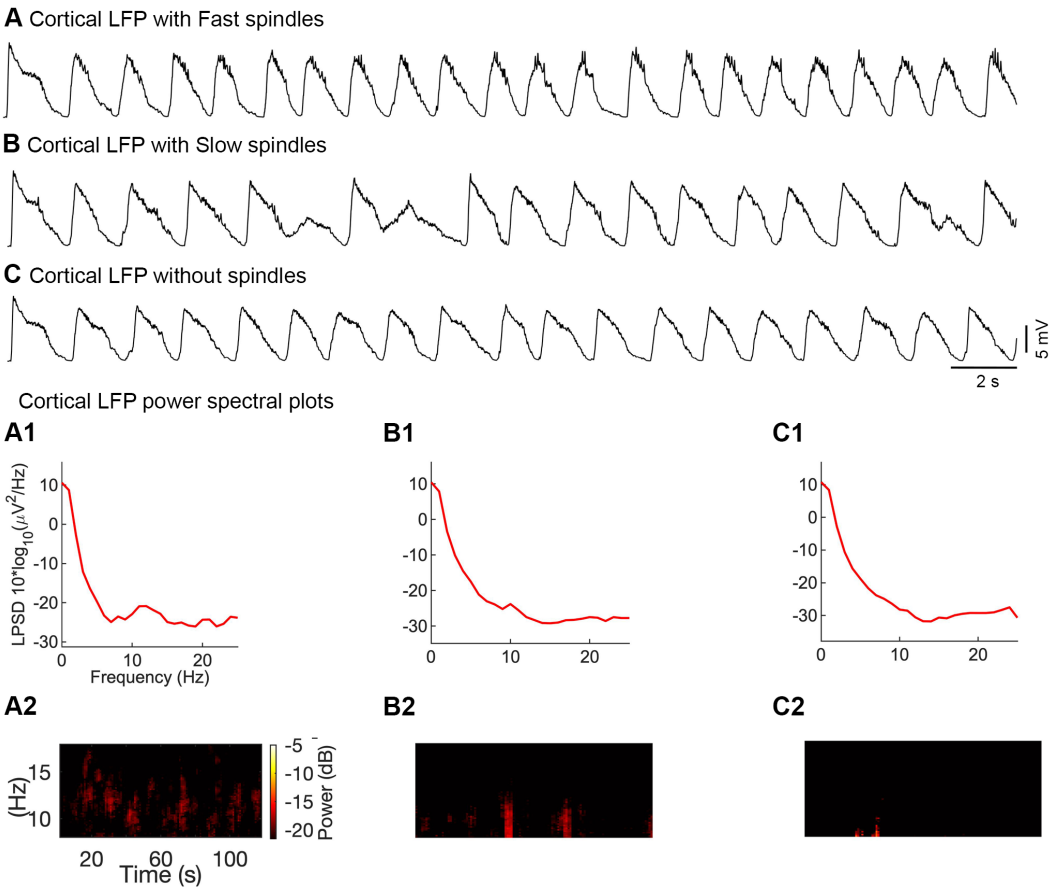


**Figure 4. 4 The influence of different thalamic inputs on the cortical LFP.**

***A***, The cortical LFP coupled with fast thalamic spindles (slow spindles were blocked). Slow thalamic network layers (layers 5 and 6) were blocked by setting synaptic conductance to zero between PY-TC(S) and PY-RE(S) cells. ***A1***, Power spectra of the cortical LFP with fast thalamic spindles ***A2***, The corresponding time-frequency spectrogram of cortical LFP. ***B***, The cortical LFP with slow spindles (fast spindles were blocked). ***B1***, The corresponding power spectra of LFP. ***B2***, The corresponding time-frequency spectrogram of LFP. In the spectrum, the number of slow spindles was relatively low compared to fast spindles (See ***A2***). ***C***, The cortical LFP without fast and slow thalamic inputs. Fast and slow spindles disappeared in both the power (***C1***) and time-frequency (***C2***) spectrum.

For further investigation, mini synaptic currents that initiate SOs, were reduced to observe the role of the slow spindle in SOs initiation. The time period of SO down states was shorter in the presence of slow spindles (see Fig 4.5G-I). The finding that slow spindles may contribute to maintenance of SO activity is the major finding of our model.

Independence of fast and slow spindle networks was investigated in another set of simulations in which network activity was produced after blocking the fast thalamic network (blocking layer 3 and 4), slow thalamic network (blocking layer 5 and 6) or by blocking both thalamic networks (blocking all four thalamic layers). Results

indeed show the temporal properties of fast and slow spindles can be retained independently of one another (Fig. 4.4). The thalamic layers were blocked by setting the synaptic conductance to zero between the cortical PY cells and thalamic cells (PY to TC and PY to RE cells).

### 4.4.3 Properties of SO – spindle interactions

In-vivo fast spindles occur normally during the SO down-to-up transition and SO up state. We refer to this interval as the SO first-half in our model. Correspondingly, the second SO-half (~ 800 ms after the initiation of the SO) characterizes the up-to-down state transition during which slow spindles occur. The fast thalamic subnetwork input projected to the cortical network increases the firing rate of cortical cells (Fig. 4.5A, B). Their spiking occurred earlier as compared to spikes from non-thalamically innervated cortical cells (Fig. 4.5D). Furthermore, the first SO-half associated with fast spindles obtained a larger amplitude (Fig. 4.5E) than without input from the fast spindle thalamic network. The average amplitude of SO cycles coupled with fast spindles was ~8.1 mV, whereas the average amplitude without spindles was ~7.6 mV. Thus, in our model, fast spindles increase both the firing rate of cortical cells and SO amplitude. Slow spindles emerge later, during the second SO-half around ~700 ms after the initiation of the SO cycle, when the SO has already reached its peak amplitude and starts to decline. Omission of the slow spindle thalamic subnetwork (Fig. 4.5C vs. 4.5D) had two effects: a slowing of up state cortical firing rate, and a reduced SO duration. On the other hand, the duration of the second SO-half was more frequently longer in the presence of slow spindles than when only fast spindles were present (Fig. 4.5C vs. 4.5A). Thus, in our model slow spindles appear to essentially assist in initiating the SO. To underpin this finding, we observed the model output across a time span of 120 second. The total time spent in SO down states was only ~16 seconds when slow spindles coupled to the SO up-to-down transition in the cortical LFP whereas without slow spindles a longer total time was spent in the down state, i.e. ~ 32.6 seconds. In this control simulation approximately 10% of SO cycles were initiated by slow spindles (e.g., Fig 4.5I red circled SOs): In cases of SO initiation by slow spindles miniature synaptic currents were not required for the initiation of SO.

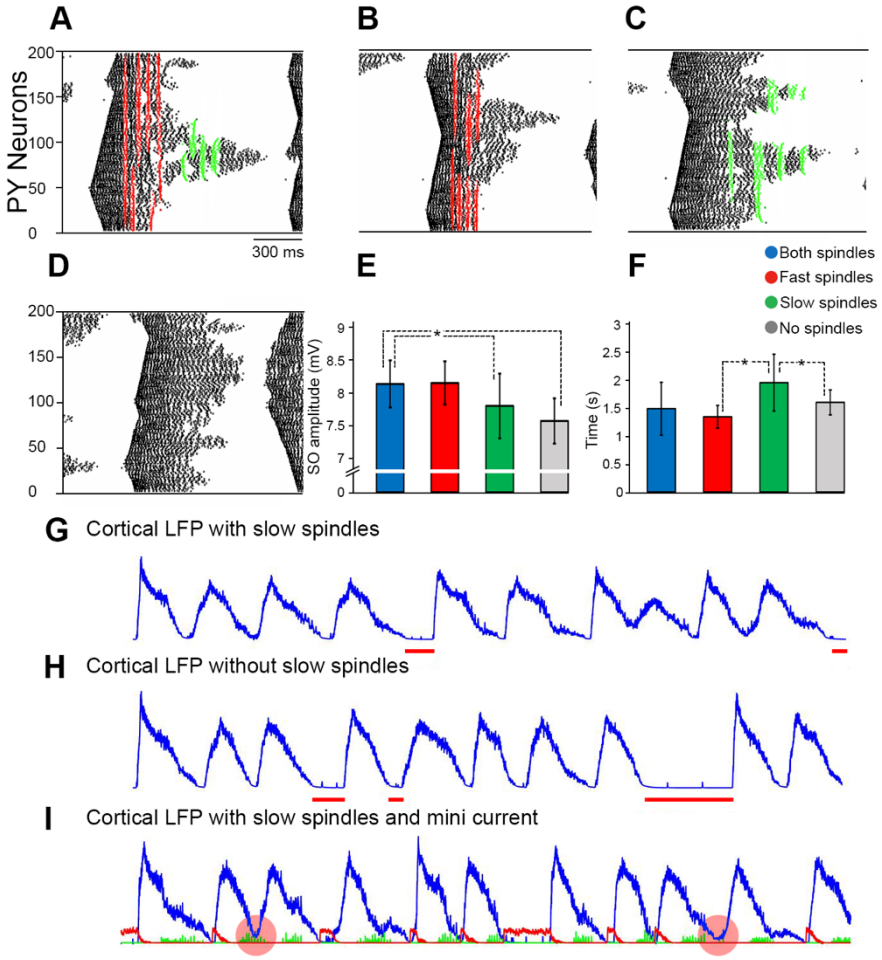


**Figure 4. 5 The influence of different thalamic inputs on the SO cycle dynamics.**

***A,*** PY spike raster plots for one SO cycle with both fast and slow spindles inputs; ***B***, with only fast spindles (slow spindles were blocked). PY firing rate is relatively increased by fast spindle input (red); ***C***, with only slow spindles (fast spindles were blocked). PY firing rate is relatively increase by slow spindle input (green). ***D***, without spindle input (both fast and slow spindles were blocked). ***E***, Average cortical LFP amplitude in the presence of both fast and slow spindles (blue), fast spindles only (red), slow spindles only (green), and without spindles (gray). Average SO amplitude is lowest when spindles are absent. Asterisks show significant difference between the amplitudes (two sample t-test with *P <.01). ***F***, Average SO cycle duration dependent upon presence of spindles. Duration was longest for the presence of slow spindles. Error bars describe standard deviation between SO cycles. Asterisks show significant difference between the SO cycle duration (*P <.01). ***G,*** Resultant cortical LFP when the input of miniature synaptic current was reduced, but slow spindles were still generated by the model. The horizontal red bars indicate periods of increased down state duration due to weak mini synaptic current. ***H,*** Same as for G, however slow spindles are blocked. The down state durations are on average longer than when slow spindles are present (G). ***I***, The cortical LFP with the input of miniature synaptic current (red) and slow spindles (green). The red circles indicate SO initiated by slow spindles without mini current.

In the second-SO-half, the cortical network unit frequency is comprehensively reduced and cortical cells cease firing. To better distinguish between the interaction

of slow and fast spindle subnetworks with SO properties in this critical second SO-half, we replaced slow spindles with the fast spindles (see Fig 4.6), i.e., fast spindles were generated both during the first and second SO-halves (Fig. 4.6B). Fast spindles in the second SO-half eliminated the down/hyperpolarized state of SO, the cortical network remained in its state of increased firing (similar to the first SO-half), albeit exhibited activity was irregular compared to controlled simulation results (Fig. 4.6A). In another control simulation, the model only allowed for generation of fast spindles during the second SO-half. The down states of SOs again disappeared and inconsistent cortical LFPs were observed (not shown in figure). From these results, we conclude that slow spindles maintain a slow oscillation rhythm by preserving the SO down state.

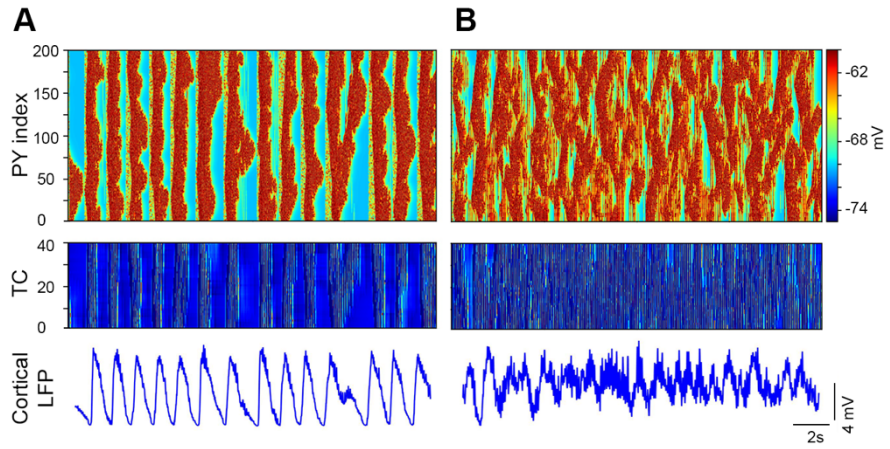


**Figure 4. 6 The influence of fast spindles in the SO cycle.**

***A***, The control simulation in which the fast spindles are coupled with SO-first-half and slow spindles with the SO-second-half. Cortical and network exhibit regular LFP and both the up and down states of Sos are quite clear. ***B***, The simulation in which fast spindles were coupled with both phases of the SO cycle, the first half and the second half. Top panel: PY raster plot revealing that fast spindle coupling in the second phase almost diminished the down/hyperpolarized state of SO. Middle and bottom panels: Fast thalamic activity in both SO halves produced irregular (middle) and more depolarized (bottom) responses.

### 4.4.4 Hyperpolarized fast thalamic subnetwork

The thalamic membrane potential level (in both TC and RE cell layers) differs, physiologically, between depths of NREM sleep and thus plays a role in the likelihood of spindle generation (205), (206). To investigate the response of the model, we increased the hyperpolarization level of fast thalamic subnetwork. Hyperpolarization was increased by altering the conductance of potassium leaked current ($g_{KL}$): $g_{KL}$ = .033 mS/cm$^2$ (from $g_{KL}$ = .03 mS/cm$^2$). The hyperpolarization

response is depicted by raster plots of the all TC cells in the fast (40 TC(f) cells) and slow (40 TC(s) cells) thalamic subnetworks and by the power spectra of the corresponding cortical LFPs (Fig. 4.7): The membrane potential of TC cells of the fast thalamic subnetwork decreased with increased thalamic hyperpolarization compared to control fast thalamic subnetwork activity (Fig. 4.7A-B). In each fast thalamic subnetwork with hyperpolarization a decreased number of spikes per event (~ 6 spikes) were observed relative to control simulations (~ 9 spikes/event; Fig. 4.7D). Fast spindle LFP power also decreased with hyperpolarization (Fig. 4.7 B, left). Interestingly, this increase in hyperpolarization of the fast thalamic subnetwork resulted in a stronger slow thalamic subnetwork input to the cortical network and subsequently, the number of slow thalamic subnetwork events was increased (~25 events per minutes) as compared to the control simulations (~ 19 events per minute: Fig. 4.7 C). The resultant cortical LFP power in the slow frequency range remained the same after hyperpolarization (Fig. 4.7ab right). In summary, the hyperpolarization of the fast thalamic subnetwork reduces fast spindle activity and increases activity within the slow thalamic subnetwork.

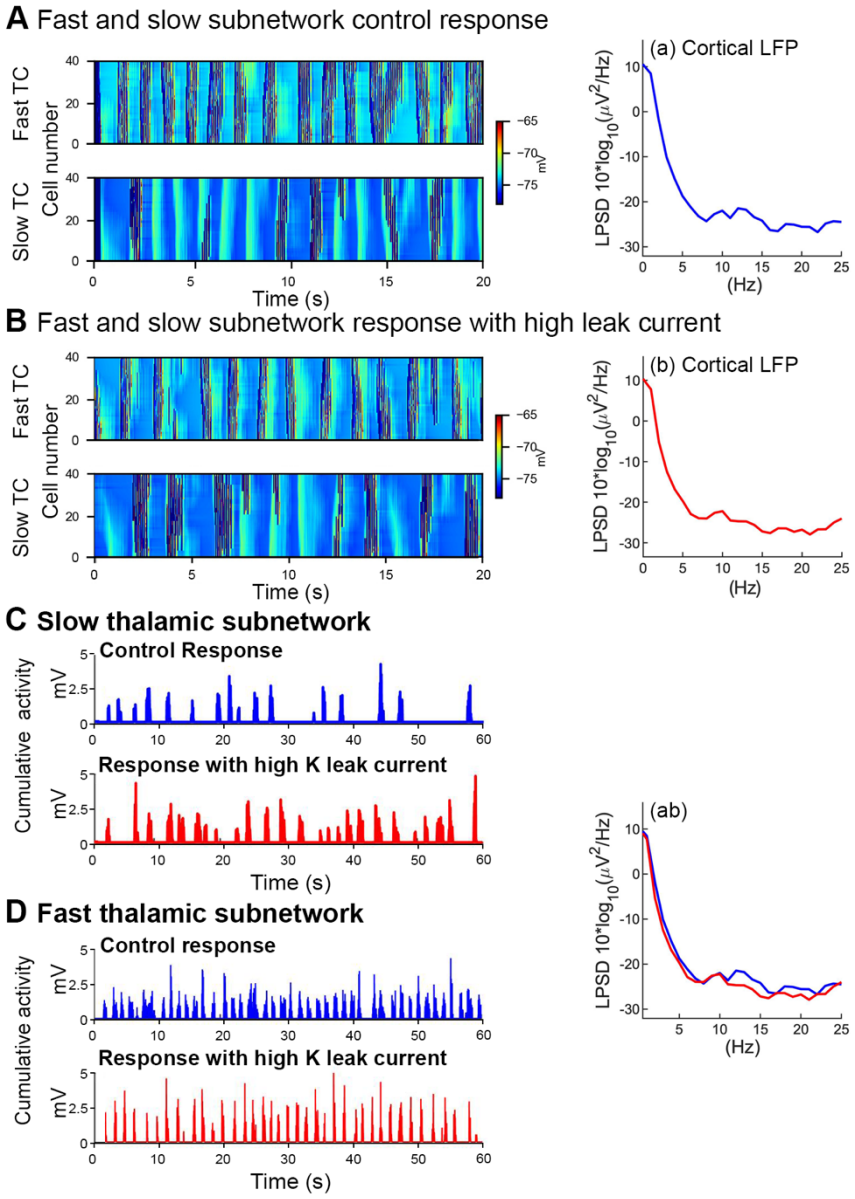


**Figure 4. 7 Influence of increased hyperpolarization.**

Influence of increased hyperpolarization of fast TC and increased potassium leak current in the fast thalamic subnetwork on spindle activity. ***A***, Plots of fast TC and slow TC cell membrane potential (color coded, right axis) overlayed by the firing rate (left axis) during control simulation (left) and the corresponding power spectrum of cortical LFP (right; a). ***B***, Plots of fast TC and slow TC cell membrane potential (color coded, right axis) overlayed by the firing rate (left axis) during hyperpolarization simulation (left) and the corresponding power spectrum of cortical LFP (right; b). ***C***, In control simulations, the input from the slow thalamic subnetwork projecting to the cortical network generated only a few events (~19 events per minute; above panel, left), whereas in simulations with increased K leak current, the number of events was higher (~25 events per minute; bottom panel, left). ***D***, In control results, The fast thalamic subnetwork exhibited stronger response in each event (~ 9 spikes in event; above panel) in control results, whereas in increased K leak these results, the event response was weaker (~ 6 spikes in event; bottom panel). ***ab***, The resultant cortical LFP power in the slow frequency range remained the same after hyperpolarization.

## 4.5 Model validation

Finally, we disintegrated all three subnetworks; cortical, fast thalamic, and slow thalamic subnetworks to validate the main rhythms; SO, fast spindles and slow spindles in each individual network. The cortical network initiation procedure was just like in the integrated model. Both fast and slow thalamic subnetworks were initiated by injecting step current to TC and RE cells. In both thalamic subnetworks, RE cells got .09 nA current whereas TC cells got .065 nA current for 600 ms after every 3 seconds (see Fig. 4.8). All three networks successfully generated expected frequency range. Cortical network generated LFP with little high frequency ~ 1.3 Hz (Fig. 4.8A). Thalamic results were observed in single cell activity. TC cells of the fast thalamic subnetwork fires with frequency of ~ 16 Hz. Moreover, the fast thalamic subnetwork shows weaker response with high potassium leak current (~ 14 Hz) (Fig. 4.8B-C). Similarly, the slow thalamic subnetwork cells fire with frequency ~ 10 Hz (Fig. 4.8D).

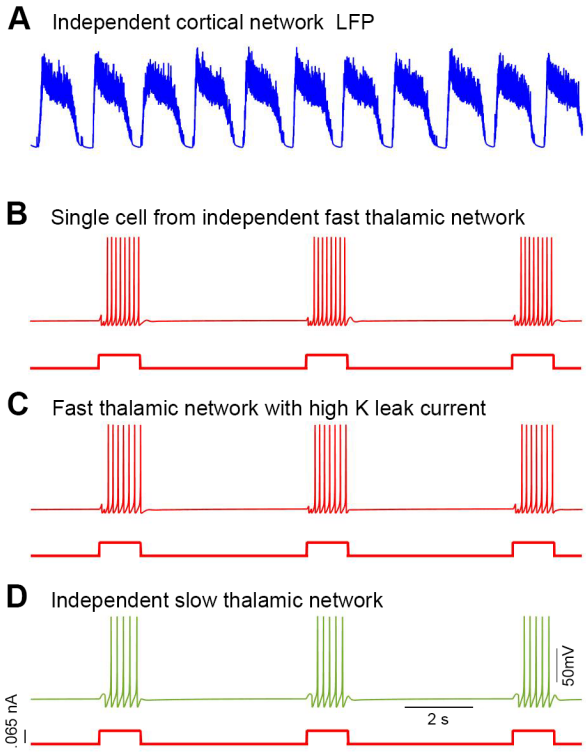


**Figure 4. 8 Each individual network response.**

**A**, The resultant local field potential of the individual (two layered) cortical network. ***B***, Single TC cell exhibits frequency ~16 Hz in individual fast thalamic subnetwork when step current was applied. ***C***, The TC cell of fast thalamic subnetwork with high potassium leak current shows relatively weaker response (~14 Hz). ***D***, The TC cell of slow thalamic subnetwork shows slow frequency ~10Hz.

## 4.6 Results summary

In summary, in our model slow spindle properties can be modeled by a thalamic subnetwork that differs from the fast spindle thalamic subnetwork; Our model revealed the following properties of SO and spindle interactions:

(a) fast spindles increased the SO amplitude;
(b) slow spindles assisted in initiating the SO;
(c) slow spindles regularized and stabilized the SO rhythm by preserving the SO down state; and
(d) hyperpolarization of the fast thalamic subnetwork reduced fast spindle density and increased the number of slow thalamic network events (slow spindles).

Chapter 5

# Closed loop stimulations and sleep spindles

This chapter deals with sleep spindles and closed loop stimulation protocols. Sleep spindles are already introduced and discussed in previous chapter. As discussed earlier, Slow oscillations (SOs) and sleep spindles are two characteristic EEG rhythms of non-rapid eye movement (NREM) sleep. Both rhythms are attributed roles in memory consolidation (113), (185), (207), (208). According to the concept of active system consolidation, cortical SOs provide a temporal window for neuronal reactivation processes during which the transfer of recently acquired memory traces to the cortex for long-term storage is presumed to occur (5), (3), (187). Burst-like waxing and waning EEG sleep spindles are the hallmark of NREM sleep stage N2, but are also found in N3 (209), (18), (48), and are often concurrent with SOs. Like sleep spindles hippocampal sharp wave ripples (SWRs) occur in a phase-dependent manner relative to SOs, and also spindles, (188), (210). The simultaneous occurrence of these and other electrophysiological events reflecting parallel neuronal network activity is indicative of inter-regional communication and cellular plasticity such as long-term potentiation (211), (189), (103), (102), (212). Long-term potentiation like processes were found to specifically occur during sleep spindle-like activity (75). Combined behavioral and EEG studies on human and experimental animals show an association between memory consolidation and spindles activity (spindle density and/or sigma power) in different experimental observations (68), (213), (214), (215). Several experimental studies show that spindle activity can be enhanced through sensory or electrical stimulation during sleep (113), (216), (110), (111). Closed loop acoustic stimulation (CLAS), i.e., acoustic stimulation applied during a specific phase of the SO, presents an intriguing method to study network and behavioral responsiveness in a phase-dependent manner, even across species. CLAS modifies endogenous slow oscillations, sleep spindles, and hippocampal sharp-wave ripples and has been shown to enhance sleep-associated memory consolidation (217). CLAS relies on a specific brain state for stimulation, and timing (i.e., stimulation phase of the oscillatory rhythm) is decisive (112), (218), (219), (220). CLAS is most widely

used as a double stimulation with two stimuli given at the same phase of two successive SOs, the initial study in humans applied closed loop stimulation as a single stimulus. A closed loop driving stimulation (DSt), in which was previously used to optimize the closed loop procedure (110), (111). In humans, CLAS presents a noninvasive tool to potentially improve sleep functions and is more versatile than targeted memory reactivation (TMR) (106).

## 5.1 Study purpose

In this study, we present a thalamocortical computational model for NREM sleep that produces fast spindles along with the SO rhythm (184), (33) and the response of fast sleep spindles to stimulation cues. Several closed loop stimulation protocols are implemented. Stimulation cues are given to the TC layer of the thalamic network as an increase in AMPA currents. The purpose of this study is to develop a computational model which provides a theoretical setup for closed loop acoustic stimulation through which we can improve the activity of sleep spindles by closed loop stimulation protocols during NREM sleep. Our model provides a platform to detect more precise SO states for stimulation cues for both double-click closed loop stimulations (CLS) and driving stimulations (DSt). To better simulate acoustic stimuli, computational current injection targets the thalamic network. Furthermore, this set up provides discrete traces of spindles along with their power.

## 5.2 Thalamocortical model for this study

In this conductance-based thalamocortical model for NREM sleep intrinsic and synaptic currents were computed for all network neurons. The intrinsic currents and their conductances are described in Table A 4.1 and Table B 5.1, and the synaptic currents in Table B 5.2. Our thalamocortical network model consists of two interacting sub-networks (Fig 5.1). The first one is a cortical network for SOs comprised of pyramidal (PY) and interneuron (IN) cells. The second thalamic network generates sleep spindles. The sleep spindles are primarily initiated by the interaction of hyperpolarization current ($I_h$) and the transient calcium current ($I_T$) of thalamocortical/relay (TC) and reticular (RE) cells (45), (43). The thalamic network is also comprised of two cell layers: TC and RE cells. All network neurons are

modeled by Hodgkin-Huxley kinetics. In this model, same intrinsic and synaptic currents are used which are used in previous model (Discussed in chapter 4).

### 5.2.1 Network geometry

The network model is comprised of four one-dimensional layers of neurons (Fig 5.1). Each layer of cells had N neurons, (N = 40) except the PY neurons layer, which had 5N neurons (200 neurons) (203). The first and second cortical layer of PY and IN neurons initiate SOs. The third and fourth are thalamic layers for sleep spindle initiation. The radii of synaptic connections between different layers are described in Table B 5.2 For each SO cycle initiation, EPSPs and IPSPs miniature currents were given to PY-PY, PY-IN and IN-PY cells via AMPA and $GABA_A$ receptors. For Poisson input implementation, NetStim.noise was set to 1 in the NEURON simulator.

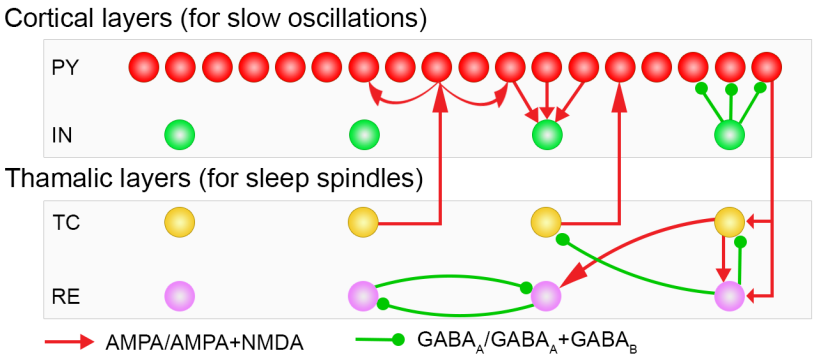


**Figure 5. 1 The thalamocortical network geometry.**

The network is comprised of four cell layers. The top two consist of cortical PY and IN cells. The bottom two, thalamic TC and RE neuron layers, generate sleep spindles. The cortical PY cells layer contains 200 neurons, all other layers contain 40 neurons. Small, green-filled circles symbolize $GABA_A$Rs or $GABA_A$Rs+ $GABA_B$Rs, and corresponding connections. Red arrowheads represent, correspondingly, AMPARs or AMPARs+ NMDARs receptors.

### 5.2.2 Stimulation protocols

Since the intent of this model is to mimic auditory closed loop stimulation, we introduced a sensory neuron (SN), which sends a sensory cue to the thalamocortical (TC) layer of the thalamic network via AMPA receptors. The model also implements a slow oscillation detection algorithm to precisely monitor and detect the different SO states. This algorithm monitors the activity of individual PY cells to help determine SO Down-states. If PY cells are silent for > 100 ms the algorithm starts counting the number of spontaneously occurring PY spikes (action potentials). When

the number of these spikes reaches 75, the algorithm declares this time point as the commencing of the Up-state, i.e., The Down-to-Up- state transition (Fig 5.3C, dark green circle). The stimulation cue is delivered to the TC layer relative to this transitory time period (Fig 5.3). The sensory cue has a duration of 20 ms.

In this study, CLS, sCLS, and DSt protocols were implemented and their effects on sleep spindle activity investigated. In CLS, the stimulation cue was applied at the same phase of two successive SOs (Fig 5.3A, red vertical arrows). After the second of these two cues, the SO detection was paused for 2.5 seconds (Fig 5.3A, grey shaded area) and subsequently resumed, detecting SOs for the next two clicks and so on. The sCLS protocol has the same procedure as CLS, except here, SO detection was paused for 2.5 seconds after applying a single SO stimulation cue.

In the driving stimulation (DSt) protocol, the stimulation cue was applied at every proceeding SO (Fig 5.3B) as long as the silent (Down-state like) period was shorter than 0.5 second (Fig 5.3B time mentioned before the first grey shaded area). If the Down-state like period was longer than 0.5 s SO detection paused for 2.5 seconds (grey shaded area).

## 5.3 Simulation results

In this study, we presented a conductance-based thalamocortical model for NREM sleep and its application to simulate closed loop stimulation protocols. Our NREM sleep model exhibits sleep spindles along with SOs: The main network comprises four layers of cells (Fig 5.1), the top two of which are cortical layers of PY and IN cells for SOs, and the bottom two are thalamic layers of TC and RE cells that initiate the sleep spindles. The TC layer receives information from a SN.

The main thalamocortical network is initiated by applying a mini synaptic current to the cortical layers during the Down state. Once the SO cycle is initiated, the mini synaptic current is removed from the cortical layers. During the SO Down state, the mini synaptic current activates the persistent sodium current of PY neurons and, consequently, these PY neurons depolarize and reach the firing threshold. As one or more PY neurons produces an action potential, they target their neighboring PYs by strong PY-PY excitatory connections and sustain this active/depolarized state for 500-1000 ms because of a strong PY-PY excitation and persistent sodium current. The calcium-dependent potassium current and progressive synaptic depression

terminate this active/depolarized state and bring the cortical network back to the down/silent state (See Fig 5.2A for entire network activity and Fig 5.2B and 2C for single cell activity). One hundred milliseconds after the SO cycle terminates, the mini synaptic current is applied again to initiate the next SO cycle and, similarly, this process is repeated for each SO cycle.

Activation of the cortical network activates, both layers of the thalamic network (TC and RE cells layers). In the thalamic network, the interaction of TC and RE cells produces spindle oscillations with a major contribution of the TC hyperpolarization current ($I_h$) and transient calcium current ($I_T$) (45). The thalamic output is sent back to the cortical network by TC cells. The cortical network receives this thalamic feedback 50-100 ms after the initiation of the SO cycle (Fig. 5.2D blue traces). The cortical local field potential (LFP) was calculated as the sum of the presynaptic currents of PY cells (Fig. 5.2D red traces). In the frequency domain, the thalamic network produced the spindle activity within the frequency range ~10-16 Hz, shown in Fig 5.2E (Time-frequency histogram of Fig 5.2D) and Fig 5.2F (power spectrum density (PSD) of cortical LFP across the 5 minutes time period). In simulation time period of 60 s, an average of 32.6 SOs and 4.6 spindles were observed in the control simulation (Fig 5.2G).

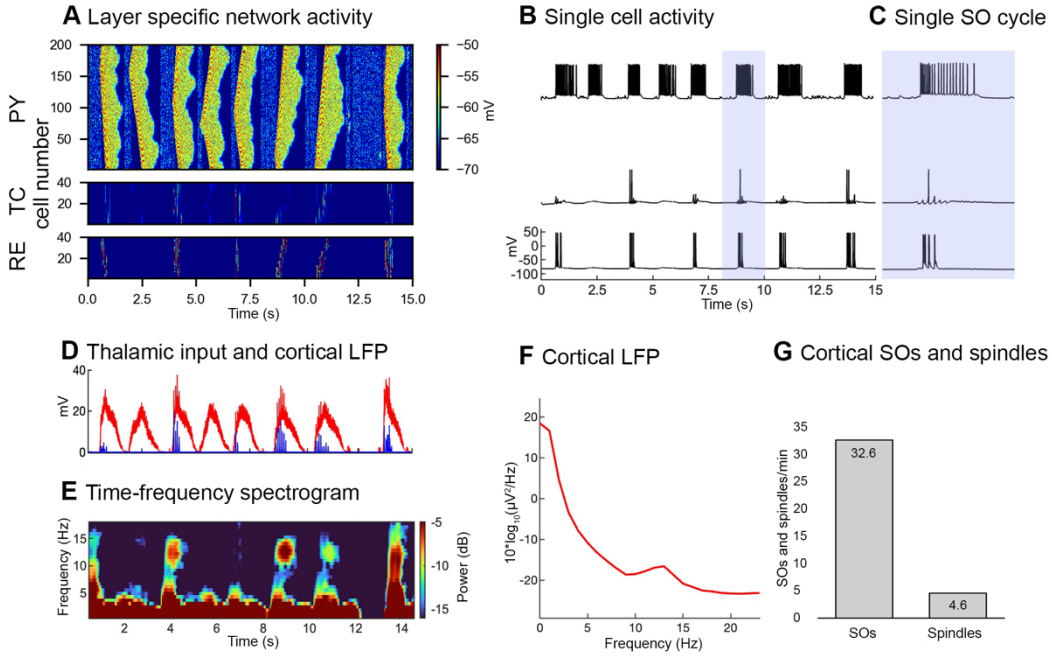


**Figure 5. 2 Layer specific network activity.**

***A***, Time-space raster plots exhibit the simultaneous activity of pyramidal (PY) and thalamic layers (200 PY, 40 cells in each thalamic layer). The membrane potential of each cell is color coded. TC and

RE represent thalamocortical and reticular cells of the thalamic network. ***B***, Corresponding single-cell activity within each neuron layer. ***C***, Zoomed single-cell activity of (blue shaded) one slow oscillation (SO) cycle. ***D***, The cortical LFP (red), calculated as the sum of presynaptic currents (AMPA, $GABA_A$ NMDA) of pyramidal (PY) cells. The thalamic activity (blue) appears at the SO Down to Up-state transition of. ***E***, Time-frequency spectrogram (calculated by short-time moving window Fourier transform) (range, .1–18 Hz) of corresponding cortical LFP of SO and sleep spindle activity. ***F***, Power spectrum density (PSD) of the corresponding cortical LFP, exhibiting a peak in the sleep spindle (10–16 Hz) frequency band. ***G***, The average number of SOs and spindles per minute.

### 5.3.1 Results with Stimulation protocols

We implemented two stimulation protocols; "double" click closed loop stimulation (CLS) and driving stimulation (DSt) protocols (Fig 5. 3) which targeted the TC layer of the thalamic network (for details, see *stimulation protocols* section in methods). To define different states of SOs, the SO is topographically divided into four states (Fig 5.3C), and its corresponding phase angles are also derived from the Hilbert transformation of filtered LFP (Fig 5.3D). The first phase is the Down state (its corresponding phase angle is 180°) when the entire cortical network goes into a silent state. The second state is the Down to Up-state transition (D2U state transition, phase angle between 180°-360°) commencing when the cortical network starts depolarizing (Fig 5.3C, green bar). The third is the Up state (360°) when the amplitude of cortical LFP reaches its peak, and the last state is the SO Up to Down-state transition (U2D state transition, phase angle between 0°-180°) when the amplitude of cortical LFP starts dropping (Fig 5.3C, red bar) back to a Down state. In the present study, stimulation cues were topographically applied on different states of SOs, but here in the results, four of them were discussed in detail and shown in Fig 5.3C (small colored circles). The first stimulation point was at the commencing of the D2U state, Fig 5.3C, dark green circle) the term "Point 1" was used for this stimulation point. Similarly, for the next two points, when stimulation cues were applied with a time delay of 120 ms and 180 ms (Fig 5.3C, light green circles) after the commencing of the D2U state, the terms "Point 2" and "Point 3" were used respectively. For the last stimulation point when stimulation cues were applied during the transition from the Up to Down-state (Fig 5.3C, red circle), the term "Point 4" was used.

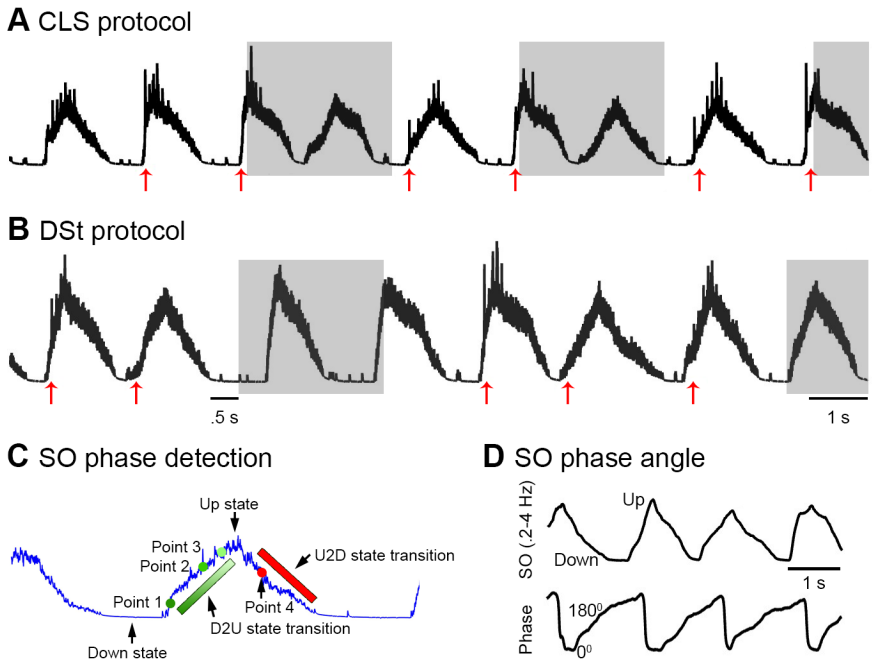


**Figure 5. 3 CLS and DSt protocols.**

***A***, In this CLS protocol, the stimulation cues (red arrows) were applied at the commencing of the SO Down to Up-state transition of two successive SOs. After these two cues, SO detection was paused for 2.5 seconds (grey-shaded). ***B,*** In the driving stimulation (DSt) protocol, the stimulation cues were delivered to the transition of the SO Down to Up-state for as long as the duration of Down state was below 0.5 seconds. ***C,*** Different states of SO and stimulation points. The dark green circle is the stimulation point at the commencing of the D2U state transition called "Point 1", the light green circles present the stimulation points with 120 ms and 180 ms time delay from the SO detection point (dark green), called "Point 2" and "Point 3" respectively. The red bar presents the SO Up to Down-state transition and the red circle is the stimulation point during the U2D state transition called "Point 4". The black arrows point to different states of SO and stimulation points. ***D***, Filtered SOs and their corresponding calculated phases.

### 5.3.2 Results of CLS simulations

In CLS simulation (Fig 5.3A) spindle power was adequately increased when stimulation cues were applied at the "Point 1". Conversely, CLS was not effective when cues were applied at the "Point 4". The power spectral density (PSD) of the cortical LFP revealed a strong increase in the sigma band (10-16 Hz) when stimulation cues were applied at "Point 1" compared to "Point 4" stimulation and control simulations (Fig 5.4A). In addition, the sigma band at "Point 4" stimulations was even slightly reduced compared to the control PSD. Similarly, at "Point 1" stimulations, the density of spindles was higher (average of 8 spindles per minute) than in the control and "Point 4" stimulation (4.6 and 4 spindles per minute respectively) (Fig 5.4B). In addition, the spindle density was also high when the cue

was applied at "Point 2" and "Point 3" (Fig 5.3 C). However, spindle activity decreased at longer delays (Fig 5.4C). Moreover, the corresponding PSDs of the "Point 2" and "Point 3" were also higher than the control PSD (not shown in the figure). At "Point 1" stimulation, the inter-spindle time period was significantly decreased because of more spindle events, and the spindle events occurred in around regular time intervals (7.3 s, standard deviation; 2.7 s). Conversely, in "Point 4", spindle events occurred in irregular, large time intervals (14 s, standard deviation; 9.4 s). In another set of simulations, CLS was applied at "Point 1" with different pause times (2 s, 3 s, and 4 s) between pairs of clicks (see pause time in Fig 5.3A). In the resultant PSDs of cortical LFP, the sigma band was adequately weaker when the pause time was set to 3 s and 4 s, but the results with 2 s and 2.5 s pauses were approximately the same. In summary, the CLS was more effective for spindle power and density when the cue was applied at the commencing of D2U state transition (Point 1), but increased stimulation delay (from "Point 1") decreased the effect of stimulation cues. Conversely, the CLS wasn't effective when the stimulation cue was applied during U2D state transition (Point 4).

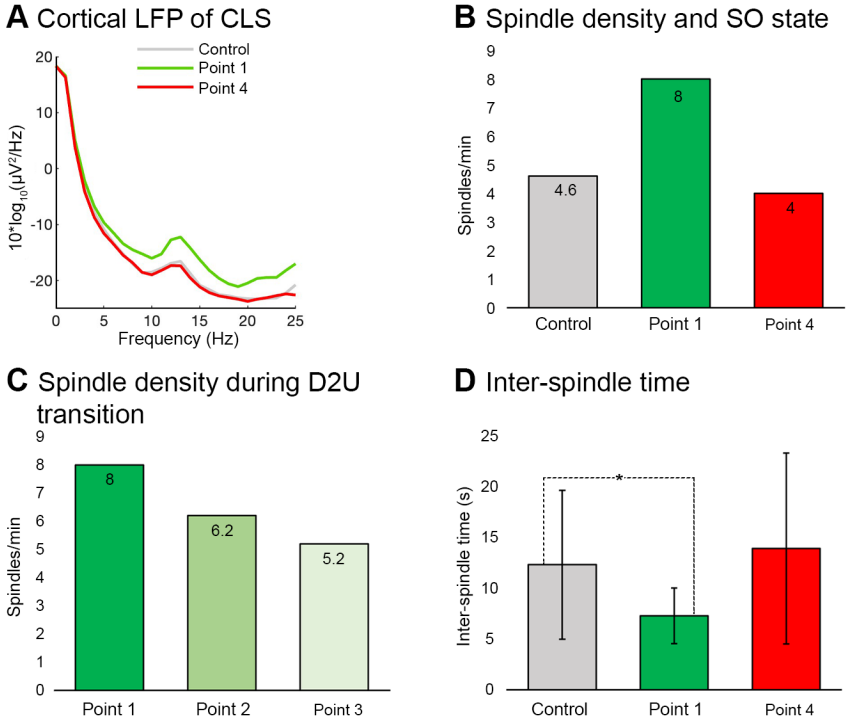


**Figure 5. 4 Closed loop stimulation (CLS) simulation results.**

***A,*** Power spectral density (PSD) of the cortical LFP across a 300 s time period with "Point 1" (green), "Point 4" stimulation (red), and control (grey) simulation. Spindle power was increased compared to Control when the stimulation cue was applied at "Point 1". Conversely, spindle power was not

increased when the cue was applied at "Point 4". ***B,*** Number of spindles in resultant simulations. Mean value of spindle density was increased during "Point 1" (green) compared to "Point 4" stimulation (red) and control simulation (grey). ***C,*** Mean value of spindle density was decreased when the stimulation cue was applied at both delays after the "Point 1" point. The stimulation cue was less effective with a larger time delay (180 ms) compared to a smaller time delay (120 ms). ***D,*** Average inter-spindle time. The average inter-spindle time period was also significantly reduced when stimulation cues were applied at "Point 1" compared to "Point 4" (red) and control simulation (grey). * $P < .005$, two sample t-test.

### 5.3.3 Results of DSt simulations

In the driving stimulation (DSt) protocol (Fig 5.3B), the stimulation cue was applied on every successive SO until its post Down state time period was less than 0.5 s. As the time period of the Down state exceeded 0.5 s, stimulation was paused for 2.5 s (see Fig 5.3B). In the DSt simulation results, the spindle power was also adequately higher in "Point 1" stimulation. In the resultant PSD of cortical LFP, the sigma band activity was higher than the "Point 4" and control simulations (Fig 5.5A). Similarly, in "Point 1", the spindle density was also higher (Average 8.2 spindles per minute) than in "Point 4" control simulation (4.6 and 3.4 spindles per minute respectively) (Fig 5.5B). Even in "Point 4", the average number of spindles was less than the average number of spindles in control simulations. In addition, the spindle density was also high when the cue was applied on "Point 2" and "Point 3" but the spindle density was decreased with an increased delay (not shown in figure) like CLS simulation results. At "Point 1", the inter-spindle time period was sufficiently decreased, and the spindle events occurred in regular time intervals (7 s, standard deviation; 2.9 s). Conversely, at "Point 4", spindle events occurred at irregular and large time intervals (17 s, standard deviation; 9.5 s). Moreover, in DSt (during "Point 1") the number of clicks (Fig 5.4D) was less than CLS in 5 minutes of simulation time (73 clicks and 115 clicks respectively). Compared to CLS and DSt results, the spindle densities were approximately the same in both protocols during "Point 1", "Point 2", and "Point 3" stimulations. On the other hand, the in PSD of CLS during "Point 1", the sigma band was slightly higher than the corresponding PSD of DSt.

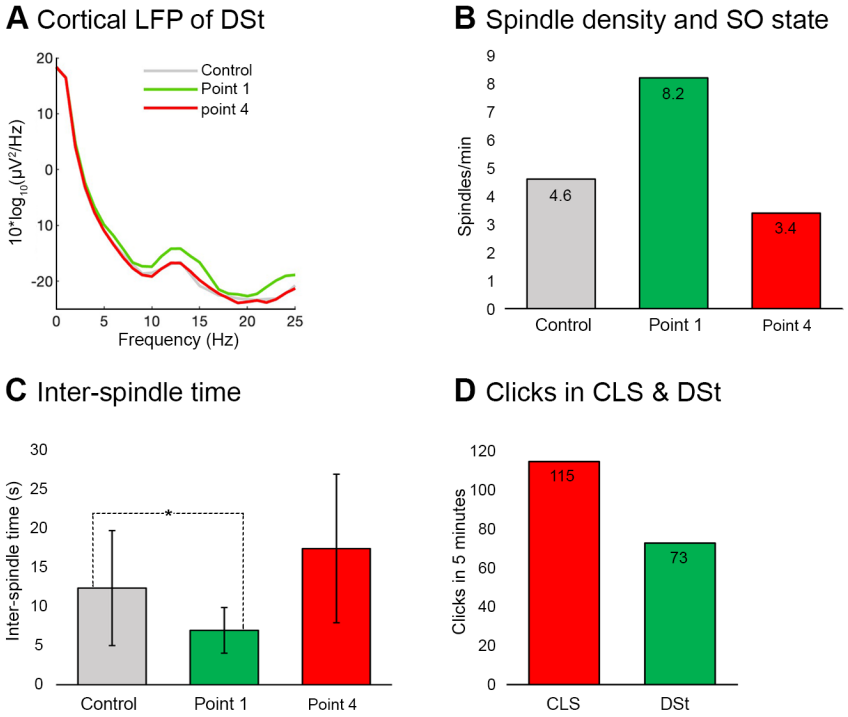


**Figure 5. 5 Driving stimulation (DSt) simulation results.**

***A,*** PSD of the cortical LFP across a 300 s time period with "Point 1" (green), "Point 4" stimulation (red), and control simulation (grey). Spindle power was increased compared to Control when the stimulation cue was applied at "Point 1". Conversely, this power was not increased when the cue was applied at "Point 4". ***B,*** Number of spindles in resultant simulations. Mean value of spindle density was increased when the stimulation cue was applied at "Point 1" (green) compared to "Point 4" stimulation (red) and control simulation (grey). ***C,*** The average inter-spindle time period was also significantly reduced when stimulation cue was applied at "Point 1" compared to "Point 4" stimulation (red) and control simulation (grey). * $P < .005$, two sample t-test with. ***D,*** Number of clicks (cues) in CLS and DSt simulations across the time period of 300 s. The number of clicks was significantly higher in CLS compared to the DSt simulation.

### 5.3.4 Results of sCLS simulations

In another set of simulations, one click closed loop stimulation (sCLS) was applied to the TC model. In this stimulation protocol, the stimulation was paused for 2.5 s after each click. In sCLS at "Point 1", the spindle power was also higher than control simulations (Fig 5.6A); particularly, the spindle density was significantly higher (Fig 5.6B) than the sigma band of corresponding PSD. The sCLS wasn't very effective with a delayed cue; particularly on "Point 3", the results couldn't show a notable change in the sigma band of the corresponding PSD and control PSD. Moreover, on the optimal simulation point ("Point 1") the sigma band of sCLS LFP was weaker than the corresponding CLS sigma band (Fig 5.6C). In conclusion, sCLS was

effective when the cue was applied at "Point 1". The delayed cue (particularly on "Point 3") wasn't as effective as in CLS and DSt.

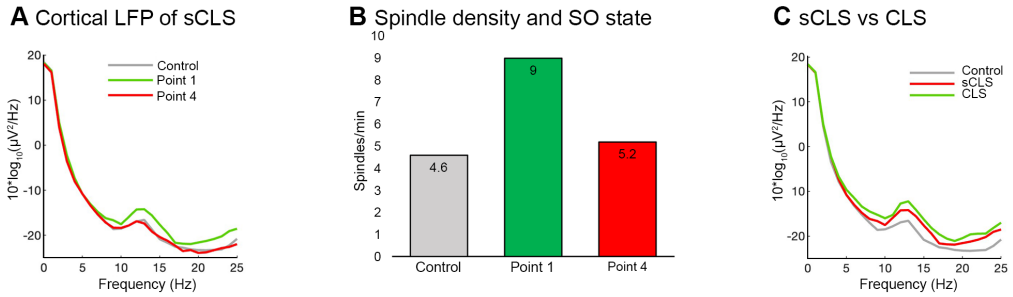


**Figure 5. 6 One click Closed loop stimulation (sCLS) simulation results.**

***A,*** PSD of the cortical LFP across a 300 s time period with "Point 1" (green), "Point 4" stimulation (red), and control simulation (grey). Spindle power was increased compared to Control when stimulation cues were applied at "Point 1" like CLS and DSt. ***B,*** Mean value of spindle density in Control, "Point 1", and "Point 4" stimulation. ***C,*** PSDs of cortical LFP with control simulation, sCLS, and CLS stimulation at "Point 1" stimulation. The sigma power was higher in CLS than in sCLS.

## 5.4 Initiation of slow spindles: Possible mechanism

In our model, we observed that the shift of cortico-thalamic potential from the TC layer to the RE layer exhibited an important role in the frequency of spindles and their topographical occurrence on SOs. In normal simulation results, the TC layer received a stronger input (by increased synaptic conductance, PY-TC; .003 μS) than the RE layer (PY-RE; .0015 μS) from the cortical network (Fig 5.7A). As a result of this higher cortical input, the TC layer interacted with the RE layer instantly and initiated spindles rhythms which nested to cortical LFP during the transition from an SO Down to Up-state (Fig 5.7A, 5.7A1). The corresponding single-cell activities of both thalamic layers also simultaneously emerged during the time period of the SO Down to Up-state (Fig 5.7A2).

In another set of simulations, the cortico-thalamic potential was altered in both thalamic layers and conversely, the RE layer received a stronger cortical input (PY-RE; .0021 μS) than the TC layer (PY-TC; .001 μS). In response to the stronger cortical input, the RE layer produced stronger activity and sent strong inhibitory feedback to the TC layer (Fig 5.7B). This inhibitory feedback actually hyperpolarized and suppressed the activity of the TC layer during the SO Down to Up-state transition. Moreover, this inhibitory feedback was gradually decreased and after approximately ~400 ms (Fig 5.7B1), the TC layer (received reduced RE feedback became depolarized) interacted with the RE layer and produced slow

spindle activity (Fig 5.7B3) which was nested with SO during the SO Up to Down-state transition. In the corresponding single-cell activity of both thalamic layers, the RE cell presented very strong activity during an D2U state time and, meanwhile, the activity of the TC cell was completely or partially suppressed. In a later part (U2D state) when RE activity became a bit weaker, the TC cells became depolarized and interacted with RE cells (Fig 5.7B2) and produced slow spindles. In conclusion, strong inhibitory feedback of the RE layer to the TC layer shifted the spindle activity in the U2D state and the frequency of spindles was also decreased (8-11 Hz) by this inhibition.

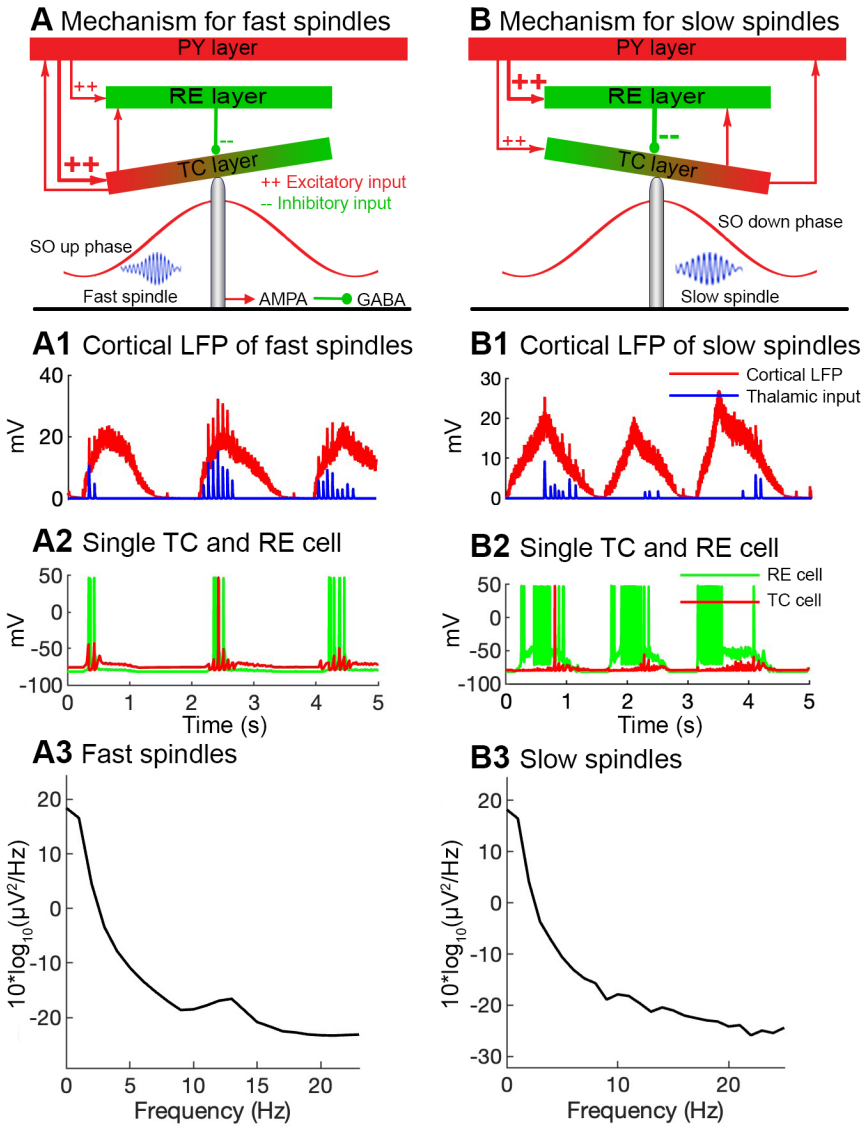


**Figure 5. 7 Possible mechanism of the initiation of fast and slow spindles.**

***A,*** A cartoon diagram of fast spindles' mechanism. The thalamocortical (TC) layer receives a stronger cortical excitatory input (large red plus sign) from the pyramidal layer, whereas the reticular (RE) layer receives a weaker cortical input. Having a relatively strong excitatory input, the TC layer produces fast thalamic activity which is nested with SOs during the D2U state transition (left bottom). ***A1,*** The cortical LFP (red) with fast thalamic input (blue) which is nested with cortical LFP during the D2U state transition. ***A2,*** The corresponding activity of single TC (red) and RE (green) cells. ***A3,*** PSD of cortical LFP with fast spindles. ***B,*** A cartoon diagram of slow spindles' mechanism. The RE layer receives a stronger cortical excitatory input (large red plus sign) from the pyramidal layer whereas the TC layer receives a weaker cortical input. Having an excitatory input, the RE layer sends a strong inhibitory input to the TC layer and resultantly, the TC layer produces slow thalamic activity during the U2D state transition (left bottom). ***B1,*** The cortical LFP (red) with a slow thalamic input (blue) which is nested with cortical LFP during the U2D state transition. ***B2,*** The corresponding activity of single TC (red) and RE (green) cells. The TC cell activity is observed later (~400 ms) during the SO Up to Down-state ***B3,*** PSD of cortical LFP with slow spindles.

## 5.5 Results summary

In summary, our model showed the possible ways to improve the activity of sleep spindles via CLS and DSt protocols and also the role of strong RE activity in SO phase shifting of slow spindles. Our model revealed the following effects of stimulation protocols on sleep spindles and the role of strong RE-TC activity:

1. Spindle power and density were increased when stimulation cues were applied at the commencement of the SO D2U state transition ("Point 1").
2. The effect of stimulation was decreased when cues were applied with increased delay from the "Point 1".
3. Spindle power and density were not improved when cues were applied during the U2D state transition.
4. The sigma power of CLS was significantly stronger than DSt and sCLS during "Point 1" stimulation.
5. A strong inhibitory input of the RE layer to the TC layer shifts the spindle activity to U2D state transition (from D2U state).

Chapter 6

# Discussion and summary

## First study

In our first study, we demonstrated the modulatory effects of calcium influx and gap junction activation during the expression of sharp-wave ripples in CA1. In our computational model we showed that the expression of SPW-Rs was a calcium dependent process. The number of SPW-Rs decreases with a reduction of calcium influx through pyramidal cells. Interestingly, similar results are obtained when the current is reduced through gap junctions. In another set of simulations, we demonstrated that a reduction in calcium influx and a decreased conductance through gap junctions had synergistic effects on the generation of SPW-Rs in our computational model of CA1.

Neurotransmitters like acetylcholine, norepinephrine, serotonin etc. suppress SPW-Rs in experimental animals (93), (95), (97). These neuromodulators are thought to reduce the calcium influx through presynaptic terminals in Schaffer collaterals (95), (61). This reduction in calcium influx in turn decreases the glutamate release in the synaptic cleft resulting in a decreased firing rate of neurons and eventually affects the network's fast oscillations. Reduction in calcium influx into the PCs of CA3 and CA1 weakens the contact among neighboring cells by recurrent axonal collaterals (60). This leads to less synchrony of postsynaptic cells and a suppression of SPW-Rs in CA3 and CA1.

In our model, we gradually reduced the calcium influx through axonal collaterals and dendrites assuming that this decline in calcium influx partially mimics the decrease in presynaptic calcium mediated by various neuromodulators in experimental settings. The decrease in calcium conductance weakens the strength of the synapses of the pyramidal cells. These weak synapses don't provide enough strength to targeted cells to fire in the network. Similarly, with low calcium conductance targeted cells depolarize slowly, which causes a delay in *SPW-Rs* generation. Furthermore, SPW-Rs disappeared when calcium influx was completely blocked in

pyramidal cells in both models of ten cells (data not shown) and 26 cells except for the first sharp wave, which occurs during network stimulation time.

In our computational model we observed that SPW-Rs were also suppressed by reducing the conductance through gap junctions. Moreover, reducing both calcium influx and gap junction coupling had a synergistic effect on the suppression of SPW-Rs. As previously described, excitatory synaptic interaction and electrical signaling through gap junctions coordinate ripple activities (175), (89). Thus, these ripples are inhibited by blocking gap junctions (60), (61). Interestingly, monoamines like norepinephrine, serotonin and dopamine reduce the gap junction coupling mainly by two different signaling mechanisms, i.e. through the IP3/$Ca^{2+}$/ protein kinase C pathway and the adenylyl cyclase/cAMP/protein kinase A pathway (221), (222), (223). In addition, cholinergic input also reduces gap junction coupling (224). In a recent publication from Buzsaki's lab, Fernández-Ruiz and colleagues showed that SPW-Rs were prolonged during learning processes, and these prolonged ripples recruit new neurons (225). This finding opens a new window for a modulation of the temporal structure of SPW-Rs and its implication for learning, both experimentally and theoretically.

**Second Study**

Sleep spindles are the other prominent EEG rhythm of NREM sleep. These are initiated by the interaction of thalamocortical (TC) and reticular (RE) cells of thalamic nuclei (45). These spindles are also sent to the cortical network by collaterals of TC cells. Generally, these are nested with cortical SOs at the initial phase of the SO cycle, the first-half phase in primates and rodents. In human sleep studies, spindles are classified into two categories, namely fast (12-16 Hz) and slow (8-12 Hz) spindles. The fast spindles are mostly found in central and parietal cortical regions, and these are also nested with SOs during the first-half of up state. Slow spindles are observed in the frontal cortical area, and these are nested with SO during the second-half of up state, (18), (48). Fast spindles are extensively studied in the experimental and computational arena regarding their role in long-term potentiation and synaptic plasticity (189). Conversely, slow spindles need lot of work to find clear answers about their origin, cellular mechanism, and most importantly their role in such a framework (SO, fast spindles, hippocampal ripples) that is dedicated for

memory consolidation. As a step ahead, it would be useful to explore the functional relation between SOs and slow spindles.

In this study, we developed a thalamocortical model for SOs, fast and slow sleep spindles. The novel aspect is the inclusion of thalamic-based slow spindle generation. Two independent sub-thalamic networks were developed for each fast and slow spindles. Physiologically fast and slow spindles occur at the SO down-to-up transition / SO up-phase and at the SO up-to-down transition, respectively. In the model fast spindles are nested with SOs during the first-half of the SOs cycle (SO down-to-up transition / SO up-phase) and the slow spindles are nested with SOs during the second SO-half (end of the SO up state/up-to-down transition). Slow spindles are produced with the same intrinsic and synaptic current dynamics as fast spindles but the thalamic subnetwork is in a more hyperpolarized state. According to our model results, slow spindles can initiate SOs and may thereby facilitate the maintenance of ongoing SOs. A contribution of slow spindles to the maintenance of activity in the SO state could also be deduced from the decrease in SO duration on omission of slow spindles. Faster electrophysiological activity ensues as NREM sleep lightens.

Fast spindles could not replicate these actions of slow spindles on the SO. When simulations were run for fast spindles nesting within the second SO-half (end of the up-state), the cortical network exhibited an irregular LFP pattern and the down states of SOs practically disappeared. Moreover, the fast thalamic subnetwork response was reduced when the hyperpolarization level in this network was increased, in contrast to the facilitatory response of the slow thalamic subnetwork to hyperpolarization. Thus, our model shows that slow spindles can facilitate cortical network activity while maintaining the natural rhythm of SOs.

To which neurophysiological processes are the model properties consistent? Prominent initial studies revealed that SO arise from layer 5 pyramidal cells and that SOs continue despite thalamic deafferentiation (32) e.g. through intrinsic activity emerging in layer 5 pyramidal cells. (31), (32), (226). It was recognized that thalamic input can contribute to cortical Up-states (227), however, the argument that SOs do not require thalamic input for initiation contrasts more recent studies that disclosed thalamic activity preceding the onset of cortical Up states, and also that severing thalamocortical connections reduced the incidence of spontaneous cortical Up states

(228), and also modified ongoing SO frequency (229). Experiments on anaesthetized cats demonstrated that thalamic oscillations contribute importantly to the cortical network in generating SOs and can results explain previous contradictory findings (230), reviewed in (67). Thalamic output at the time of slow spindle activity may thus deliver the input to the cortex required for triggering cortical Up states. Some thalamocortical cells, including the ventral lateral posterior (VLp) nucleus as a possible thalamic source of slow frequency spindles (194), possess both core-like and matrix neurons, and project thus to both superficial and deeper cortical layers, including axonal arborizations to layer V (231), (232), (233). The intrinsic initiation of SOs in cortical layer 5 is discussed in the context of one the of two possible mechanisms, firstly, by persistently active pacemaker-like cortical cells, and secondly by temporal summation of spontaneous synaptic activity (226), (67). Any one of both mechanisms cannot initiate the SOs unless it counters the activity-dependent $K^+$ conductances that are activated during active states. Consistent with our modeling results slow spindle could assist in SO initiation by providing some depolarization to counter activity-dependent hyperpolarization conductances. Independent on whether such bilayer cortical input could be beneficial for SO initiation in layer 5 pyramidal cells, the above cytoarchitectonics and neurophysiological processes may allow to explain model results on slow spindle-SO initiation.

Processes underlying the maintenance of the SO rhythm are undoubtedly even more diverse and complex than can be reflected in our model. Human intracranial recordings and rodent local field potentials describe mechanisms on how thalamic spindles may drive cortical spindles emerging during the SO down-to-up transition (234), (235). Slow and fast spindles are found however to occur during the same SO phase (234), thus findings on the temporal relationship between thalamic and cortical down states are not comparable with our modeling results. These inconsistencies in slow spindle timing present a major focus of ongoing research (236), (237), (238).

Modeling results presented two properties regarding the impact of fast spindle on the slow spindle network. Firstly, that fast spindles increased the firing rate of cortical cells and SO amplitude, and secondly that the hyperpolarization of the fast thalamic network reduced fast spindle, yet increased slow spindle activity. Both properties are associated with membrane potential level of thalamic cells and coincide with results

linking increased thalamic hyperpolarization to the emergence of delta oscillations and increased NREM sleep depth. (239). In deeper NREM sleep occurrence and frequency of spindles are also reduced in humans (193).

Taken together, our modeling results present above most a further platform to test the potential role to thalamic spindles in SO initiation. In future work, we will extend this study by making structural and physiological modifications for more detailed experiments. For instance, by including neuronal plasticity in the current model we could analzye the potential contribution of slow spindles to this function.

**Third study**

In this study, we developed a thalamocortical model for SOs and fast sleep spindles. The SOs are initiated in two layered (PY and IN layers) cortical networks and sleep spindles are initiated by the interaction of two layers (TC and RE Layers) of the thalamic network. Physiologically, fast and slow spindles occur at the D2U state transition and at the U2D state transition, respectively. In the model, fast spindles are nested with SOs during the first half of the SOs cycle (D2U state transition). In addition, the stimulation protocols were implemented on the thalamic network. The TC layer received a stimulation cue via AMPA receptors. Two types of stimulation protocols were implemented in the model: CLS and DSt (for details, see *Stimulation protocols* section in Methods).

According to our model results, in both CLS and DSt, an increased spindle activity was observed when stimulation cues were applied at the commencing of the D2U state transition (Point 1). In addition, the spindle activity gradually decreased when stimulation cues were applied with a time delay from the commencing of the D2U state transition. On the other hand, the cues didn't have a significant effect during the U2D state transition (Point 4). The sigma power of CLS results was comparatively higher than DSt results when stimulation cues were applied at "Point 1", but the spindle density was almost the same in both results. Finally, in another set of simulations, we observed that the slow spindles can be produced by the same thalamic network by the shift of cortico-thalamic potential from the TC layer to the RE layer. A strong inhibitory input of the RE layer to the TC layer shifted the spindle activity to the U2D state transition (from the D2U state transition) and the frequency of spindles was also reduced (8-11 Hz) by this inhibition.

During slow wave sleep, both cortical and thalamic networks display phase-related synchronous activity in a narrow time window (240). The sleep spindles and SOs emerge approximately in the same temporal window. Actually, as the cortical network initiates a SO, it also sends feedback to the thalamic network at the same time and ultimately, the thalamic network initiates fast spindles, which are observed a few milliseconds after the initiation of a SO (33).

When a cortical network initiates a SO, the PY cells start depolarizing and generate action potentials. At the start of the D2U state transition, the PY cells exhibit a very strong depolarization, and resultantly the cortical LFP rise with a steep slope. Meanwhile, the thalamic network also receives a stronger synaptic input via corticothalamic projections, and this strong cortical input eventually initiates spindles. Furthermore, the resultant thalamic feedback to the cortical network also supports the role of a strong corticothalamic input because the fast spindles are also found quite soon after the commencing of the D2U state transition. Our model results suggest that, at the commencing of the D2U state transition, the strong corticothalamic input and concurrent stimulation cue synergistically increase the spindle activity. On the other hand, the stimulation cues were less effective when the thalamic network received weaker corticothalamic inputs.

González-Rueda et al. (241) conducted an in vivo experimental study on mice. They conducted in vivo single-cell recordings, and optogenetic stimulation of presynaptic inputs in the murine cortex. The results showed that conventional spike timing-dependent plasticity was observed during Down-states of SWS activity. On the other hand, Up-states are linked to a decrease in EPSPs slopes. Presynaptic stimulation that results in postsynaptic spikes would protect (but not enhance) the corresponding connections during the SO Up-states of SWS activity. The stimulation protocols of González-Rueda study and our model are nearly similar to each other because in both studies the stimulation cues were applied on a cellular level. Interestingly, in both studies, the stimulation cues were effective approximately in the SO Down-state. Moreover, another computational study (204) also observed that, when stimulation cues were applied to the cortical network during the SO Down-state, positive effects were observed on synaptic plasticity. On the other hand, some experimental studies suggested that cues were effective during the SO Up-state (110), (111). There can be different reasons for this SO state discrepancy. The foremost reason could be the

delay from the cue sound to the brain. The other possible reason can be the difference in state detection methods in both groups of studies. We detected the SO state on the basis of cellular activity whereas Ngo et al. (110), (111) used EEG traces for SO state detection.

In our previous study (184) we presented a thalamocortical model for both fast and slow spindles along with SOs. In that study, we proposed that the slow spindles are possibly initiated in a more hyperpolarized thalamic sub-network, and for their emergence during the second-half SO Up-state, we suggested the synaptic delay of 600 ms time between PY-TC connections. Then we couldn't find experimental evidence for the 600 ms synaptic delay because of an insufficient number of human studies. In this study, we found an interesting observation about phase shifting without adding a synaptic delay between PY-TC cells. During the first SO phase, a strong RE to TC negative feedback actually hyperpolarized and suppressed the activity of the TC layer. This inhibitory feedback was gradually decreased and after approximately ~400 ms (Fig 5.7B1), the TC layer became depolarized and interacted with the RE layer and produces slow spindle activity (Fig 5.7B3) during the second SO phase/U2D state transition.

Functionally, sleep spindles are considered very important for sleep quality (242), (243) neuronal development (244), (245) and synaptic plasticity and memory consolidation. The bursting property of sleep spindles sends a strong synaptic input which eventually triggers synaptic plasticity (246). This repetitive discrete bursting thalamic activity actually generates robust calcium entry in the dendrites of cortical cells (247). The entry of calcium might provide an ideal environment to prime synapses for plastic changes (248). Rosanova and Ulrich (190) showed that sleep spindles induce long-term synaptic changes and also induce Hebbian long-term potentiation in rat somatosensory layer V pyramidal cells.

Taken altogether, our model provides a platform to find the optimal topographical state point of the SO to apply stimulation cues in CLS which eventually improves spindle activity. Furthermore, in the experimental paradigm, the role of reticular network activity needs to be investigated in the occurrence of slow spindles during the SO Up to down-state transition. In future work, we will extend this study by including neuronal plasticity into the current model to make it learning based model.

Furthermore, we will study the role of CLS and increased spindle activity in synaptic plasticity.

**Summary**

In preceding chapters, three main EEG rhythms of NREM sleep were discussed. We presented a series of computational models for simulating SPW-Rs, SOs, and sleep spindles for exclusive investigations.

In first study we presented a theoretical model of hippocampal SPW-Rs. The hippocampus plays a key role in memory formation and learning. According to the concept of active systems memory consolidation, transiently stored memory traces are transferred from the hippocampus into the neocortex for permanent storage. This phenomenon relies on hippocampal network oscillations, particularly SPW-Rs. In this process prior saved data in the hippocampus may be reactivated. Recent investigations reveal that several neurotransmitters and neuromodulators including norepinephrine, acetylcholine, serotonin, etc., suppress SPW-Rs activity in rodents' hippocampal slices. This suppression of SPW-Rs may depend on various presynaptic and postsynaptic parameters including decrease in calcium influx, hyperpolarization / depolarization and alteration in gap junctions' function in pyramidal cells. In this study, we demonstrate the impact of calcium influx and gap junctions on pyramidal cells for the modulation of SPW-Rs in a computational model of CA1. We used SPW-Rs model with some modifications. SPW-Rs are simulated with gradual reduction of calcium and with decreasing conductance through gap junctions in PCs. Both, with calcium reduction as well as with conductance reduction through gap junctions, SPW-Rs are suppressed. Both effects add up synergistically in combination.

In second study, we presented a thalamocortical computational model for NREM sleep that exhibits both fast and slow spindles along with the SOs.Cortical SOs and thalamocortical sleep spindles are two prominent EEG rhythms of slow wave sleep. These EEG rhythms play an essential role in memory consolidation. In humans, sleep spindles are categorized into slow spindles (8–12 Hz) and fast spindles (12–16 Hz), with different properties. Slow spindles that couple with the up-to-down phase of the SO require more experimental and computational investigation to disclose their origin, functional relevance and most importantly their relation with SOs regarding

memory consolidation. To examine slow spindles, we propose a biophysical thalamocortical model with two independent thalamic networks (one for slow and the other for fast spindles). Our modeling results show that fast spindles lead to faster cortical cell firing, and subsequently increase the amplitude of the cortical local field potential (LFP) during the SO down-to-up phase. Slow spindles also facilitate cortical cell firing, but the response is slower, thereby increasing the cortical LFP amplitude later, at the SO up-to-down phase of the SO cycle. Neither the SO rhythm nor the duration of the SO down state is affected by slow spindle activity. Furthermore, at a more hyperpolarized membrane potential level of fast thalamic subnetwork cells, the activity of fast spindles decreases, while the slow spindles activity increases. Together, our model results suggest that slow spindles may facilitate the initiation of the following SO cycle, without however affecting expression of the SO Up and Down states.

In last study, we presented another thalamocortical model with closed loop stimulation (CLS) protocols to investigate the impact of CLS on spindle activity. Sleep spindles are one of the prominent EEG oscillatory rhythms of non-rapid eye movement sleep. In the memory consolidation, these have an important role in the processes of long-term potentiation and synaptic plasticity. Moreover, the activity (spindle density and/or sigma power) of spindles has a linear association with learning performance in different paradigms. According to the experimental observations, the sleep spindle activity can be improved by closed loop acoustic stimulations (CLAS) which eventually improve memory performance. To examine the effects of CLAS on spindles we propose a biophysical thalamocortical model for slow oscillations (SOs) and sleep spindles. In addition, closed loop stimulation (CLS) protocol is applied on a thalamic network. Our model results show that the power of spindles is significantly increased when stimulation cues are applied at the commencing of an SO Down to Up-state transition, but that activity gradually decreases when cues are applied with an increased time delay from this SO phase. Conversely, stimulation is not effective significantly when cues are applied during the transition of an SO Up to Down-state. Furthermore, our model suggests that a strong inhibitory input of reticular (RE) layer to a thalamocortical (TC) layer in the thalamic network shifts leads to an emergence of spindle activity at the SO Up to

Down-state transition (rather than at SO Down to Up-state transition), and the spindle frequency is also reduced (8-11 Hz) by thalamic inhibition.
In summary, our models revealed the following properties of SPW-Rs, SO and sleep spindles:

**First study:**

- Sharp-wave ripples occurred by summation of electrical coupling among CA1 cells and synaptic inputs of place cells.
- Sharp-wave ripples were suppressed by reduction in calcium influx.
- Weak electrical coupling between place cells weakened SPW-Rs activities.
- Combined reduction of calcium influx and electrical coupling had strong suppressive effect on SPW-Rs.

**Second study:**

- Fast spindles increased the SO amplitude.
- Slow spindles assisted in initiating the SO.
- Slow spindles regularized and stabilized the SO rhythm by preserving the SO down state.
- Hyperpolarization of the fast thalamic subnetwork reduced fast spindle density and increased the number of slow thalamic network events (slow spindles).

**Third study:**

- Spindles activity was increased when stimulation cues were applied at the commencement of the SO Down to Up-state transition.
- The effect of stimulation was decreased when cues were applied with increased delay from the commencement of the SO Down to Up-state transition.
- Spindle activity was not increased when cues were applied during the SO Up to Down-state transition.
- The sigma power of CLS2 was significantly stronger than DSt and CLS1 during D2U.

- A strong inhibitory input of the RE layer to the TC layer shifts the spindle activity to an SO Up to Down-state transition (from an SO Down to Up-state).

# Appendices

## Appendix A Equations

**Table A 3. 1 Rate functions for soma-dendrite compartments**

| Function | Forward (α) | Backward (β) |
|---|---|---|
| $g_{Na}$ activation (m) | $\frac{0.32(13.1-V)}{exp\left(\frac{13.1-V}{4}\right)-1}$ | $\frac{0.28(V-40.1)}{exp\left(\frac{V-40.1}{5}\right)-1}$ |
| $g_{Na}$ inactivation (h) | $.128exp\left(\frac{17-V}{18}\right)$ | $\frac{4}{1+exp\left(\frac{40-V}{5}\right)}$ |
| $g_{Ca}$(s) | $\frac{1.6}{1+\exp\left(-0.072(V-65)\right)}$ | $\frac{0.02(V-51.1)}{exp\left(\frac{V-51.1}{5}\right)-1}$ |
| $g_{K(DR)}$ (n) | $\frac{0.016(35.1-V)}{exp\left(\frac{35.1-V}{5}\right)-1}$ | $0.25exp\left(\frac{20-V}{40}\right)$ |
| $g_{K(AHP)}$ (q) | $\min\left(0.2\times10^{-4}\chi, 0.01\right)$ | 0.001 |
| $g_{K(A)}$ activation (a) | $\frac{0.02(13.1-V)}{exp\left(\frac{13.1-V}{10}\right)-1}$ | $\frac{0.0175(V-40.1)}{exp\left(\frac{V-40.1}{10}\right)-1}$ |
| $g_{K(A)}$ inactivation (b) | $0.0016\exp\left(\frac{-13-V}{18}\right)$ | $\frac{0.05}{1+exp\left(\frac{10.1-V}{5}\right)}$ |
| $g_{K(Ca)}$ (c) $[V \leq 50]$ | $\frac{exp\left[\left(\frac{V-10}{11}\right)-\left(\frac{V-6.5}{27}\right)\right]}{18.975}$ | $2\times exp\left(-\frac{V-6.5}{27}\right)-\propto_c$ |
| $g_{K(Ca)}$ (c) $[V \geq 50]$ | $2exp\left(-\frac{V-6.5}{27}\right)$ | 0 |

**Table A 3. 2 Rate functions for axon and (AIS) compartments**

| Function | Forward (α) | Backward (β) |
|---|---|---|
| $g_{Na}$ activation (m) | $\frac{0.8(17.2-V)}{exp\left(\frac{17.2-V}{4}\right)-1}$ | $\frac{0.7(V-42.2)}{exp\left(\frac{V-42.2}{5}\right)-1}$ |
| $g_{Na}$ inactivation (h) | $0.32exp\left(\frac{42-V}{18}\right)$ | $\frac{10}{1+exp\left(\frac{42-V}{5}\right)}$ |
| $g_{K(DR)}$ (n) | $\frac{0.03(17.2-V)}{exp\left(\frac{17.2-V}{5}\right)-1}$ | $0.45exp\left(\frac{12-V}{40}\right)$ |

**Table A 4. 1 Dynamical models of all intrinsic currents**

## For PY neurons

**(Axosomatic + dendritic) Fast sodium current $I_{Na}$**

$M$=3; $N$=1

$\alpha 1 = 0.182(V + 25)/(1 - \exp(-(V + 25)/9))$ *if* $|V - 10|/35 > 10^{-6} = 1.638$ *if* $|V - 10|/35 < 10^{-6}$

$\beta 1 = 0.124(-(V + 25))/(1 - \exp((V + 25)/9))$ *if* $|V - 10|/35 > 10^{-6} = 1.116$ *if* $|V - 10|/35 < 10^{-6}$

$\tau_m = 0.34/(\alpha 1 + \beta 1)$; $m_\infty = \alpha 1/(\alpha 1 + \beta 1)$;

$\alpha 2 = 0.024(V + 40)/(1 - \exp(-(V + 40)/5))$ *if* $|V - 10|/50 > 10^{-6} = 0.12$ *if* $|V - 10|/50 < 10^{-6}$

$\beta 2 = 0.0091(V - 85)/(1 - \exp(-(V - 85)/5))$ *if* $|V - 10|/50 > 10^{-6} = 0.0455$ *if* $|V - 10|/50 > 10^{-6}$

$\tau_h = (1/(\alpha 2 + \beta 2))/2.9529$; $h_\infty = 1/(1 + \exp((V + 55)/6.2))$;

**(Axosomatic & dendritic) Fast potassium current $I_K$**

$M$=1; $N$=0;

$\alpha = 0.02 * (V - 25)/(1 - \exp(-(V - 25)/9))$;

$\beta = -0.002 * (V - 25)/(1 - \exp((V - 25)/9))$;

$\tau_m = (1/(\alpha + \beta))/2.9529$; $m_\infty = \alpha/(\alpha + \beta)$;

**(Axosomatic + dendritic) Persistent sodium current $I_{Na(p)}$**

$M$=1; $N$=0;

$m_\infty = 0.02/(1 + exp(-(v + 42)/5))$;

**(Dendrite) Slow voltage-dependent non-inactivating potassium current $I_{Km}$**

$M = 1$; $N = 0$;

$\alpha = 0.001 \times (V + 30)/(1 - \exp(-(V + 30)/9))$;

$\beta = -0.001 \times (V + 30)/(1 - \exp((V + 30)/9))$;

$\tau_m = (1/(\alpha + \beta))/(-30)$; $m_\infty = \alpha/(\alpha + \beta)$;

**(Dendrite) Slow calcium-dependent potassium current $I_{KCa}$**

$M = 1$; $N = 0$;

$\alpha = 0.01 \times [Ca^{2+}]i$;

$\beta = 0.02$;

$\tau_m = (1/(\alpha + \beta))/2.9529$; $m_\infty = \alpha/(\alpha + \beta)$;

**(Dendrite) High-threshold calcium current $I_{HVA}$**

$M = 2$; $N = 1$;

$\alpha 1 = 0.055 \times (-27 - V)/(\exp((-27 - V)/3.8) - 1)$;

$\beta 1 = 0.94 \times \exp((-75 - V)/17)$;

$\tau_m = (1/(\alpha 1 + \beta 1))/2.9529$; $m_\infty = \alpha 1/(\alpha 1 + \beta 1)$;

$\alpha 2 = 0.000457 \times \exp((-13 - V)/50)$;

$\beta 2 = 0.0065/(\exp((-V - 15)/28) + 1)$;

$\tau_h = (1/(\alpha 2 + \beta 2))/2.9529$; $h_\infty = \alpha 2/(\alpha 2 + \beta 2)$;

**(Dendritic) Potassium leak current $I_{KL}$**

$M = 0$; $N = 0$;

$g_{KL} = 0.0025 mS/cm^2$;

## For IN neurons

IN cells have same current dynamics as PY cells except $I_{Na(p)}$. $I_{Na(p)}$ is not included in IN cells

## For TC neurons (TC neurons for both thalamic layers have same current dynamics)

**Fast sodium current $I_{Na}$**

$M = 3$; $N = 1$;

$\alpha 1 = 0.32 \times (-37 - v)/(\exp((13 - (V + 40))/4) - 1)$;

$\beta 1 = 0.28 \times (V - 90)/(\exp(((V + 40) - 40)/5) - 1)$;

$\tau_m = 1/(\alpha 1 + \beta 1)$; $m_\infty = \alpha 1/(\alpha 1 + \beta 1)$;

$\alpha 2 = 0.128 \times \exp((17 - (V + 40))/18)$;

$\beta 2 = 4/(\exp((40 - (V + 40))/5) + 1)$;

$\tau_h = 1/(\alpha 2 + \beta 2)$; $h_\infty = \alpha 2/(\alpha 2 + \beta 2)$;

**Fast potassium current $I_K$**

$M = 4$; $N = 0$;

$\alpha 1 = 0.032 \times (-35 - V)/(\exp((-35 - V)/5) - 1)$;

$\beta 1 = 0.5 \times \exp((-40 - V)/40)$;

$\tau_m = 1/(\alpha 1 + \beta 1)$; $m_\infty = \alpha 1/(\alpha 1 + \beta 1)$;

**Low-threshold calcium current $I_T$**

$M$=4;$N$=1;

*if* $V < -63$

$\tau_m = (1.0/(\exp((V + 35.82)/19.69) + \exp(-(V + 79.69)/12.7)) + 0.37)/3.9482$; $m_\infty = 1.0/(1 + \exp(-(V + 60)/8.5))$;

$\tau_h = 1.0/((\exp((V + 46.05)/5) + \exp(-(V + 238.4)/37.45)))/3.9482$;

*if* $V = -63$

$\tau_h = 19.0/3.9482$; $h_\infty = 1.0/(1 + \exp((V + 78)/6))$;

**hyperpolarization-activated cation current $I_h$**

*Voltage dependence*: $C \overset{\alpha}{\rightarrow} O,\ O \overset{\beta}{\rightarrow} C$

$h_\infty = 1/(1 + \exp((V + 75)/5.5))$;

$\tau_s = (20 + 1000/(\exp((V + 71.5)/14.2) + \exp(-(V + 89)/11.6)))$;

$\alpha = h_\infty/\tau_s$

$\beta = (1 - h_\infty)/\tau_s$

***Calcium dynamics*:**

$d[Ca]_i/dt = -AI_T + ([Ca]_\infty - [Ca]i)/\tau$,

$[Ca]_\infty = 2.4 * 10^{-4}$ mM, $A = 5.1819 * 10^{-5}$ mM cm$^2$/(ms μA) , $\tau$ = 5ms

**Potassium leak current $I_{KL}$**

$M = 0$; $N = 0$;

$g$KL = 0.03$mS/cm^2$;

## For RE neurons (RE neurons for both thalamic layers have same current dynamics)

**Fast sodium $I_{Na}$ and fast potassium current $I_K$** (RE cells have same $I_{Na}$ and $I_K$ current dynamics as TC cells)

**Low-threshold calcium current $I_{\underline{T}}$**

$M = 2$; $N = 1$;

$\tau_m = (3 + 1/(\exp((V + 27)/10) + \exp(-(V + 102)/15)))/6.8986$; $m_\infty = 1/(1 + \exp(-(V + 52)/7.4))$;

$\tau_h = (85 + 1/(\exp((V + 48)/4) + \exp(-(V + 407)/50)))/3.7372$; $h_\infty = 1/(1 + \exp((V + 80)/5))$;

**Potassium leak current $I_{KL}$**

$M = 0$; $N = 0$;

$g\mathrm{KL} = 0.005 mS/cm^2$;

## Appendix B Parameters

**Table B 3. 1 Maximum conductance densities**

| Level | $Na^+$ | $K_{(DR)}$ | $K_{(AHP)}$ | $K_{(A)}$ | $Ca^{2+}$ | $K_{(Ca)}$ |
|---|---|---|---|---|---|---|
| 1 | - | - | 0.0008 | - | 0.001 | 0.004 |
| 2 | - | - | 0.0008 | 0.0005 | 0.001 | 0.004 |
| 3 | 0.001 | 0.015 | 0.0008 | 0.0005 | 0.001 | 0.008 |
| 4 (Soma) | 0.070 | 0.170 | 0.0008 | 0.0005 | 0.001 | 0.02 |
| 5 (Shaft) | 0.003 | 0.020 | 0.0008 | 0.0005 | 0.001 | 0.008 |
| 6 | 0.003 | 0.020 | 0.0008 | 0.0005 | 0.001 | 0.008 |
| 7 | - | - | 0.0008 | - | 0.002 | 0.004 |
| 8 | - | - | 0.0008 | - | 0.003 | 0.012 |
| 9 | - | - | 0.0008 | - | 0.003 | 0.012 |
| 10 | - | - | 0.0008 | - | 0.001 | 0.004 |
| 11 | - | - | 0.0008 | - | 0.001 | 0.004 |
| AIS | 0.300 | 0.400 | - | - | - | - |
| Axon | 0.300 | 0.400 | - | - | - | - |

**Table B 4. 1 Model parameters and their values**

| Parameter name | Value | Description |
|---|---|---|
| **Cortical neurons, PY and IN (soma)** | | |
| $C_m$ | .75 µF/cm$^2$ | Membrane capacitance |
| $g_{Na}$ | 3000 mS/cm$^2$ (PY; IN) | Maximal sodium conductance |
| $g_K$ | 200 mS/cm$^2$ (PY; IN) | Maximal potassium conductance |
| $g_{Na(p)}$ | 15 mS/cm$^2$ (PY) | Maximal persistent sodium |
| **Cortical neurons, PY and IN (dendrite)** | | |
| $C_m$ | .75 µF/cm$^2$ | Membrane capacitance |
| $g_{Na}$ | 1.5 mS/cm$^2$ (PY; IN) | Maximal sodium conductance |
| $E_{Na}$ | 50 mV (PY; IN) | Sodium reversal potential |
| $g_{KL}$ | 0.003 mS/cm$^2$ (PY; IN) | Potassium leakage conductance |
| $E_{LK}$ | -95 mV (PY; IN) | Potassium leakage reversal |
| $g_L$ | 0.034 mS/cm$^2$ (PY; IN) | Leakage conductance |

| | | |
|---|---|---|
| $E_L$ | -68 mV (PY; IN) | Leakage reversal potential |
| $g_{Na(p)}$ | 2.5 mS/cm$^2$ (PY) | Maximal persistent sodium conductance |
| $g_{HVA}$ | 0.01 mS/cm$^2$ (PY; IN) | Maximal high-threshold $Ca^{2+}$ conductance |
| $g_{KCa}$ | 0.3 mS/cm$^2$ (PY; IN) | Slow $Ca^{2+}$ dependent $K^+$ conductance |
| $g_{Km}$ | 0.02 mS/cm$^2$ (PY); 0.03 mS/cm$^2$ (IN) | Slow voltage-dependent non-inactivating $K^+$ conductance |
| **Thalamic neurons, TC and RE (for fast spindles)** | | |
| $C_m$ | 1 μF/cm$^2$ | Membrane capacitance |
| $g_{Na}$ | 90 mS/cm$^2$ (TC); 100 mS/cm$^2$ (RE) | Maximal sodium conductance |
| $E_{Na}$ | 50 mV (TC; RE) | Sodium reversal potential |
| $g_K$ | 10 mS/cm$^2$ (RE); 10 mS/cm$^2$ (TC) | Maximal potassium conductance |
| $E_K$ | -95 mV (TC; RE) | Potassium reversal potential |
| $g_{KL}$ | 0.033 mS/cm$^2$ (TC); 0.005 mS/cm$^2$ (RE) | Potassium leakage conductance |
| $E_{KL}$ | -95 mV (TC; RE) | Potassium leakage reversal potential |
| $g_L$ | 0.01 mS/cm$^2$ (TC); 0.05 mS/cm$^2$ (RE) | Leakage conductance |
| $E_L$ | -70 mV (TC); -77 mV (RE) | Leakage reversal potential |
| $g_T$ | 1.8 mS/cm$^2$ (TC); 1.8 mS/cm$^2$ (RE) | Low-threshold $Ca^{2+}$ conductance |
| $g_h$ | 0.025 mS/cm$^2$ (TC) | Hyperpolarization-activated cation conductance |
| $E_h$ | -40 mV (TC) | Hyperpolarization-activated cation reversal potential |
| **Thalamic neurons, TC and RE (for slow spindles)** | | |
| $g_{Na}$ | 70 mS/cm$^2$ (TC); 100 mS/cm$^2$ (RE) | Maximal sodium conductance |
| $E_{Na}$ | 50 mV (TC; RE) | Sodium reversal potential |
| $g_K$ | 10 mS/cm$^2$ (RE); 12 mS/cm$^2$ (TC) | Maximal potassium conductance |
| $E_K$ | -95 mV (TC; RE) | Potassium reversal potential |
| $g_{KL}$ | 0.03 mS/cm$^2$ (TC); 0.015 mS/cm$^2$ (RE) | Potassium leakage conductance |
| $E_{KL}$ | -95 mV (TC; RE) | Potassium leakage reversal potential |
| $g_L$ | 0.01 mS/cm$^2$ (TC); 0.016mS/cm$^2$ (RE) | Leakage conductance |
| $E_L$ | -77mV (TC); -82 mV (RE) | Leakage reversal potential |
| $g_T$ | 1 mS/cm$^2$ (TC; RE) | Low-threshold $Ca^{2+}$ conductance |
| $g_h$ | 0.017 mS/cm$^2$ (TC) | Hyperpolarization-activated cation conductance |
| $E_h$ | -40 mV (TC) | Hyperpolarization-activated cation reversal potential |

**Table B 4. 2 Model Synaptic receptors and their conductance**

| Source to target neuron | Receptor | Synaptic conductance (μS) | Connecting radius |
|---|---|---|---|
| **Intracortical connections** | | | |
| PY→ PY | AMPARs | .026 | 11 |
| PY→PY | NMDARs | .0018 | 11 |
| PY→IN | AMPARs | .05 | 3 |
| PY→IN | NMDARs | .001 | 3 |
| IN→PY | $GABA_A$Rs | .16 | 11 |
| **Intrathalamic connections (Fast spindles)** | | | |
| $TC_{(f)}$→$RE_{(f)}$ | AMPARs | .025 | 17 |
| $RE_{(f)}$→$TC_{(f)}$ | $GABA_A$Rs | .05 | 17 |
| $RE_{(f)}$→$TC_{(f)}$ | $GABA_B$Rs | .01 | 17 |
| $RE_{(f)}$→$RE_{(f)}$ | $GABA_A$Rs | .075 | 11 |
| **Thalamocortical connections (Fast spindles)** | | | |
| $TC_{(f)}$→PY | AMPARs | .012 | 21 |
| $TC_{(f)}$→IN | AMPARs | .012 | 5 |
| **Cortico-thalamic connections (Fast spindles)** | | | |
| PY→$TC_{(f)}$ | AMPARs | .0013 | 21 |
| PY→$RE_{(f)}$ | AMPARs | .0032 | 17 |
| **Intrathalamic connections (Slow spindles)** | | | |
| $TC_{(S)}$→$RE_{(S)}$ | AMPARs | .022 | 17 |
| $RE_{(S)}$→$TC_{(S)}$ | $GABA_A$Rs | .22 | 17 |
| $RE_{(S)}$→$TC_{(S)}$ | $GABA_B$Rs | .025 | 17 |
| $RE_{(S)}$→$RE_{(S)}$ | $GABA_A$Rs | .05 | 11 |
| **Thalamocortical connections (Slow spindles)** | | | |
| $TC_{(S)}$→PY | AMPARs | .004 | 21 |
| $TC_{(S)}$→IN | AMPARs | .004 | 5 |
| **Cortico-thalamic connections (Slow spindles)** | | | |
| PY→$TC_{(S)}$ | AMPARs | .0009 | 21 |
| PY→$RE_{(S)}$ | AMPARs | .002 | 17 |

$RE_{(f)}$ and $TC_{(f)}$ thalamic neurons (Layer 3 and Layer 4 neurons) produce fast spindles and $RE_{(S)}$ and $TC_{(S)}$ thalamic neurons (Layer 5 and Layer 6 neurons) produce slow spindles.

**Table B 5. 1 Model parameters and their values**

**Table B 5.1: Model parameters, their values, and description.**

| Parameter name | Value | Description |
|---|---|---|
| **Cortical cells, PY and IN (soma)** | | |
| $g_{Na}$ | 2000 mS/cm$^2$ (PY; IN) | Maximal sodium conductance |
| $g_K$ | 200 mS/cm$^2$ (PY; IN) | Maximal potassium conductance |
| $g_{Na(p)}$ | 15 mS/cm$^2$ (PY) | Maximal persistent sodium |
| **Cortical cells, PY and IN (dendrite)** | | |
| $g_{Na}$ | 1.3 mS/cm$^2$ (PY; IN) | Maximal sodium conductance |
| $g_{KL}$ | 0.0033 mS/cm$^2$ (PY; IN) | Potassium leakage conductance |
| $E_{LK}$ | -95 mV (PY; IN) | Potassium leakage reversal |
| $g_L$ | 0.033 mS/cm$^2$ (PY; IN) | Leakage conductance |
| $E_L$ | -68 mV (PY; IN) | Leakage reversal potential |
| $g_{Na(p)}$ | 2.5 mS/cm$^2$ (PY) | Maximal persistent sodium conductance |
| $g_{HVA}$ | 0.01 mS/cm$^2$ (PY; IN) | Maximal high-threshold $Ca^{2+}$ conductance |
| $g_{KCa}$ | 0.4 mS/cm$^2$ (PY; IN) | Slow $Ca^{2+}$ dependent $K^+$ conductance |
| $g_{Km}$ | 0.014 mS/cm$^2$ (PY); 0.03 mS/cm$^2$ (IN) | Slow voltage-dependent noninactivating $K^+$ conductance |
| **Thalamic cells, TC and RE** | | |
| $C_m$ | 1 µF/cm$^2$ | Membrane capacitance |
| $g_{Na}$ | 90 mS/cm$^2$ (TC); 100 mS/cm$^2$ (RE) | Maximal sodium conductance |
| $g_K$ | 10 mS/cm$^2$ (RE); 10 mS/cm$^2$ (TC) | Maximal potassium conductance |
| $g_{KL}$ | 0.03 mS/cm$^2$ (TC); 0.03 mS/cm$^2$ (RE) | Potassium leakage conductance |
| $E_{KL}$ | -95 mV (TC; RE) | Potassium leakage reversal potential |
| $g_L$ | 0.028 mS/cm$^2$ (TC); 0.08 mS/cm$^2$ (RE) | Leakage conductance |
| $E_L$ | -70 mV (TC); -77 mV (RE) | Leakage reversal potential |
| $g_T$ | 1.1 mS/cm$^2$ (TC); 2 mS/cm$^2$ (RE) | Low-threshold $Ca^{2+}$ conductance |
| $g_h$ | 0.011 mS/cm$^2$ (TC) | Hyperpolarization-activated cation conductance |

**Table B 5. 2 Model Synaptic receptors and their conductance**

**Table B 5.2: Synaptic receptors, conductance, and their connecting radii**

| Source to target cell | Receptor | Synaptic conductance (μS) | Connecting radius |
|---|---|---|---|
| **Intracortical connections** | | | |
| PY→ PY | AMPA | .025 | 11 |
| PY→PY | NMDA | .0019 | 11 |
| PY→IN | AMPA | .055 | 3 |
| PY→IN | NMDA | .001 | 3 |
| IN→PY | $GABA_A$ | .055 | 11 |
| **Intra-thalamic connections** | | | |
| TC→RE | AMPA | .1 | 17 |
| RE→TC | $GABA_A$ | .05 | 17 |
| RE→TC | $GABA_B$ | .02 | 17 |
| RE→RE | $GABA_A$ | .05 | 11 |
| **Thalamocortical connections** | | | |
| TC→PY | AMPA | .01 | 21 |
| TC→IN | AMPA | .01 | 5 |
| **Cortico-thalamic connections** | | | |
| PY→TC | AMPA | .003 | 21 |
| PY→RE | AMPA | .0015 | 17 |

# Bibliography


1. Siegel. Sleep viewed as a state of adaptive inactivity. Nat Rev Neurosci. 2009 Oct; 10(10): p. 747-53.
2. Rasch B, Born J. About sleep's role in memory. Physiol Rev. 2013; 93(2): p. 681-766.
3. Diekelmann S, Born J. The memory function of sleep. Nat Rev Neurosci. 2010; 11(2): p. 114-26.
4. Maquet P. The role of sleep in learning and memory. Science. 2001; 294(5544): p. 1048-52.
5. Buzsáki G. Memory consolidation during sleep: a neurophysiological perspective. Sleep Res. 1998; 1: p. 17-23.
6. Staresina B, Bergmann T, Bonnefond M, van der Meij R, Jensen O, Deuker L, et al. Hierarchical nesting of slow oscillations, spindles and ripples in the human hippocampus during sleep. Nat Neurosci. 2015; 18(11): p. 1679-1686.
7. Brown J. Short-term memory. Br Med Bull. 1964; 20: p. 8-11.
8. Squire L, Zola S. Structure and function of declarative and nondeclarative memory systems. Proc Natl Acad Sci U S A. 1996; 93(24): p. 13515-22.
9. Eichenbaum H. Declarative memory: insights from cognitive neurobiology. Annu Rev Psychol. 1997; 48: p. 547-72.
10. Willingham. What differentiates declarative and procedural memories: reply to Cohen, Poldrack, and Eichenbaum (1997). Memory. 1998; 6(6): p. 689-99.
11. Smith C. Sleep states and memory processes in humans: procedural versus declarative memory systems. Sleep Medicine Reviews. 2001; 5(6): p. 491–506.
12. Walker M, Stickgold R. Sleep, memory, and plasticity. Annu Rev Psychol. 2006; 57: p. 139-66.
13. Nishida M, Pearsall J, Buckner R, Walker M. REM sleep, prefrontal theta, and the consolidation of human emotional memory. Cereb Cortex. 2009; 19(5): p. 1158-66.

14. Born J, Wilhelm I. System consolidation of memory during sleep. Psychological Research. 2012; 76: p. 192–203.
15. Steriade M, Amzica F. Slow sleep oscillation, rhythmic K-complexes, and their paroxysmal developments. J Sleep Res. 1998; 1: p. 30-5.
16. Massimini M, Huber R, Ferrarelli F, Hill S, Tononi G. The sleep slow oscillation as a traveling wave. J Neurosci. 2004; 31(24): p. 6862-70.
17. Adrian E. Afferent discharges to the cerebral cortex from peripheral sense organs. J Physiol. 1941; 100(2): p. 159-91.
18. Fernandez LMJ, Lüthi. Sleep Spindles: Mechanisms and Functions. Physiol Rev. 2020; 100(2): p. 805-868.
19. Buzsáki G. Hippocampal sharp wave-ripple: A cognitive biomarker for episodic memory and planning. Hippocampus. 2015; 25(10): p. 1073-188.
20. Boulder C. Embryonic vertebrate central nervous system: revised terminology. Anat Rec. 1970; 166(2): p. 257-61.
21. Callaway E. Local circuits in primary visual cortex of the macaque monkey. Annu Rev Neurosci. 1998; 21: p. 47-74.
22. DeFelipe J, Alonso-Nanclares L, Arellano J. Microstructure of the neocortex: comparative aspects. J Neurocytol. 2002; 31(3-5): p. 299-316.
23. Gilbert C, Kelly J. The projections of cells in different layers of the cat's visual cortex. J Comp Neurol. 1975; 163(1): p. 81-105.
24. Miller K, Pinto , DJ , Simons D. Processing in layer 4 of the neocortical circuit: new insights from visual and somatosensory cortex. Curr Opin Neurobiol. 2001; 11(4): p. 488-97.
25. Miller K. Understanding layer 4 of the cortical circuit: a model based on cat V1. Cereb Cortex. 2003; 13(1): p. 73-82.
26. Sherman S. Thalamocortical interactions. Curr Opin Neurobiol. 2012; 22(4): p. 575-9.
27. Sun W, Tan Z, Mensh B, Ji N. Thalamus provides layer 4 of primary visual cortex with orientation- and direction-tuned inputs. Nat Neurosci. 2016; 19(2): p. 308-15.

28. Rafati A, Safavimanesh F, Dorph-Petersen K, Rasmussen J, Møller J, Nyengaard J. Detection and spatial characterization of minicolumnarity in the human cerebral cortex. J Microsc. 2016; 261(1): p. 115-26.
29. Larkum M, Senn W, Lüscher H. Top-down dendritic input increases the gain of layer 5 pyramidal neurons. Cereb Cortex. 2004; 14(10): p. 1059-70.
30. Larkum M. A cellular mechanism for cortical associations: an organizing principle for the cerebral cortex. Trends Neurosci. 2013; 36(3): p. 141-51.
31. Steriade M, Nuñez A, Amzica F. A novel slow (>
32. Timofeev , Grenier F, Bazhenov , Sejnowski , Steriade. Origin of slow cortical oscillations in deafferented cortical slabs. Cereb Cortex. 2000; 10: p. 1185–1199.
33. Bazhenov M, Timofeev I, Steriade M, Sejnowski TJ. Model of thalamocortical slow-wave sleep oscillations and transitions to activated states. J Neurosci. 2002; 22: p. 8691– 8704.
34. Steriade M, Timofeev I, Grenier F. Natural waking and sleep states: a view from inside neocortical neurons. J Neurophysiol. 2001; 85: p. 1969–1985.
35. Nir , Staba RJ, Andrillon , Vyazovskiy VV, Cirelli , Fried , et al. Regional slow waves and spindles in human sleep. Neuron. 2011; 70: p. 153–169.
36. Todorova , Zugaro. Isolated cortical computations during delta waves support memory consolidation. Science. 2019 Oct; 366(6463): p. 377-381.
37. Galarreta , Hestrin. Frequency-dependent synaptic depression and the balance of excitation and inhibition in the neocortex. Nat Neurosci. 1998 Nov; 1(7): p. 587-94.
38. Sherman S, Guillery RW. Exploring the Thalamus and Its Role in Cortical Function. 2nd ed. London: The MIT Press; 2005.
39. Jones E. Thalamic circuitry and thalamocortical synchrony. Philos Trans R Soc Lond B Biol Sci.. 2002; 357(1428): p. 1659-73.
40. Jones E. Some aspects of the organization of the thalamic reticular complex. J Comp Neurol. 1975; 162(3): p. 285-308.

41. Steriade M. The thalamus as a neuronal oscillator. Brain Research Reviews. 1984; 8(1): p. 1–63.
42. Timofeev I, Steriade M. Low-frequency rhythms in the thalamus of intact-cortex and decorticated cats. Journal of Neurophysiology. 1996; 76(6): p. 4152–4168.
43. McCormick D, Pape H. Properties of a hyperpolarization-activated cation current and its role in rhythmic oscillation in thalamic relay neurones. The Journal of Physiology. 1990; 431: p. 291–318.
44. Bal T, McCormick D. What stops synchronized thalamocortical oscillations? Neuron. 1996; 17(2): p. 297-308.
45. Destexhe , Contreras , Steriade , Sejnowski TJ, Huguenard JR. In vivo, in vitro, and computational analysis of dendritic calcium currents in thalamic reticular neurons. J Neurosci. 1996b Jan; 16(1): p. 169-85.
46. Steriade M, Parent A, Paré D, Smith Y. Cholinergic and non-cholinergic neurons of cat basal forebrain project to reticular and mediodorsal thalamic nuclei. Brain Res. 1987; 408(1-2): p. 372-6.
47. Bazhenov M, Timofeev I, Steriade M, Sejnowski T. Self-sustained rhythmic activity in the thalamic reticular nucleus mediated by depolarizing GABAA receptor potentials. Nature Neuroscience. 1999; 2(2): p. 168–174.
48. Purcell , Manoach , Demanuele , Cade , Mariani , Cox , et al. Characterizing sleep spindles in 11,630 individuals from the National Sleep Research Resource. Nat Commun. 2017 Jun; 8: p. 15930.
49. McCormick D, Bal T. Sleep and arousal: thalamocortical mechanisms. Annu Rev Neurosci. 1997; 20: p. 185-215.
50. Lüthi A. Sleep spindles: where they come from, what they do. Neuroscientist. 2014; 20: p. 243–256.
51. Hagler DJ, Ulbert , Wittner , Ero˝ss , Madsen JR, Devinsky. Heterogeneous origins of human sleep spindles in different cortical layers. J Neurosci. 2018; 38: p. 3013–3025.

52. McDevitt E, Krishnan G, Bazhenov M, Mednick S. The Role of Sleep Spindles in Sleep-Dependent Memory Consolidation. In Axmacher N, Rasch B. Cognitive Neuroscience of Memory Consolidation.: Springer; 2017.
53. Amaral D, Witter M. The three-dimensional organization of the hippocampal formation: a review of anatomical data. Neuroscience. 1989; 31(3): p. 571-91.
54. Andersen P, Morris R, Amaral D, Bliss T, O'Keefe J. The Hippocampus Book New York: Oxford Univ. Press; 2007.
55. Bird C, Burgess N. The hippocampus and memory: insights from spatial processing. Nat Rev Neurosci. 2008; 9(3): p. 82-94.
56. Buzsáki G, Horváth Z, Urioste R, Hetke J, Wise K. High-frequency network oscillation in the hippocampus. Science. 1992; 256(5059): p. 1025-7.
57. Ylinen A, Bragin A, Nádasdy Z, Jandó G, Szabó I, Sik A, et al. Sharp wave-associated high-frequency oscillation (200 Hz) in the intact hippocampus: network and intracellular mechanisms. J Neurosci. 1995; 15(1 Pt 1): p. 30-46.
58. Chrobak J, Buzsáki G. High-frequency oscillations in the output networks of the hippocampal-entorhinal axis of the freely behaving rat. J Neurosci. 1996; 16(9): p. 3056-66.
59. Buzsáki G. Hippocampal sharp waves: their origin and significance. Brain Res. 1986; 398(2): p. 242-52.
60. Maier N, Nimmrich V, Draguhn A. Cellular and network mechanisms underlying spontaneous sharp wave-ripple complexes in mouse hippocampal slices. J Physiol. 2003; 550(Pt 3): p. 873-87.
61. Nimmrich V, Maier N, Schmitz D, Draguhn A. Induced sharp wave-ripple complexes in the absence of synaptic inhibition in mouse hippocampal slices. J Physiol. 2005; 563(Pt 3): p. 663-70.
62. Maier N, Tejero-Cantero A, Dorrn A, Winterer J, Beed P, Morris G, et al. Coherent phasic excitation during hippocampal ripples. Neuron. 2011; 72(1): p. 137-52.
63. Marr D. Simple memory: a theory for archicortex. Philos Trans R Soc Lond B Biol Sci. 1971; 262(841): p. 23-81.

64. McClelland J, McNaughton B, O'Reilly R. Why there are complementary learning systems in the hippocampus and neocortex: insights from the successes and failures of connectionist models of learning and memory. Psychol Rev. 1995; 02(3): p. 419-457.

65. Carr M, Jadhav S, Frank L. Hippocampal replay in the awake state: a potential substrate for memory consolidation and retrieval. Nat Neurosci. 2011; 14(2): p. 147-53.

66. Mölle M, Marshall L, Gais S, Born J. Learning increases human electroencephalographic coherence during subsequent slow sleep oscillations. Proc Natl Acad Sci U S A. 2004; 101(38): p. 13963-8.

67. Neske G. The Slow Oscillation in Cortical and Thalamic Networks: Mechanisms and Functions. Front Neural Circuits. 2016; 9: p. 88.

68. Gais S, Mölle M, Helms K, Born J. Learning-dependent increases in sleep spindle density. J Neurosci. 2002; 22(15): p. 6830-4.

69. Eschenko O, Ramadan W, Mölle M, Born J, Sara S. Sustained increase in hippocampal sharp-wave ripple activity during slow-wave sleep after learning. Learn Mem. 2008; 15(4): p. 222-8.

70. Huber R, Ghilardi M, Massimini M, Tononi G. Local sleep and learning. Nature. 2004; 430(6995): p. 78-81.

71. Clemens Z, Fabó D, Halász P. Overnight verbal memory retention correlates with the number of sleep spindles. Neuroscience. 2005; 132(2): p. 529-35.

72. Fogel S, Smith C. The function of the sleep spindle: a physiological index of intelligence and a mechanism for sleep-dependent memory consolidation. Neurosci Biobehav Rev. 2011; 35(5): p. 1154-65.

73. Siapas A, Wilson M. Coordinated interactions between hippocampal ripples and cortical spindles during slow-wave sleep. Neuron. 1998; 21(5): p. 1123-8.

74. Sirota A, Buzsáki G. Interaction between neocortical and hippocampal networks via slow oscillations. Thalamus Relat Syst. 2005; 3(4): p. 245-259.

75. Ulrich D. Sleep Spindles as Facilitators of Memory Formation and Learning. Neural Plast. 2016;: p. 1796715.

76. Seibt J, Richard C, Sigl-Glöckner J, Takahashi N, Kaplan D, Doron G, et al. Cortical dendritic activity correlates with spindle-rich oscillations during sleep in rodents. Nat Commun. 2017; 8(1): p. 684.

77. Purves D, Augustine G, Fitzpatrick D, Hall W, LaMantia AS, McNamara J, et al. Neuroscience 4th , editor. Massachusetts: Sinauer Associates; 2008.

78. Madden D. The structure and function of glutamate receptor ion channels. Nat Rev Neurosci. 2002; 3(2): p. 91-101.

79. Malinow R, Malenka R. AMPA receptor trafficking and synaptic plasticity. Annu Rev Neurosci. ; 26: p. 103-26.

80. Anggono V, Huganir R. Regulation of AMPA receptor trafficking and synaptic plasticity. Curr Opin Neurobiol. 2012; 22(3): p. 461-9.

81. Maren S, Baudry M. Properties and mechanisms of long-term synaptic plasticity in the mammalian brain: relationships to learning and memory. Neurobiol Learn Mem. 1995; 63(1): p. 1-18.

82. Hunt D, Castillo P. Synaptic plasticity of NMDA receptors: mechanisms and functional implications. Curr Opin Neurobiol. 2012; 22(3): p. 496-508.

83. Kaila K, Voipio J. Postsynaptic fall in intracellular pH induced by GABA-activated bicarbonate conductance. Nature. 1987; 330(6144): p. 163-5.

84. Rodríguez-Moreno A, Herreras O, Lerma J. Kainate receptors presynaptically downregulate GABAergic inhibition in the rat hippocampus. Neuron. 1997; 19(4): p. 893-901.

85. Kandel E, Schwartz J, Jessell T. Principles of Neural Science New York: McGraw-Hill; 2000.

86. Hormuzdi S, Filippov M, Mitropoulou G, Monyer H, Bruzzone R. Electrical synapses: a dynamic signaling system that shapes the activity of neuronal networks. Biochim Biophys Acta. 2004; 1662((1-2)): p. 113-37.

87. Bennett M, Zukin R. Electrical coupling and neuronal synchronization in the Mammalian brain. Neuron. 2004; 41(4): p. 495-511.

88. Draguhn A, Traub R, Schmitz D, Jefferys J. Electrical coupling underlies high-frequency oscillations in the hippocampus in vitro. Nature. 1998; 394(6689): p. 189-92.

89. Traub R, Schmitz D, Jefferys J, Draguhn A. High-frequency population oscillations are predicted to occur in hippocampal pyramidal neuronal networks interconnected by axoaxonal gap junctions. Neuroscience. 1999; 92(2): p. 407-26.

90. Schmitz D, Schuchmann S, Fisahn A, Draguhn A, Buhl E, Petrasch-Parwez E, et al. Axo-axonal coupling. a novel mechanism for ultrafast neuronal communication. Neuron. 2001; 31(5): p. 831-40.

91. Vladimirov N, Tu Y, Traub R. Synaptic gating at axonal branches, and sharp-wave ripples with replay: a simulation study. Eur J Neurosci. 2013; 38(10): p. 3435-47.

92. Hasselmo M, McGaughy J. High acetylcholine levels set circuit dynamics for attention and encoding and low acetylcholine levels set dynamics for consolidation. Prog Brain Res. 2004; 145: p. 207-31.

93. Norimoto H, Mizunuma M, Ishikawa D, Matsuki N, Ikegaya Y. Muscarinic receptor activation disrupts hippocampal sharp wave-ripples. Brain Res. 2012; 1461: p. 1-9.

94. Vandecasteele M, Varga V, Berényi A, Papp E, Barthó P, Venance L, et al. Optogenetic activation of septal cholinergic neurons suppresses sharp wave ripples and enhances theta oscillations in the hippocampus. Proc Natl Acad Sci U S A. 2014; 111(37): p. 13535-40.

95. Ul Haq R, Liotta A, Kovacs R, Rösler A, Jarosch M, Heinemann U, et al. Adrenergic modulation of sharp wave-ripple activity in rat hippocampal slices. Hippocampus. 2012; 22(3): p. 516-533.

96. Wang D, Yau H, Broker C, Tsou J, Bonci A, Ikemoto S. Mesopontine median raphe regulates hippocampal ripple oscillation and memory consolidation. Nat Neurosci. 2015; 18(5): p. 728-35.

97. Ul Haq R, Anderson M, Liotta A, Shafiq M, Sherkheli M, Heinemann U. Pretreatment with β-adrenergic receptor agonists facilitates induction of LTP and sharp wave ripple complexes in rodent hippocampus. Hippocampus. 2016; 26(12): p. 1486-1492.

98. Madison D, Nicoll R. Actions of noradrenaline recorded intracellularly in rat hippocampal CA1 pyramidal neurones, in vitro. J Physiol. 1986; 372: p. 221-44.
99. Schmitz D, Empson R, Heinemann U. Serotonin and 8-OH-DPAT reduce excitatory transmission in rat hippocampal area CA1 via reduction in presumed presynaptic Ca2+ entry. Brain Res. 1995; 701(1-2): p. 249-54.
100. Cobb S, Davies C. Cholinergic modulation of hippocampal cells and circuits. J Physiol. 2005; 562(Pt 1): p. 81-8.
101. Melonakos E, White J, Fernandez F. A model of cholinergic suppression of hippocampal ripples through disruption of balanced excitation/inhibition. Hippocampus. 2019; 29(9): p. 773-786.
102. Cairney S, Guttesen A, El Marj N, Staresina B. Memory Consolidation Is Linked to Spindle-Mediated Information Processing during Sleep. Curr Biol. 2018; 28(6): p. 948-954.e4.
103. Schönauer M. Sleep Spindles: Timed for Memory Consolidation. Curr Biol. 2018; 28(11): p. R656-R658.
104. Zhang Y, Gruber R. Can Slow-Wave Sleep Enhancement Improve Memory? A Review of Current Approaches and Cognitive Outcomes. Yale J Biol Med. 2019; 92(1): p. 63-80.
105. Rasch B, Büchel C, Gais S, Born J. Odor cues during slow-wave sleep prompt declarative memory consolidation. Science. 2007; 315(5817): p. 1426-9.
106. Antony J, Gobel E, O'Hare J, Reber P, Paller K. Cued memory reactivation during sleep influences skill learning. Nat Neurosci. 2012; 15(8): p. 1114-6.
107. Schönauer M, Geisler T, Gais S. Strengthening procedural memories by reactivation in sleep. J Cogn Neurosci. 2014; 26(1): p. 143-53.
108. Hu X, Cheng L, Chiu M, Paller K. Promoting memory consolidation during sleep: A meta-analysis of targeted memory reactivation. Psychol Bull. 2020; 146(3): p. 218-244.
109. Schouten D, Pereira S, Tops M, Louzada F. State of the art on targeted memory reactivation: Sleep your way to enhanced cognition. Sleep Med Rev. 2017; 32: p. 123-131.

110. Ngo H, Martinetz T, Born J, Mölle M. Auditory closed-loop stimulation of the sleep slow oscillation enhances memory. Neuron. 2013; 78(3): p. 545-53.

111. Ngo H, Miedema A, Faude I, Martinetz T, Mölle M, Born J. Driving sleep slow oscillations by auditory closed-loop stimulation-a self-limiting process. J Neurosci. 2015; 35(17): p. 6630-8.

112. Weigenand A, Mölle M, Werner F, Martinetz T, Marshall L. Timing matters: open-loop stimulation does not improve overnight consolidation of word pairs in humans. Eur J Neurosci. 2016; 44(6): p. 2357-68.

113. Marshall L, Helgadóttir H, Mölle M, Born J. Boosting slow oscillations during sleep potentiates memory. Nature. 2006; 444(7119): p. 610-3.

114. Marshall L, Mölle M, Hallschmid M, Born J. Transcranial direct current stimulation during sleep improves declarative memory. J Neurosci. 2004; 24(44): p. 9985-92.

115. Hodgkin A, Huxley A, Katz B. Measurement of current-voltage relations in the membrane of the giant axon of Loligo. J Physiol. 1952; 116(4): p. 424-48.

116. Hodgkin A, Huxley A. Currents carried by sodium and potassium ions through the membrane of the giant axon of Loligo. J Physiol. 1952a; 116(4): p. 449-72.

117. Hodgkin A, Huxley A. The components of membrane conductance in the giant axon of Loligo. J Physiol. 1952b; 116(4): p. 473-96.

118. Hodgkin A, Huxley A. The dual effect of membrane potential on sodium conductance in the giant axon of Loligo. J Physiol. 1952c; 116(4): p. 497-506.

119. Hodgkin AL HA. A quantitative description of membrane current and its application to conduction and excitation in nerve. J Physiol (Lond). 1952d; 117: p. 500–544.

120. David S, Bruce G, Andrew G, David W. Principles of Computational Modelling in Neuroscience Cambridge: Cambridge University Press; 2011.

121. Wang X. Calcium coding and adaptive temporal computation in cortical pyramidal neurons. J Neurophysiol. 1998; 79(3): p. 1549-66.

122. Destexhe A, Contreras D, Sejnowski T, Steriade M. A model of spindle rhythmicity in the isolated thalamic reticular nucleus. J Neurophysiol. 1994a; 72(2): p. 803-18.

123. Huguenard JR, Prince DA. A novel T-type current underlies prolonged Ca2+ □-dependent burst firing in GABAergic neurons of rat tha- lamic reticular nucleus. J Neurosci. 1992; 12: p. 3804 –3817.

124. Huguenard JR, McCormick DA. Simulation of the currents involved in rhythmic oscillations in thalamic relay neurons. J Neurophysiol. 1992; 68: p. 1373–1383.

125. Traub R, Wong RMR, Michelson H. A model of a CA3 hippocampal pyramidal neuron incorporating voltage-clamp data on intrinsic conductances. J Neurophysiol. 1991a; 66(2): p. 635-50.

126. Shouval H, Wang S, Wittenberg G. Spike timing dependent plasticity: a consequence of more fundamental learning rules. Front Comput Neurosci. 2010; 4: p. 19.

127. Tsodyks MV, Markram H. The neural code between neocortical pyramidal neurons depends on neurotransmitter release probability. Proc Natl Acad Sci USA. 1997; 94: p. 719–723.

128. Graupner M, Brunel N. Calcium-based plasticity model explains sensitivity of synaptic changes to spike pattern, rate, and dendritic location. Proc Natl Acad Sci U S A. 2012; 109(10): p. 3991-6.

129. Hindmarsh J, Rose R. A model of neuronal bursting using three coupled first order differential equations. Proc R Soc Lond B Biol Sci. 1984; 221(1222): p. 87-102.

130. Fitzhugh R. Impulses and Physiological States in Theoretical Models of Nerve Membrane. Biophys J. 1961; 1(6): p. 445-66.

131. Morris C, Lecar H. Voltage oscillations in the barnacle giant muscle fiber. Biophys J. 1981; 35(1): p. 193-213.

132. Lapicque L. Recherches quantitatives sur l'excitation electrique des nerfs traitée comme une polarization. J Physiol Pathol Gen (Paris). 1907; 9: p. 620–635.

133. Stein R. Some models of neuronal variability. Biophys J. 1967; 7(1): p. 37-68.

134. Tuckwell H. Introduction to Theoretical Neurobiology. In: linear cable theory and dendritic structure. 1st ed. Cambridge: Cambridge University Press; 1988.

135. Burkitt A. A review of the integrate-and-fire neuron model: I. Homogeneous synaptic input. Biol Cybern. 2006; 95(1): p. 1-19.

136. Izhikevich E, Gally J, Edelman G. Spike-timing dynamics of neuronal groups. Cereb Cortex. 2004; 14(8): p. 933-44.

137. Buzsáki G. Rhythms of the Brain: Oxford University Press; 2006.

138. Cowan J, Sharp D. Neural networks and artificial intelligence. Daedalus. 1988; 117: p. 85–121.

139. Wilson H, Cowan J. Excitatory and inhibitory interactions in localized populations of model neurons. Biophys J. 1972; 12(1): p. 1-24.

140. Wilson H, Cowan J. A mathematical theory of the functional dynamics of cortical and thalamic nervous tissue. Kybernetik. 1973; 13(2): p. 55-80.

141. Amari S. A method of statistical neurodynamics. Kybernetik. 1974; 14(4): p. 201-15.

142. Nunez P. The brain wave equation: A model for the EEG. Mathematical Biosciences. 1974; 21(3-4): p. 279–297.

143. Ledoux E, Brunel N. Dynamics of networks of excitatory and inhibitory neurons in response to time-dependent inputs. Front Comput Neurosci. 2011; 5: p. 25.

144. Lopes da Silva F, Hoeks A, Smits H, Zetterberg L. Model of brain rhythmic activity. The alpha-rhythm of the thalamus. Kybernetik. 1974; 15(1): p. 27-37.

145. Freeman W. Models of the dynamics of neural populations. Electroencephalogr Clin Neurophysiol Suppl. 1978; 34: p. 9-18.

146. Zetterberg L, Kristiansson L, Mossberg K. Performance of a model for a local neuron population. Biol Cybern. 1978; 31(1): p. 15-26.

147. Jansen B, Zouridakis G, Brandt M. A neurophysiologically-based mathematical model of flash visual evoked potentials. Biol Cybern. 1993; 68(3): p. 275-83.

148. Jansen B, Rit V. Electroencephalogram and visual evoked potential generation in a mathematical model of coupled cortical columns. Biol Cybern. 1995; 73(4): p. 357-66.

149. Liley D, Cadusch P, Wright J. A continuum theory of electro-cortical activity. Neurocomputing. 1999; 26-27: p. 795–800.

150. Wendling F, Bellanger J, Bartolomei F, Chauvel P. Relevance of nonlinear lumped-parameter models in the analysis of depth-EEG epileptic signals. Biol Cybern. 2000; 83(4): p. 367-78.

151. Sotero R, Trujillo-Barreto N, Iturria-Medina Y, Carbonell F, Jimenez J. Realistically coupled neural mass models can generate EEG rhythms. Neural Comput. 2007; 19(2): p. 478-512.

152. Kiebel S, Garrido M, Moran R, Chen C, Friston K. Dynamic causal modeling for EEG and MEG. Hum Brain Mapp. 2009; 30(6): p. 1866-76.

153. Hines M. NEURON-a program for simulation of nerve equations. In F E, Norwell M. Neural Systems: Analysis and Modeling.: Kluwer Academic Publishers; 1993. p. 127-136.

154. Hines ML, Carnevale NT. The NEURON simulation environment. Neural Comput. 1997; 9: p. 1179–1209.

155. Bower J, Beeman D. The book of GENESIS: Exploring realistic neural models with the GEneral NEural SImulation System. 2nd ed. New York: Springer-Verlag; 1998.

156. R B, M R, T C, M H, Beeman D, Bower J, et al. Simulation of networks of spiking neurons: a review of tools and strategies. J Comput Neurosci. 2007; 23(3): p. 349-98.

157. Bard E. Simulating, Analyzing, and Animating Dynamical Systems: A Guide to XPPAUT for Researchers and Students Philadelphia: PA: Society for Industrial Mathematics; 2002.

158. Ziv I, Baxter D, Byrne J. Simulator for neural networks and action potentials: description and application. J Neurophysiol. 1994; 71(1): p. 294-308.

159. Baxter D, Byrne J. Simulator for neural networks and action potentials. Methods Mol Biol. 2007; 401: p. 127–154.

160. Carnevale N, Hines M. The NEURON Book Cambridge: Cambridge University Press; 2006.

161. Crank J. The Mathematics of Diffusion. 2nd ed. London: Oxford University Press; 1979.

162. Jack J, Noble D, Tsien R. Electric Current Flow in Excitable Cells London: Oxford University Press; 1983.

163. Johnston D, Wu S. Foundations of Cellular Neurophysiology Cambridge: MIT Press; 1995.

164. Kootsey J, Kohn M, Feezor M, Mitchell G, Fletcher P. SCoP: an interactive simulation control program for micro- and minicomputers. Bulletin of Mathematical Biology. Bulletin of Mathematical Biology. 1986; 48: p. 427-441.

165. Mushtaq M, Haq R, Anwar W, Marshall L, Bazhenov M, Zia K, et al. A computational study of suppression of sharp wave ripple complexes by controlling calcium and gap junctions in pyramidal cells. Bioengineered. 2021; 12(1): p. 2603-2615.

166. O'Keefe J, Nadel L. The Hippocampus as a Cognitive Map Oxford: Oxford University Press; 1978.

167. Wilson M, McNaughton B. Reactivation of hippocampal ensemble memories during sleep. Science. 1994; 265(5172): p. 676-9.

168. Skaggs W, McNaughton B, Wilson M, Barnes C. Theta phase precession in hippocampal neuronal populations and the compression of temporal sequences. Hippocampus. 1996; 6(2): p. 149-72.

169. Lee A, Wilson M. Memory of sequential experience in the hippocampus during slow wave sleep. Neuron. 2002; 36(6): p. 1183-94.

170. Kudrimoti H, Barnes C, McNaughton B. Reactivation of hippocampal cell assemblies: effects of behavioral state, experience, and EEG dynamics. J Neurosci. 1999; 19(10): p. 4090-101.

171. Nádasdy Z, Hirase H, Czurkó A, Csicsvari J, Buzsáki G. Replay and time compression of recurring spike sequences in the hippocampus. J Neurosci. 1999; 19(21): p. 9497-507.

172. O'Neill J, Senior T, Csicsvari J. Place-selective firing of CA1 pyramidal cells during sharp wave/ripple network patterns in exploratory behavior. Neuron. 2006; 49(1): p. 143-55.

173. Davidson T, Kloosterman F, Wilson M. Hippocampal replay of extended experience. Neuron. 2009; 63(4): p. 497-507.

174. Koene R, Hasselmo M. Reversed and forward buffering of behavioral spike sequences enables retrospective and prospective retrieval in hippocampal regions CA3 and CA1. Neural Netw. 2008; 21(2-3): p. 276-88.

175. Memmesheimer R. Quantitative prediction of intermittent high-frequency oscillations in neural networks with supralinear dendritic interactions. Proc Natl Acad Sci U S A. 2010; 107(24): p. 11092-7.

176. Taxidis J, Coombes S, Mason R, Owen M. Modeling sharp wave-ripple complexes through a CA3-CA1 network model with chemical synapses. Hippocampus. 2012; 22(5): p. 995-1017.

177. Traub R, Bibbig A. A model of high-frequency ripples in the hippocampus based on synaptic coupling plus axon-axon gap junctions between pyramidal neurons. J Neurosci. 2000; 20(6): p. 2086-93.

178. Traub R, Schmitz D, Maier N, Whittington M, Draguhn A. Axonal properties determine somatic firing in a model of in vitro CA1 hippocampal sharp wave/ripples and persistent gamma oscillations. Eur J Neurosci. 2012; 36(5): p. 2650-60.

179. Donoso J, Schmitz D, Maier N, Kempter R. Hippocampal Ripple Oscillations and Inhibition-First Network Models: Frequency Dynamics and Response to GABA Modulators. J Neurosci. 2018; 38(12): p. 3124-3146.

180. Traub RD JJMRWMTK. A branching dendritic model of a rodent CA3 pyramidal neurone. J. Physiol. 1994; 481: p. 79–95.

181. Epsztein J, Lee A, Chorev E, Brecht M. Impact of spikelets on hippocampal CA1 pyramidal cell activity during spatial exploration. Science. 2010; 327(5964): p. 474-7.

182. Lee D, Lin B, Lee A. Hippocampal place fields emerge upon single-cell manipulation of excitability during behavior. Science. 2012; 337(6096): p. 849-53.

183. Wang X, Buzsáki G. Gamma oscillation by synaptic inhibition in a hippocampal interneuronal network model. J Neurosci. 1996; 16(20): p. 6402-13.

184. Mushtaq M, Marshall L, Bazhenov M, Mölle M, Martinetz T. Differential thalamocortical interactions in slow and fast spindle generation: A computational model. PLoS One. 2022; 17(12): p. e0277772.

185. Born , Rasch , Gais. Sleep to remember. Neuroscientist. 2006; 12(5): p. 410–424.

186. Marshall , Born. The contribution of sleep to hippocampus-dependent memory consolidation. Trends Cogn Sci. 2007; 11: p. 442–450.

187. Chauvette , Seigneur , Timofeev. Sleep oscillations in the thalamocortical system induce long-term neuronal plasticity. Neuron. 2012; 75: p. 1105–1113.

188. Todorova , Zugaro. Hippocampal ripples as a mode of communication with cortical and subcortical areas. Hippocampus. 2020 Jan; 30(1): p. 39-49.

189. Antony JW, Piloto , Wang , Pacheco , Norman KA, Paller KA. Sleep spindle refractoriness segregates periods of memory reactivation. Current Biology. 2018; 28: p. 1736–1743.

190. Rosanova , Ulrich. Pattern-Specific Associative Long-Term Potentiation Induced by a Sleep Spindle-Related Spike Train. J Neurosci. 2005 October; 25(41): p. 9398 –9405.

191. Ayoub , Aumann , Hörschelmann , Kouchekmanesch , Paul , Born , et al. Differential effects on fast and slow spindle activity, and the sleep slow oscillation in humans with carbamazepine and flunarizine to antagonize voltage-dependent Na□ and Ca2□ channel activity. Sleep. 2013; 36: p. 905–911.

192. Dehnavi , Moghimi , Ghorbani , Hashemi NS. Slow spindles are associated with cortical high frequency activity. Neuroimage. 2019; 89: p. 71–84.

193. Andrillon T, Nir Y, Staba RJ, Ferrarelli , Cirelli , Tononi , et al. Sleep spindles in humans: insights from intracranial EEG and unit recordings. J Neurosci. 2011; 31(49): p. 17821-34.

194. Bastuji , Lamouroux , Villalba , Magnin , Garcia-Larrea. Local sleep spindles in the human thalamus. J Physiol. 2020; 598(11): p. 2109-2124.

195. Halassa MM, Chen , Wimmer RD, Brunetti PM, Zhao , Zikopoulos , et al. State-dependent architecture of thalamic reticular subnetworks. Cell. 2014; 158: p. 808–821.

196. Mainen ZF, Sejnowski TJ. Influence of dendritic structure on firing pattern in model neocortical neurons. Nature. 1996; 382: p. 363–366.

197. Traub RD, Miles R. Neuronal networks of the hippocampus. Cambridge, UK: Cambridge; 1991.

198. Destexhe , Bal, T, McCormick DA, Sejnowski TJ. Ionic mechanisms underlying synchronized oscillations and propagating waves in a model of ferret thalamic slices. J Neurophysiol. 1996a; 76: p. 2049–2070.

199. Destexhe , Mainen ZF. Synthesis of models for excitable membrane, synaptic transmission and neuromodulation using a common kinetic formalism. J Comp Neurosci. 1994; 1: p. 195–230.

200. Wei , Krishnan GP, Bazhenov. Synaptic mechanisms of memory consolidation during sleep slow oscillations. J Neurosci. 2016; 36: p. 4231– 4247.

201. Abbott LF, Varela JA, Sen K, Nelson SB. Synaptic depression and cortical gain control. Science. 1997; 275: p. 220–224.

202. Dutar P NR. A physiological role for GABAB receptors in the central nervous system. Nature. 1988;: p. 332: 156–158.

203. Krishnan GP, Chauvette , Shamie , Soltani , Timofeev , Cash SS, et al. Cellular and neurochemical basis of sleep stages in the thalamocortical network. eLife. 2016; 5: p. e18607.

204. Wei , Krishnan GP, Marshall , Martinetz T, Bazhenov M. Stimulation Augments Spike Sequence Replay and Memory Consolidation during Slow-Wave Sleep. J Neuroscience. 2020 January; 40(4): p. 811– 824.

205. Hirsch J, Fourment A, Marc M. Sleep-related variations of membrane potential in the lateral geniculate body relay neurons of the cat. Brain Res. 1983; 259(2): p. 308-12.

206. Steriade M. Cellular Substrates of Brain Rhythms; 1993b.

207. Cowan E, Liu A, Henin S, Kothare S, Devinsky O, Davachi L. Sleep Spindles Promote the Restructuring of Memory Representations in Ventromedial Prefrontal Cortex through Enhanced Hippocampal-Cortical Functional Connectivity. J Neurosci. 2020; 40(9): p. 1909-1919.

208. Bastian L, Samanta A, Ribeiro de Paula D, Weber F, Schoenfeld R, Dresler M, et al. Spindle-slow oscillation coupling correlates with memory performance and connectivity changes in a hippocampal network after sleep. Hum Brain Mapp. 2022; 43(13): p. 3923-3943.

209. Loomis A, Harvey E, Hobart G. POTENTIAL RHYTHMS OF THE CEREBRAL CORTEX DURING SLEEP. Science. 1935; 81(2111): p. 597-8.

210. Marshall L, Cross N, Binder S, Dang-Vu T. Brain Rhythms During Sleep and Memory Consolidation: Neurobiological Insights. Physiology (Bethesda). 2020; 35(1): p. 4-15.

211. Niknazar M, Krishnan G, Bazhenov M, Mednick S. Coupling of Thalamocortical Sleep Oscillations Are Important for Memory Consolidation in Humans. PLoS One. 2015; 10(12): p. e0144720.

212. Niethard N, Ngo H, Ehrlich I, Born J. Cortical circuit activity underlying sleep slow oscillations and spindles. Proc Natl Acad Sci U S A. 2018; 115(39): p. E9220-E9229.

213. Schabus M, Gruber G, Parapatics S, Sauter C, Klösch G, Anderer P, et al. Sleep spindles and their significance for declarative memory consolidation. Sleep. 2004; 27(8): p. 1479-85.

214. Tamminen J, Payne J, Stickgold R, Wamsley E, Gaskell M. Sleep spindle activity is associated with the integration of new memories and existing knowledge. J Neurosci. 2010; 30(43): p. 14356-60.

215. Campos-Beltrán D, Marshall L. Changes in sleep EEG with aging in humans and rodents. Pflugers Arch. 2021; 473(5).

216. Vyazovskiy V, Faraguna U, Cirelli C, Tononi G. Triggering slow waves during NREM sleep in the rat by intracortical electrical stimulation: effects of sleep/wake history and background activity. J Neurophysiol. 2009; 101(4): p. 1921-31.

217. Henin S, Borges H, Shankar A, Sarac C, Melloni L, Friedman D, et al. Closed-Loop Acoustic Stimulation Enhances Sleep Oscillations But Not Memory Performance. eNeuro. 2019; 6(6): p. ENEURO.0306-19.2019.

218. Aksamaz S, Mölle M, Akinola E, Gromodka E, Bazhenov M, Marshall L. Single closed-loop acoustic stimulation targeting memory consolidation suppressed hippocampal ripple and thalamo-cortical spindle activity in mice. Eur J Neurosci. 2023.

219. Henao D, Navarrete M, Juez J, Dinh H, Gómez R, Valderrama M, et al. Auditory closed-loop stimulation on sleep slow oscillations using in-ear EEG sensors. J Sleep Res. 2022; 31(6): p. e13555.

220. Koo-Poeggel P, Neuwerk S, Petersen E, Grasshoff J, Mölle M, Martinetz T, et al. Closed-loop acoustic stimulation during an afternoon nap to modulate subsequent encoding. J Sleep Res. 2022; 31(6): p. e13734.

221. Rörig B, Sutor B. Regulation of gap junction coupling in the developing neocortex. Mol Neurobiol. 1996; 12(3): p. 225-49.

222. Blomstrand F, Khatibi S, Muyderman H, Hansson E, Olsson T, Rönnbäck L. 5-Hydroxytryptamine and glutamate modulate velocity and extent of intercellular calcium signalling in hippocampal astroglial cells in primary cultures. Neuroscience. 1999; 88(4): p. 1241-53.

223. Zsiros V, Maccaferri G. Noradrenergic modulation of electrical coupling in GABAergic networks of the hippocampus. J Neurosci. 2008; 28(8): p. 1804-15.

224. Velazquez J, Han D, Carlen P. Neurotransmitter modulation of gap junctional communication in the rat hippocampus. Eur J Neurosci. 1997; 9(12): p. 2522-31.

225. Fernández-Ruiz A, Oliva A, Fermino de Oliveira E, Rocha-Almeida F, Tingley D, Buzsáki G. Long-duration hippocampal sharp wave ripples improve memory. Science. 2019; 364(6445): p. 1082-1086.

226. Sanchez-Vives MV, McCormick DA. Cellular and network mechanisms of rhythmic recurrent activity in neocortex. Nat Neurosci. 2000 Oct; 3(10): p. 1027-1034.

227. MacLean JN, Watson BO, Aaron GB, Yuste. Internal Dynamics Determine the Cortical Response to Thalamic Stimulation. Neuron. 2005; 48: p. 811–823.

228. Rigas , Castro-Alamancos MA. Thalamocortical Up States: Differential Effects of Intrinsic and Extrinsic Cortical Inputs on Persistent Activity. J Neurosci. 2007 April; 27(16): p. 4261– 4272.

229. David , Schmiedt JT. Thalamus and Cortex: Inseparable Partners in Shaping Sleep Slow Waves? J Neurosci. 2014; 27(34(35)): p. 11517-8.

230. Lemieux , Chen JY, Lonjers , Bazhenov , Timofeev. The Impact of Cortical Deafferentation on the Neocortical Slow Oscillation. J Neurosci. 2014 April; 34(16): p. 5689 –5703.

231. Jones EG. The thalamic matrix and thalamocortical synchrony. Trends Neurosci. 2001 Oct; 24(10): p. 595-601.

232. Shepherd GMG, Yamawaki. Untangling the cortico-thalamo-cortical loop: cellular pieces of a knotty circuit puzzle. Nat Rev Neurosci. 2021 Jul; 22(7): p. 389-406.

233. Rah JC, Bas , Colonell , Mishchenko , Karsh , Fetter RD, et al. Thalamocortical input onto layer 5 pyramidal neurons measured using quantitative large-scale array tomography. Front Neural Circuits. 2013 Nov; 7: p. 177.

234. Mak-McCully RA, Rolland , Sargsyan , Gonzalez , Magnin , Chauvel , et al. Coordination of cortical and thalamic activity during non-REM sleep in humans. Nat Commun. 2017 May; 25(8): p. 15499.

235. Urbain , Fourcaud-Trocme´ , Laheux , Salin PA, Gentet LJ. Brain-State-Dependent Modulation of Neuronal Firing and Membrane Potential Dynamics in the Somatosensory Thalamus during Natural Sleep. Cell Rep. 2019 Feb; 26(6): p. 1443-1457.

236. Klinzing JG, Mölle , Weber , Supp , Hipp JF, Engel AK, et al. Spindle activity phase-locked to sleep slow oscillations. NeuroImage. 2016; 134 : p. 607–616.

237. Gonzalez CE, Mak-McCully RA, Rosen BQ, Cash SS, Chauvel PY. Theta Bursts Precede, and Spindles Follow, Cortical and Thalamic Downstates in Human NREM Sleep. J Neurosci. 2018 Nov; 38(46): p. 9989-10001.

238. Mölle , Bergmann TO, Marshall , Born. Fast and Slow Spindles during the Sleep Slow Oscillation: disparate Coalescence and engagement in Memory processing. Sleep. 2011 Oct; 34(10): p. 1411-21.

239. Steriade M. Grouping of brain rhythms in corticothalamic systems. Neuroscience. 2006; 137(4): p. 1087-106.

240. Contreras D, Steriade M. Cellular basis of EEG slow rhythms: a study of dynamic corticothalamic relationships. J Neurosci. 1995; 15(1 Pt 2): p. 604-22.

241. González-Rueda A, Pedrosa V, Feord R, Clopath C, Paulsen O. Activity-Dependent Downscaling of Subthreshold Synaptic Inputs during Slow-Wave-Sleep-like Activity In Vivo. Neuron. 2018; 97(6): p. 1244-1252.

242. Dang-Vu T, McKinney S, Buxton O, Solet J, Ellenbogen J. Spontaneous brain rhythms predict sleep stability in the face of noise. Curr Biol. 2010; 20(15): p. R626-7.

243. Dang-Vu T. Neuronal oscillations in sleep: insights from functional neuroimaging. Neuromolecular Med. 2012; 14(3): p. 154-67.

244. Hanganu-Opatz I. Between molecules and experience: role of early patterns of coordinated activity for the development of cortical maps and sensory abilities. Brain Res Rev. 2010; 64(1): p. 160-76.

245. Khazipov , Sirota A, Leinekugel X, Holmes G, Ben-Ari Y, Buzsáki G. Early motor activity drives spindle bursts in the developing somatosensory cortex. Nature. 2004; 432(7018): p. 758-61.

246. Dan Y, Poo M. Spike timing-dependent plasticity of neural circuits. Neuron. 2004; 44(1): p. 23-30.

247. Contreras D, Destexhe A, Steriade M. Intracellular and computational characterization of the intracortical inhibitory control of synchronized thalamic inputs in vivo. J Neurophysiol. 1997; 78(1): p. J Neurophysiol.

248. Sejnowski T, Destexhe A. Why do we sleep? Brain Res. 2000; 886(1-2): p. 208-223.

# List of Publications

- **Mushtaq M**, Marshall L, Haq RU, Martinetz T (under review). Possible mechanisms to improve sleep spindles via closed loop stimulation during slow wave sleep. A computational study

- **Mushtaq M**, Marshall L, Bazhenov M, Mölle M, Martinetz T. Differential thalamocortical interactions in slow and fast spindle generation: A computational model. PLoS One. 2022; 17(12): e0277772

- **Mushtaq M**, Haq RU, Anwar W, Marshall L, Bazhenov M, Zia K, Alam H, Hertel L, Awan AA, Martinetz T. A computational study of suppression of sharp wave ripple complexes by controlling calcium and gap junctions in pyramidal cells. Bioengineered. 2021; 12(1): 2603-2615

- Khan HA, Jue W, **Mushtaq M**, Mushtaq MU. Brain tumor classification in MRI image using convolutional neural network. Math Biosci Eng. 2020; 17(5): 6203-6216

- Rehman MU, **Mushtaq M**, Sherkheli MA. Glutamine augments neuronal network activity in Rat hippocampal slices. J Ayub Med Coll Abbottabad. 2017; 29(3): 388-392